

Washington University in St. Louis

Washington University Open Scholarship

All Theses and Dissertations (ETDs)

January 2009

Metal Oxide Semiconductors for Solar Energy Harvesting

Elijah Thimsen

Washington University in St. Louis

Follow this and additional works at: <https://openscholarship.wustl.edu/etd>

Recommended Citation

Thimsen, Elijah, "Metal Oxide Semiconductors for Solar Energy Harvesting" (2009). *All Theses and Dissertations (ETDs)*. 347.

<https://openscholarship.wustl.edu/etd/347>

This Dissertation is brought to you for free and open access by Washington University Open Scholarship. It has been accepted for inclusion in All Theses and Dissertations (ETDs) by an authorized administrator of Washington University Open Scholarship. For more information, please contact digital@wumail.wustl.edu.

WASHINGTON UNIVERSITY IN SAINT LOUIS

School of Engineering and Applied Science

Department of Energy, Environmental and Chemical Engineering

Dissertation Examination Committee

Pratim Biswas, Chair
Richard Axelbaum
Robert Blankenship
Daniel Giammar
Dewey Holten
Cynthia Lo

METAL OXIDE SEMICONDUCTORS FOR SOLAR ENERGY HARVESTING

by

Elijah James Thimsen

A dissertation presented to the Graduate School of Arts and Sciences of Washington
University in partial fulfillment for the degree of Doctor of Philosophy

August 2009

Saint Louis, Missouri, United States of America

Acknowledgements

I am very thankful to Professor Pratim Biswas for many things, including the numerous opportunities he has provided me and for his continuing support during my tenure at Washington University. He provided me with a seed that grew into a very enjoyable and interesting dissertation. But I am particularly grateful to him for teaching me something that I will use for the rest of my life, no matter where my career takes me. Professor Biswas has taught me to stand on my own two feet as a researcher, always providing enough help to keep me standing, but never too much so I would risk falling when the support was gone. Thanks to him, I wrap up my work at Washington University bolstered by the confidence that I have what it takes to be independent and take the lead.

I am very thankful to Professor Dewey Holten and his group in the chemistry department for teaching me the fundamentals of physical chemistry, which have been, and continue to be indispensable in my research. Professor Cynthia Lo took the time to teach the principles and computational applications of quantum chemistry, which can be abstract and difficult to grasp at times. I am sincerely thankful for that. I am also thankful for discussions with Professor Bob Blankenship, through which the inner workings of photosynthesis have started to become clear, a knowledge base that will be valuable as I continue my work on artificial systems. Professors Axelbaum and Giammar were instrumental to the planning of this work, and have provided great advice on planning my career.

I had the opportunity to work with two outstanding undergraduate students during my time at Washington University: Sam Crawford and Neema Rastgar. They have

helped me tremendously, and both are among the coauthors of the work presented in this thesis.

I would like to also acknowledge my colleagues in the AAQRL for constantly proving an intellectually challenging and fruitful environment. I would particularly like to thank Jingkun Jiang and Chris Hogan for countless discussions and providing examples to follow. I would also like to thank Hee-eun Song and Anne Kee in Professor Holten's group for numerous discussions about physical chemistry and for helping to conduct collaborative experiments.

I would also like to thank the administrative assistants in the EECE department, Beth Mehringer for helping to smooth the reimbursement procedure, Mindy Price and Trisha Sutton for aiding with purchasing, and Rose Baxter for helping with many things, from required paperwork to helping find rooms for meetings.

Without funding, this work would not have been possible. I would like to thank the Center for Materials Innovation for awarding me the Graduate Fellowship, the Center for Environmentally Beneficial Catalysis at Kansas University (NSF ERC-0310689), Corning Incorporated, DOD-MURI grant UR523873, the NSF- NIRT 0304649 Grant and the McDonnell Academy Global Energy and Environmental Partnership (MAGEEP) at Washington University in St. Louis.

Finally, I would like to thank my family and friends for constant encouragement. A few friends in particular that have helped me stay on the path: Subramanya Nayak, Heather Kay, Kenneth Anders Fischl and Jessica Deem.

Table of Contents

Acknowledgements	i
List of Figures	vi
List of Tables	x
Abstract	xi
Chapter 1: Introduction	1
1.1 Overview	2
1.2 Problem Statement.....	2
1.3 Approach	4
1.4 Conclusion.....	8
1.5 References	8
Chapter 2: Human Development and the Energy-Environment Nexus	10
2.1 Abstract.....	11
2.2 Introduction	12
2.3 Methods	15
2.4 G20 Nations.....	16
2.5 Global Perspective.....	20
2.6 Carbon Dioxide Emissions	24
2.7 Efficiency in the United States	28
2.8 Conclusions	30
2.9 Acknowledgements	31
2.10 References	31
Chapter 3: Synthesis of Nanostructured Photoactive Films with Controlled Morphology by a Flame Aerosol Reactor	34
3.1 Abstract.....	35
3.2 Introduction	36
3.3 Experimental Methods.....	39
3.3.1 System.....	39
3.3.2 Characterization	41

3.3.3 Test Plan.....	42
3.4 Results and Discussion	43
3.4.1 Aerosol Phase Dynamics	44
3.4.2 Dynamics After Particle Deposition onto the Substrate	48
3.4.3 Photocurrent Measurements.....	52
3.5 Conclusions	54
3.6 Acknowledgements	55
3.7 References	55
Chapter 4: Nanostructured TiO₂ Film Morphology and the Performance of Dye-Sensitized Solar Cells and Photo Water Splitting	60
4.1 Abstract.....	61
4.2 Introduction	62
4.3 Experimental Methods.....	65
4.3.1 Film Synthesis.....	65
4.3.2 Film Characterization.....	67
4.3.3 Photo Water Splitting.....	68
4.3.4 Dye Sensitized Solar Cell	68
4.4 Results and Discussion	69
4.4.1 Film Synthesis.....	69
4.4.1 Photo Water Splitting.....	74
4.4.1 Dye-Sensitized Solar Cell	77
4.5 Conclusions	80
4.6 Acknowledgements	81
4.7 References	81
Chapter 5: Impact of Different Electrolytes on Photocatalytic Water Splitting	88
5.1 Abstract.....	89
5.2 Introduction	90
5.3 Experimental Methods.....	91
5.3.1 Materials	91

5.3.2 Data Collection	93
5.3.3 Electrolytes	94
5.3.4 Procedure	94
5.4 Results and Discussion	96
5.4.1 Effect of OH ⁻	96
5.4.2 Effect of Dissolved Oxygen.....	100
5.4.3 Effect of Conductivity.....	102
5.4.4 Effect of Cation and Anion Species.....	104
5.5 Conclusions	110
5.6 Acknowledgements	111
5.7 References	111
Chapter 6: Band structure of Mixed Metal Oxides: Theory and Experiment	116
6.1 Abstract.....	117
6.2 Introduction	118
6.3 Methods	122
6.3.1 Test Plan.....	122
6.3.2 MMOBS Analysis.....	121
6.3.3 DFT Calculations	125
6.3.4 Model Systems for DFT Calculations.....	126
6.3.5 Experimental	128
6.4 Results and Discussion	131
6.4.1 MMOBS Analysis.....	132
6.4.2 DFT Calculations	133
6.4.3 Nanostructured Thin Films	135
6.4.4 Confirmation of Predictions.....	137
6.4.5 Photocatalyst Design for Water Splitting	140
6.5 Conclusions	141
6.6 Acknowledgements	142
6.7 References	142

Chapter 7: Nanostructured Visible Light Active All Oxide p/n Bulk-Heterojunctions for Improved Charge Separation	149
7.1 Abstract.....	150
7.2 Introduction	151
7.3 Results and Discussion	155
7.3.1 Synthesis	155
7.3.2 Photovoltaic Characteristics.....	163
7.4 Conclusions	168
7.5 Methods	169
7.6 Acknowledgements	173
7.7 References	174
Chapter 8: Conclusions and Future Directions	181
8.1 Conclusions	181
8.2 Future Directions	184
8.2.1 Columnar Film Deposition Mechanism.....	184
8.2.2 Dye-Sensitized Solar Cells	185
8.2.3 Electrolyte Saturation Effects	185
8.2.4 Extension of MMOBS	186
8.2.4 Improvement of n-TiO ₂ /p-Cu ₂ O BHJ Cells.....	186
Appendix I: Experimental Diagrams and Digital Images	187
Appendix II: pH and Redox Thermodynamics	194
Appendix III: Curriculum Vitae	197

List of Figures

Chapter 1: Introduction

Figure 1-1: Schematic diagram of a research water splitting photocell	6
--	---

Chapter 2: Human Development and the Energy-Environment Nexus

Figure 2-1: Different primary energy resources in the energy mix of the United States and globally.....	13
--	----

Figure 2-2: HDI as a function of per capita primary energy consumption for the G20 nations.....	17
Figure 2-3: Saturation energies for the components of the HDI	19
Figure 2-4: Human development index as a function of per capita primary energy consumption for 170 nations	20
Figure 2-5: HDI as a function of per capita primary energy consumption for select nations over the time period from 1991 to 2006	21
Figure 2-6: Shift in total global primary energy consumption required to bring the world to the saturation energy, corresponding to an HDI value of 0.93	22
Figure 2-7: Shift in total global primary energy consumption as a function of global HDI.....	23
Figure 2-8: Per capita CO ₂ emission as a function of per capita primary energy consumption for 170 nations	24
Figure 2-9: Global average per capita CO ₂ emissions under different coal sequestration scenarios	26
Figure 2-10: Fraction of fossil fuels in the primary energy mix of select nations ...	27
Figure 2-11: HDI as a function of CO ₂ intensity for 170 nations showing no correlation.....	28
Figure 2-12: Total consumption of household energy for different end uses averaged over the United States	30

Chapter 3: Synthesis of Nanostructured Photoactive Films with Controlled Morphology by a Flame Aerosol Reactor

Figure 3-1: Schematic diagram of the experimental setup for deposition of nanostructured TiO ₂ films	40
Figure 3-2: Characteristic time conditions for different film deposition processes ..	45
Figure 3-3: Size measurements of particles in the aerosol phase for two TTIP feed rates.....	47
Figure 3-4: Film morphology for two TTIP feed rate for films deposited for a fixed time of 180 seconds.....	49
Figure 3-5: Average grain size measured from XRD peak broadening as a function of TTIP feed rate, for a fixed deposition time of 180 seconds.....	50
Figure 3-6: Selected side view SEM images of films showing film thickness increasing with deposition time.....	51
Figure 3-7: Film thickness plotted as a function of deposition time for 3 different TTIP feed rates.	52

Figure 3-8: Measured photocurrents.....	53
Chapter 4: Nanostructured TiO₂ Film Morphology and the Performance of Dye-Sensitized Solar Cells and Photo Water Splitting	
Figure 4-1: Schematic of the flame aerosol reactor	66
Figure 4-2: Side-view SEM image of a granular film deposited at a burner-substrate distance of 4.1 cm.....	70
Figure 4-3: Side-view SEM image of a columnar film deposited at a burner-substrate distance of 1.7 cm.....	71
Figure 4-4: Example XRD patterns for two as-prepared films, a 7.5 μm granular and a 6.9 μm columnar	72
Figure 4-5: Watersplitting photocurrent as a function of film thickness	75
Figure 4-6: Dye-sensitized solar cell performance characteristics.....	77
Figure 4-7: Measured photovoltage transients and electron lifetimes	79
Chapter 5: Impact of Different Electrolytes on Photocatalytic Water Splitting	
Figure 5-1. Schematic diagram of the experimental setup for water splitting	92
Figure 5-2. Hydrogen production rate as a function of pH	97
Figure 5-3. Hydrogen production rate as a function of conductivity	103
Figure 5-4. Hydrogen production rate as a function of pH for multiple electrolytes.	105
Figure 5-5. Energy level diagram indicating the valence and conduction band energy levels for TiO ₂ relative to certain standard reduction potentials	108
Chapter 6: Band structure of Mixed Metal Oxides: Theory and Experiment	
Figure 6-1: Crystal structures for the 5 model Ti-Fe-O compounds used in the DFT calculations.....	123
Figure 6-2: Electronic band edge positions of the Ti-Fe-O compounds determined by the MMOBS analysis using experimental basis values.....	124
Figure 6-3: Schematic of the FLAR synthesis reactor	129
Figure 6-4: Density of state plots generated from DFT calculations for the various Ti-Fe-O compounds.....	134
Figure 6-5: X-ray diffraction (XRD) patterns for the 4 experimental films	136

Figure 6-6: Normalized UV-visible absorption spectra measured by diffuse reflectance spectroscopy.....	137
Figure 6-7: Band gaps predicted by MMOBS using experimental and DFT basis values compared to that measured experimentally and predicted by DFT	138

Chapter 7: Nanostructured Visible Light Active All Oxide p/n Bulk-Heterojunctions for Improved Charge Separation

Figure 7-1: Diagram of an inorganic solid state bulk-heterojunction (BHJ) photovoltaic device.....	153
Figure 7-2: Energy level diagram of the TiO ₂ /Cu ₂ O system illustrating the conduction band (CB) and valence band (VB) positions	154
Figure 7-3: Side-view schematic showing the important physical dimensions in the device.....	158
Figure 7-4: X-ray diffraction pattern (a) and UV-visible absorption spectra (b) for 2.3 μm TiO ₂ columns with and without Cu ₂ O	159
Figure 7-5: Side view SEM images of TiO ₂ columns for cells 1-4 before (a1-4) and after (b1-4) Cu ₂ O deposition	161
Figure 7-6: Side view SEM images (a) and elemental maps (b) taken by X-EDS illustrating the inter-penetrating nature of the n-TiO ₂ /p-Cu ₂ O interface.....	162
Figure 7-7: I-V curves measured as a function of BHJ thickness (L_{BHJ}) under simulated AM1.5 G illumination (a) and rectifying characteristics of cells 1 and 4 in the dark (b)	164
Figure 7-8: Schematic illustrating the proposed difference between the depletion region in a BHJ device and a planer device	166
Figure 7-9: Short circuit photocurrent density as a function of BHJ thickness (L_{BHJ}) under simulated AM1.5 G illumination showing the saturation of the photocurrent when $L_{BHJ} \sim L_{ABS}$	167

Appendix I

Figure I-1: Schematic of the premixed flame aerosol reactor (FLAR)	188
Figure I-2: Digital image of the premixed flame aerosol reactor (FLAR).....	189
Figure I-3: Digital image of the sampling for aerosol size distribution measurements by SMPS in Chapter 3. The probe is a primary dilution probe	190
Figure I-4: Digital image of the water splitting photocell.....	191

Figure I-5: Digital image of the solar simulator used for photovoltaic testing in Chapter 7	192
Figure I-6: Comparison of the spectral output of the solar simulator to the AM1.5G standard.....	193

Appendix II

Figure II-1: Trend in potential with pH for the band positions of TiO ₂	196
---	-----

List of Tables

Chapter 2: Human Development and the Energy-Environment Nexus

Table 2-1: Summary of the parameters for equation (2-5) obtained from saturation curve fitting to the G20 data	19
---	----

Chapter 3: Synthesis of Nanostructured Photoactive Films with Controlled Morphology by a Flame Aerosol Reactor

Table 3-1: Summary of experimental parameters and results	43
Table 3-2: Summary of estimated characteristic times encountered in the aerosol phase	46

Chapter 4: Nanostructured TiO₂ Film Morphology and the Performance of Dye-Sensitized Solar Cells and Photo Water Splitting

Table 4-1: Summary of the dye-sensitized solar cell performance metrics for cells constructed using different TiO ₂ films	78
---	----

Chapter 5: Impact of Different Electrolytes on Photocatalytic Water Splitting

Table 5-1. Experimental outline	95
--	----

Chapter 6: Band structure of Mixed Metal Oxides: Theory and Experiment

Table 6-1: Summary of the atomic concentrations and crystalline phases of the various experimental films	130
---	-----

Chapter 7: Nanostructured Visible Light Active All Oxide p/n Bulk-Heterojunctions for Improved Charge Separation

Table 7-1: Summary of the relevant physical dimensions of each BHJ device. For comparison, the light absorption depth is approximately 2.0 μm	162
Table 7-2: Summary of the photovoltaic characteristics of each cell measured under simulated AM1.5G illumination.....	164

ABSTRACT OF THE DISSERTATION

Metal Oxide Semiconductors for Solar Energy Harvesting

by

Elijah James Thimsen

Doctor of Philosophy in Energy, Environmental and Chemical Engineering

Washington University in Saint Louis, 2009

Professor Pratim Biswas, Chairperson

The correlation between energy consumption and human development illustrates the importance of this societal resource. We will consume more energy in the future. In light of issues with the status quo, such as climate change, long-term supply and security, solar energy is an attractive source. It is plentiful, virtually inexhaustible, and can provide more than enough energy to power society. However, the issue with producing electricity and fuels from solar energy is that it is expensive, primarily from the materials (silicon) used in building the cells. Metal oxide semiconductors are an attractive class of materials that are extremely low cost and can be produced at the scale needed to meet widespread demand. An industrially attractive thin film synthesis process based on aerosol deposition was developed that relies on self-assembly to afford rational control over critical materials parameters such as film morphology and nanostructure. The film morphology and nanostructure were found to have dramatic effects on the performance of TiO₂-based photovoltaic dye-sensitized solar cells. Taking a cue from nature, to overcome the spatial and temporal mismatch between the supply of sunlight and demand for energy consumption, it is desirable to produce solar fuels such as hydrogen from

photoelectrochemical water splitting. The source of water is important -- seawater is attractive. The fundamental reaction mechanism for TiO₂-based cells is discussed in the context of seawater splitting. There are two primary issues with producing hydrogen by photoelectrochemical water splitting using metal-oxide semiconductors: visible light activity and spontaneous activity. To address the light absorption issue, a combined theory-experiment approach was taken to understand the fundamental role of chemical composition in determining the visible light absorption properties of mixed metal-oxide semiconductors. To address the spontaneous activity issue, self-biasing all oxide p/n bulk-heterojunctions were synthesized and the nanostructure was systematically varied to understand the fundamental role of various characteristic length scales in the nanostructured region of the device on performance. The conclusion of this work is that solar energy harvesting by metal oxide semiconductors is highly promising. All of the scientific concepts have been proven, and steady gains in efficiency are being achieved as researchers continue to tackle the problem.

Chapter 1:

Introduction

1.1 Overview

There is a pressing need for abundant, environmentally benign renewable energy. Concepts developed by aerosol science, nanotechnology, biomimicry and quantum chemistry provide an opportunity to develop new tools to attack this problem, which has been lingering since the 1970s. The territory is in the early stages of exploration, and this thesis serves to identify main challenges and provide successful examples of how relatively recent concepts can provide new tools and vistas on pressing technological issues. This thesis presents work at many different scales and across disciplines, with different challenges requiring different approaches. Thus detailed literature reviews identifying the specific knowledge gaps are presented in the individual chapters.

1.2 Problem Statement

The world is consuming an ever-increasing amount of energy. The increase is driven by population growth and improvement in human development around the world. Chapter 2 describes the relationship between energy consumption and human development in a pseudo quantitative manner. It then goes on to estimate the increase in energy consumption resulting from the developing world increasing its quality of life, and also estimates the efficiency gains that can be reasonably achieved in the developed world. The net result is that efficiency gains in the developed world cannot provide enough energy to meet the needs of the developing world, and thus global consumption will likely increase, potentially resulting in a more than doubling of global energy consumption.

In light of climate change, where this energy will come from is of utmost importance. The main anthropogenic driver of climate change is the carbon dioxide that is released to the atmosphere through the combustion of fossil fuels¹. Interestingly, despite the intimate relationship of energy consumption to human development, it appears as though there is no correlation between human development and the carbon dioxide intensity of a country's primary energy mix (Chapter 2). The important parameter is the *amount of primary energy consumed*. It appears as though the source of the energy is less important. To meet growing demand and reduce anthropogenic CO₂ emissions, we must develop zero-emission sources.

One approach is to capture and sequester the carbon produced through the combustion of fossil fuels, in carbon capture and storage (CCS) systems. Implementing a worldwide CCS system would be a formidable undertaking, requiring a global infrastructure to be developed that is nonexistent at the moment. Approximately 40 % of global CO₂ emissions come from the combustion of petroleum products (Chapter 2). Unfortunately, carbon capture is virtually impossible from personal automobiles. Thus a fossil-fuel based zero-emission system would also require the use of electric vehicles so the combustion byproducts could be captured at the point source (power plants).

Another approach is nuclear fission to produce electricity, coupled to the use of electric vehicles. This is a very attractive approach, except for one critical issue: the long-lived radioactive waste that is produced. A palatable solution for the waste issue has yet to be developed. There are also logistical concerns about building the nuclear power plants fast enough to meet demand².

While energy will undoubtedly continue to be produced from a mixture of sources in the future, by far the most attractive solution is renewable energy. Of the renewable sources, the most plentiful is solar energy. More energy in sunlight is incident on the earth in an hour than the entire global society consumes in a year³. Harvesting this resource would require large areas to be covered, but they are finite. For instance, if solar energy is harvested directly by photovoltaic panels, the area required to meet the United States energy needs would be less than 1/4 of the total area covered by roads and streets in the country³. The main issue is the cost of the energy produced by current photovoltaic technology is 5 to 10 times higher than fossil fuel alternatives.

Approximately half of the cost of the incumbent solar energy technology comes from the crystalline silicon in photovoltaic panels, which produce electricity when illuminated by sunlight. The majority of the remainder of the cost comes from human labor, which can be assumed to come down with economies of scale. Thus an effective way to attack the cost issue is by exploring alternative materials.

1.3 Approach

Metal oxide semiconductors are an attractive class of materials. They are very low cost, typically quite stable and can be made in large volumes. For instance, titanium dioxide (TiO₂) is produced in quantities of tons per hour by flame-based processes⁴ for use as paint pigment. Meanwhile, silicon is produced in relatively small quantities for high-technology applications like the microelectronic chips in personal electronics. For economical widespread solar energy harvesting, it is clear that the materials should more closely resemble paint than highly refined electronics. For solar cell applications, metal

oxide semiconductors are typically immobilized as a thin film with a thicknesses on the order of 100 nanometers to 10 micrometers.

The synthesis of metal oxide thin films is discussed in Chapter 3. Upon review of the literature, it was determined that existing synthesis processes for metal-oxide thin films were not amenable for industrial production of materials for solar energy harvesting. This motivated the development of a flame aerosol reactor (FLAR), which is simple, scalable, high throughput and affords rational control over nanostructure. The FLAR was used to synthesize TiO₂ thin films with well-controlled morphology and thickness as an example, although the process can be used to synthesize a variety of metal oxide materials for which suitable precursors are available.

Nanostructuring affords a powerful tool for tuning device performance. In Chapter 4, the FLAR was used to synthesize TiO₂ films for use in photovoltaic dye-sensitized solar cells^{5, 6} and photo water splitting cells with controlled nanostructure. It was found that the power conversion efficiency of these solar cells can change by a factor of 10 to 50 depending on the nanostructure, underscoring the need to rationally control this property and the potential as a tool to extract higher performance out of low cost materials.

Taking a cue from nature, it is highly desirable to store the energy in sunlight in chemical bonds so it can be used on demand. One way to do this is by splitting water into hydrogen and oxygen, which is typically accomplished using a wide-gap photo catalyst such as TiO₂^{7, 8}. An example of a research photocell for water splitting is presented in Figure 1-1. The photoanode is composed of TiO₂ deposited on an

electrically conductive substrate, which is connected through an external circuit to a counter electrode (cathode). Upon illumination by photons with an energy greater than the band gap (3.0 eV for TiO_2), which are in the UV portion of the spectrum for TiO_2 , water is oxidized by photo-generated holes at the TiO_2 surface, and aqueous protons are reduced to hydrogen gas at the counter electrode. A small electrical bias is applied in the external circuit to enhance the extraction of electrons from the TiO_2 film. The energy inputs to the cell are the photons from the lamp and electrical energy from the applied voltage, with the energy output being hydrogen gas. There are several fundamental issues that need to be addressed to scale up such a device, which are discussed below.

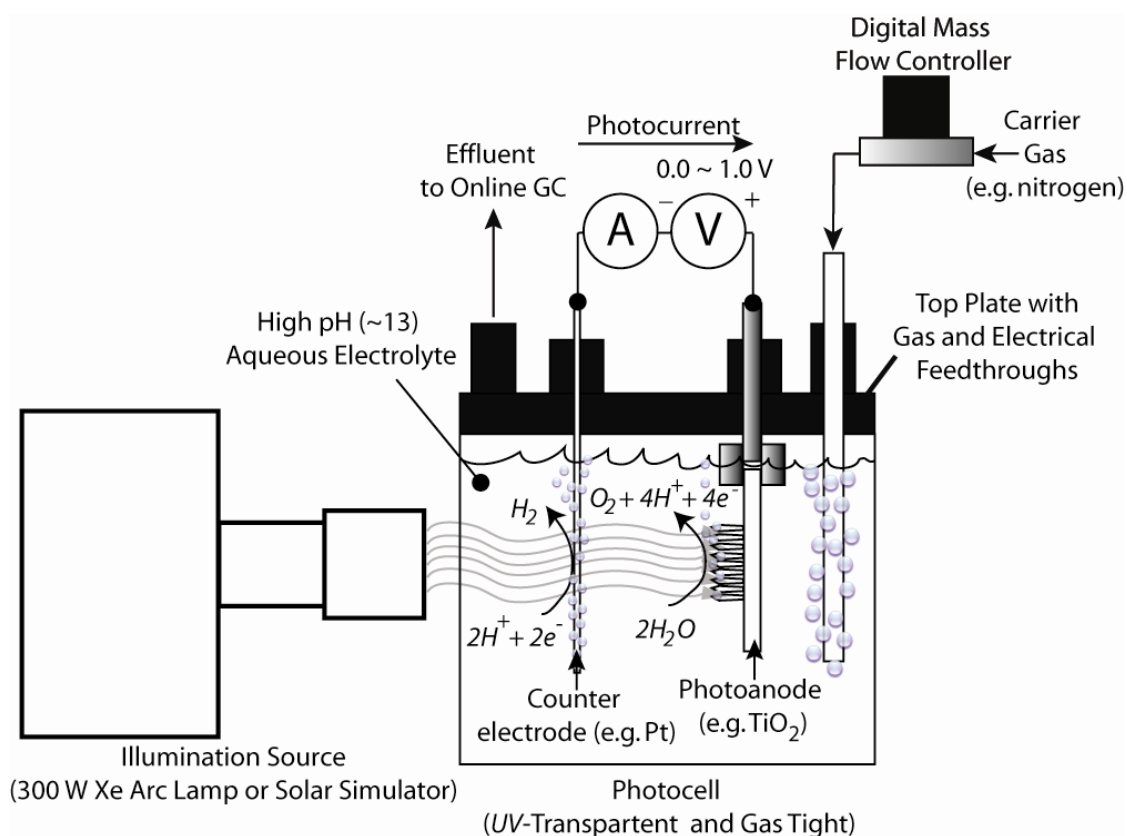


Figure 1-1: Schematic diagram of a research water splitting photocell.

For widespread production of hydrogen by photo water splitting, the source of water is important. Chapter 5 discusses the reaction mechanism of photo-induced water splitting on TiO_2 , and its relationship to the composition of the aqueous electrolyte, in the context of using seawater as a chemical feedstock.

One of the principal challenges in achieving efficient, which means greater than 10% sunlight-to-hydrogen power conversion efficiency⁸, photocatalytic water splitting via metal oxide semiconductors is driving the reaction using visible light. There are no known materials that can do it. Researchers are increasingly exploring mixed metal-oxide photocatalysts. Taking a combined theory-experiment approach, Chapter 6 discusses the role of chemical composition in the electronic band structure of mixed metal oxide materials, which determines the light absorption properties of a semiconductor and its thermodynamic ability to split water.

Another key challenge in splitting water by metal oxide photocatalysts is eliminating the need for external electrical biases (Figure 1-1), which are used to enhance charge collection and prevent parasitic processes such as charge recombination. It has been reported for cost-intensive non-oxide materials that monolithic p/n junction devices can be used to provide an internal bias to eliminate the need for external inputs. Indeed, this approach has yielded one of the most efficient self-biased devices reported to date⁹. Chapter 7 discusses the synthesis of a nanostructured all-oxide p/n junction between n- TiO_2 and p- Cu_2O towards these ends. The structures are explored as photovoltaics to determine their charge separation characteristics, although they could serve as "building blocks" for fabricating a monolithic watersplitting device in the future, as both materials meet the thermodynamic requirements to split water. Also in Chapter 7, nanostructuring

is again found to improve the device performance and the critical parameters are identified.

1.4 Conclusion

While a device configuration that yielded greater than 10% sunlight-to-hydrogen conversion efficiency was not identified over the course of this work, fundamentally new concepts and design tools were developed that lay the foundation for future work to venture into new areas in which, perhaps, the big breakthrough is hidden.

1.5 References

1. Solomon, S.; Qin, D.; Manning, M.; Marquis, M.; Averyt, K.; Tignor, M.; Miller, H. L.; Chen, Z. *IPCC Fourth Assessment Report: The Physical Science Basis*; International Panel on Climate Change: **2007**.
2. Lewis, N. S.; Nocera, D. G., Powering the planet: Chemical challenges in solar energy utilization. *Proceedings of the National Academy of Sciences of the United States of America* **2006**, 103, (43), 15729-15735.
3. Turner, J. A., A realizable renewable energy future. *Science* **1999**, 285, (5428), 687-689.
4. Strobel, R.; Pratsinis, S. E., Flame aerosol synthesis of smart nanostructured materials. *Journal of Materials Chemistry* **2007**, 17, (45), 4743-4756.
5. Oregan, B.; Gratzel, M., A Low-Cost, High-Efficiency Solar-Cell Based on Dye-Sensitized Colloidal TiO₂ Films. *Nature* **1991**, 353, (6346), 737-740.
6. Gratzel, M., Photoelectrochemical Cells. *Nature* **2001**, 414, 338 - 344.

7. Fujishima, A.; Honda, K., Electrochemical Photolysis of Water at a Semiconductor Electrode. *Nature* **1972**, 238, 37.
8. Nowotny, J.; Sorerell, C. C.; Sheppard, L. R.; Bak, T., Solar-hydrogen: Environmentally safe fuel for the future. *International Journal of Hydrogen Energy* **2005**, 30, 521-544.
9. Khaselev, O.; Turner, J. A., A Monolithic Photovoltaic-Photoelectrochemical Device for Hydrogen Production via Water Splitting. *Science* **1998**, 280, 425-427.

Chapter 2:

Human Development and the Energy- Environment Nexus

2.1 Abstract:

Energy consumption is intimately related to human development and quality of life. To improve quality of life, the developing world will consume much more energy than it does today. A detailed understanding of how much the developing world will need is critical, especially in light of climate change. A saturation model is developed to relate the human development index (HDI), which describes the education level, health care and material wealth of a nation in a pseudo-quantitative manor, to per capita primary energy resource consumption. It is found that the HDI saturates at a per capita energy consumption of 52,430 kWh year⁻¹ capita⁻¹. The life expectancy and education indices saturate at a lower per capita primary energy consumption than the GDPpc index. Strong evidence is presented that the amount of primary energy that will be required in the developing world will result in a more than doubling of current global capacity, by far exceeding gains that can be achieved by energy efficiency improvements in the developed world. However, since the developed world currently consumes the most energy, implementing efficiency improvements can have immediate impacts on emissions, providing a bridge while a comprehensive plan for the developing world is formulated. The results are discussed in the context of carbon dioxide emissions, which is a critical driver in dealing with these issues.

2.2 Introduction

Energy use is critical to all forms of life, and especially to human societies. Biologically we need the energy in food to stay alive and reproduce. The human body needs on average $2,000 \text{ kcal person}^{-1} \text{ day}^{-1}$ ($2.36 \text{ kWh person}^{-1} \text{ day}^{-1}$) of energy to sustain itself. In the United States (and many other developed nations) people consume as much as $229,000 \text{ kcal person}^{-1} \text{ day}^{-1}$ ($266 \text{ kWh person}^{-1} \text{ day}^{-1}$) of primary energy resource. From a macroscopic perspective, this extra energy consumption has been attributed to the thermodynamic requirement to maintain the complex organization of modern societies¹, which are far from the equilibrium disordered state. In terms of people in the society, this extra energy consumption represents an improvement in quality of life, which means better access to education, longer life spans and higher income.

Much of the world is energy impoverished. Out of 6.7 billion people in the world, 1.6 billion people are living with no access to electricity, and approximately 2.4 billion people are using wood, charcoal and dung as their principle source of energy². As people in the developing world strive to improve their quality of life, they will consume more energy. Indeed, as China has brought 400 million people in its own country out of poverty over the last 30 years³, it has come with a commensurate increase of $11,000 \text{ kWh year}^{-1} \text{ capita}^{-1}$ (320% increase) in primary energy consumption and an additional $3.1 \text{ metric tons year}^{-1} \text{ capita}^{-1}$ of CO_2 emission over the same time period. As the world's poor climb out of poverty, a detailed understanding of the additional energy resources that will be consumed is needed, so the process can be guided to be efficient and to avoid adverse environmental impacts.

The developed world need not decrease its quality of life, only operate more efficiently and switch to environmentally benign sources of energy. Accounting for roughly 22% of the global primary energy consumption, the United States (US) is conspicuous on the global energy stage. The average density in metropolitan areas with total populations greater than 500,000 (50% of the population) in the United States is 1,100 people km⁻², while in Japan it is 10,900 people km⁻², and Western Europe is 7,700 people km⁻².⁴ Low population density leads to additional transportation expenditures. The average automobile fuel economy in the United States is 11 km liter⁻¹ (25 miles gallon⁻¹), while in Europe and Japan it is approximately 17 km liter⁻¹ (40 miles gallon⁻¹)⁵, leading to increased petroleum consumption over the long transportation distances that are required by the large metropolitan areas. The net result is an approximately two times higher per capita energy consumption in the US (97,100 kWh year⁻¹ capita⁻¹) compared to other developed nations such as Japan (52,000 kWh year⁻¹ capita⁻¹) and Germany (51,600 kWh⁻¹ year⁻¹ capita⁻¹). The distribution of where this energy comes from in the US and globally is illustrated in Figure 2-1.

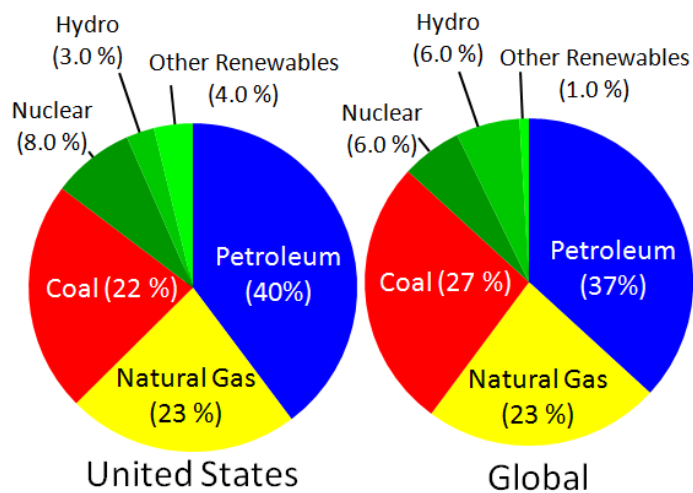


Figure 2-1: Different primary energy resources in the energy mix of the United States and globally.

The role of energy in development is not well understood. It is, however, well known that the Gross Domestic Product (GDP) of a nation is correlated to total energy consumption. And since the majority of the primary energy consumed globally comes from fossil fuels (Figure 2-1), GDP is also correlated to CO₂ emission. While GDP is related to the development of a nation, use of this quantity as the only indicator provides a distorted picture. A better measure, although still not perfect, is the Human Development Index (HDI).

The HDI is a pseudo quantitative measure that was first proposed in 1990⁶. The HDI quantifies human development by considering school enrollment and literacy rates as a measure of education, life expectancy as a measure of health care, and per capita GDP based on purchasing power parity (ppp) as a measure of material wealth. The HDI is an average of three component indices: the education index (EDUI), life expectancy index (LEI) and per capita gross domestic product index based on purchasing power parity (GDPpci)⁷:

$$HDI = \frac{EDUI + LEI + GDPpci}{3} \quad (2-1)$$

Each index takes a value between 0 (minimum development) and 1 (maximum development). The education index is calculated according to the following equation:

$$EDUI = \frac{1}{3} \left(\frac{Gross\ Enrollment\ Index - 0}{100 - 0} \right) + \frac{2}{3} \left(\frac{Adult\ Literacy\ Index - 0}{100 - 0} \right) \quad (2-2)$$

Where the gross enrollment index is the percentage of the school-aged population in a given country that is enrolled in school, and the adult literacy index is the percentage of the adult population that can read and write. The life expectancy index for a given country is calculated by:

$$LEI = \left(\frac{Life\ Expectancy - 25\ years}{85\ years - 25\ years} \right) \quad (2-3)$$

Where 85 years the goalpost for average human life expectancy, and 25 years is the lower limit. The GDPpc index is calculated by:

$$GDPpcI = \left(\frac{\log(GDPpc) - \log(100)}{\log(40,000) - \log(100)} \right) \quad (2-4)$$

Where GDPpc is the per capita GDP (\$US ppp) of a given country. The use of a log scale is used to calculate *GDPpcI* because an unlimited productivity is not necessary to achieve a higher human development level⁸.

A few studies have been conducted that correlate HDI to energy consumption⁸⁻¹⁰. Pasternek observed there is a saturation in HDI after a critical electricity consumption level by fitting a logarithmic growth function, and then calculated the cost in terms of increased electricity consumption to shift the world to this level⁹. However, it is more relevant to correlate HDI to primary energy consumption, as energy is used in more forms than just electricity. Dias et al.⁸ and Martinez and Ebenhack¹⁰ observed a similar trend of HDI saturation with increased total energy consumption. In addition, Dias et al.⁸ noted that a net global energy savings of approximately 30% could be achieved by shifting all nations to an energy consumption level with a commensurate HDI of 0.9. While some preliminary observations have been made, a detailed understanding of the relationship of primary energy consumption to HDI has not been developed. Furthermore, the consequences for global development and CO₂ emission remains absent from the literature.

2.3 Methods

The goal of this paper is to elucidate the role of energy consumption in the development process. Energy data was collected from the Energy Information Agency¹¹,

population data from the United States Census Bureau¹² and HDI data from the annual reports of the United Nations Development Program⁷. The term energy consumption refers to *primary energy consumption* which is the amount of primary energy resource such as, petroleum, natural gas or coal, that is consumed by a given country. Primary energy consumption is in contrast to the useable energy produced (e.g. electricity, transportation) which is lower than the primary energy consumption by an efficiency factor. Unless otherwise stated, all parameters in this paper are reported per capita (person) to facilitate comparisons between countries with different populations.

Here it is proposed to use a new saturation model (Equation 2-5) to describe the increase in HDI with per capita primary energy consumption. This model is widely used in biology to model growth that experiences saturation, and also in chemistry to model saturation-limited adsorption phenomena.

$$I = \frac{I_s E}{K_I + E} \quad (2-5)$$

where I is the value of the index (HDI, EDUI, LEI or GDPpcI) at an energy consumption E , I_s is the saturation value of the index at large energy consumptions and K_I is an energy constant that is defined as the energy at which the index I has attained 50% of its maximum value (*i.e.* $I = 0.5 I_s$ when $E = K_I$). At small values of E , I increases linearly with a slope of I_s/K_I ; and at large values of E , I is constant, independent of E and equal to I_s .

2.4 G20 Nations

The HDI is plotted as a function of per capita primary energy consumption for the G20 nations in Figure 2-2, along with a regression performed using equation (2-5). The

HDI increases with per capita energy consumption until reaching a saturation point, after which it remains roughly constant. The three outliers (South Africa, Russia and Saudi Arabia) were excluded from the data for the regression. Fitting equation (2-5) gave a better R^2 value (2 parameter, 0.93) than either an exponential rise to maximum function (2 parameter, $R^2 = 0.67$) or a logarithmic growth function (2 parameter, $R^2 = 0.91$). The results of the fit are presented in Table 2-1.

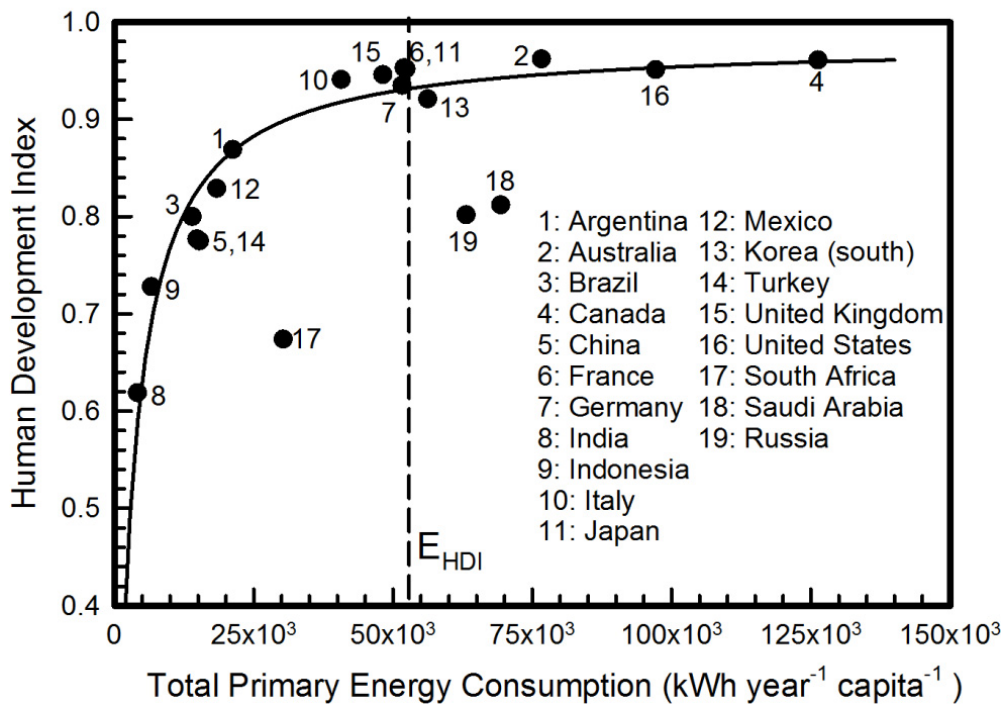


Figure 2-2: HDI as a function of per capita primary energy consumption for the G20 nations.

Once the fit parameters have been obtained for equation (2-5), the saturation point can be rigorously defined. The saturation point is defined as the energy value at which the index I has obtained 95% of its maximum value. The energy at which saturation occurs is proportional to the energy constant K_I , and can be calculated using the following equation:

$$E_I = \frac{0.95}{0.05} K_I \quad (2-6)$$

Inserting the values for the HDI from Table 2-1 yields a saturation energy of 52,430 kWh year⁻¹ capita⁻¹, which corresponds to an HDI value of 0.93. There are several countries in the G20 that are operating near the saturation point: France, Germany, Japan, Korea (south) and the United Kingdom, while several countries are operating at energy consumptions much higher than the saturation energy: Australia, the United States, Canada, Saudi Arabia and Russia. There are many countries that are consuming less than the saturation energy, including the three highly populous countries: China, India and Indonesia.

Different development activities have different energetic requirements. In other words, different levels of energy consumption are required in order to saturate different aspects of human development. The saturation energies for the different components of the HDI can be determined by fitting equation (2-5) to each of the HDI component indices separately (Figure 2-3, Table 2-1). The saturation energies of the education index and the life expectancy index are similar. However, the saturation energy for the GDPpc index is much larger. Assuming that the indices are independent, this result could mean that achieving a high level of education and high life expectancy in a country requires lower energy consumption than achieving a large GDPpc.

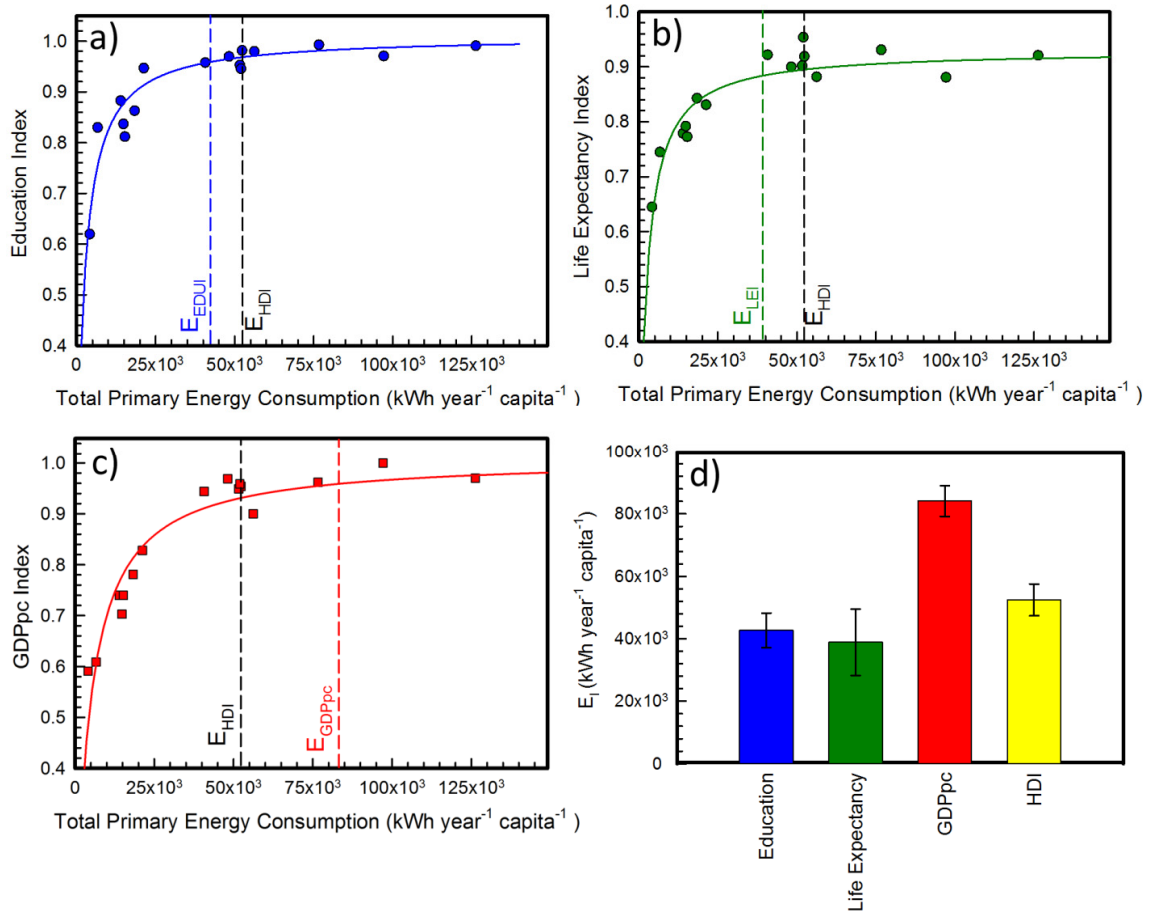


Figure 2-3: Saturation energies for the components of the HDI as a function of per capita primary energy consumption: (a) education index, (b) life expectancy index and (c) GDPpc index. (d) Comparison of the different saturation energies for each index.

Table 2-1: Summary of the parameters for equation (2-5) obtained from saturation curve fitting to the G20 data

Index (I)	I_s	K_I (kWh year ⁻¹ capita ⁻¹)	E_I (kWh year ⁻¹ capita ⁻¹)	R^2 of fit
HDI	0.98 ± 0.01	$2,759 \pm 266$	$52,430 \pm 5,060$	0.93
EDUI	1.0 ± 0.00	$2,248 \pm 290$	$42,706 \pm 5,500$	0.88
LEI	0.93 ± 0.01	$2,047 \pm 259$	$38,891 \pm 4,930$	0.88
GDPpcI	1.0 ± 0.02	$4,427 \pm 560$	$84,122 \pm 10,000$	0.91

2.5 Global Perspective

Nations can be categorized according to their energy consumption relative to the saturation energy and according to their HDI values (Figure 2-4). It is evident that the developing world is seeking to improve its quality of life, which is reflected in ever-increasing HDI values and per capita primary energy consumption. Plotted in Figure 2-5 is HDI as a function of per capita primary energy consumption for India, China, Portugal, South Korea and the United States over the time period from 1991 to 2006. These countries follow the saturation curve towards higher development levels by increasing their energy consumption, until reaching a high development level (the United States) when the per capita primary energy consumption remains roughly constant.

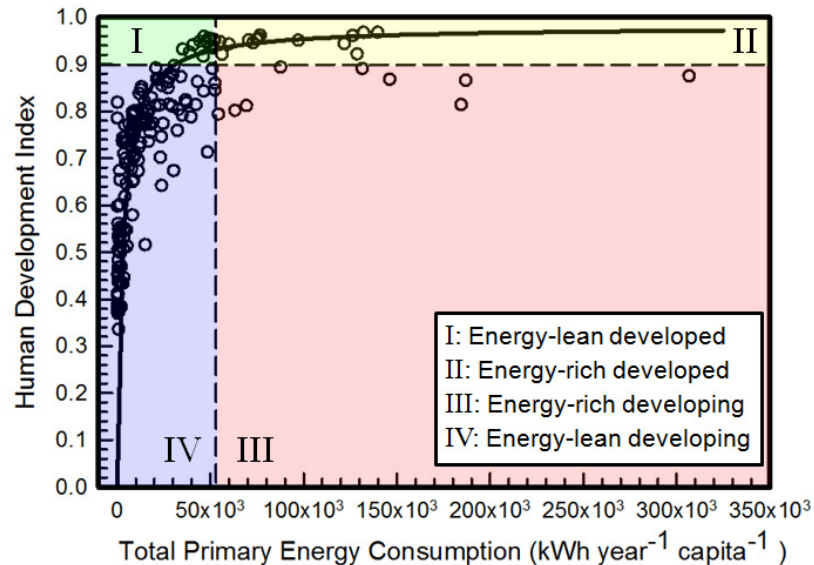


Figure 2-4: Human development index as a function of per capita primary energy consumption for 170 nations. The parameters for the saturation curve were taken from the G20 fit.

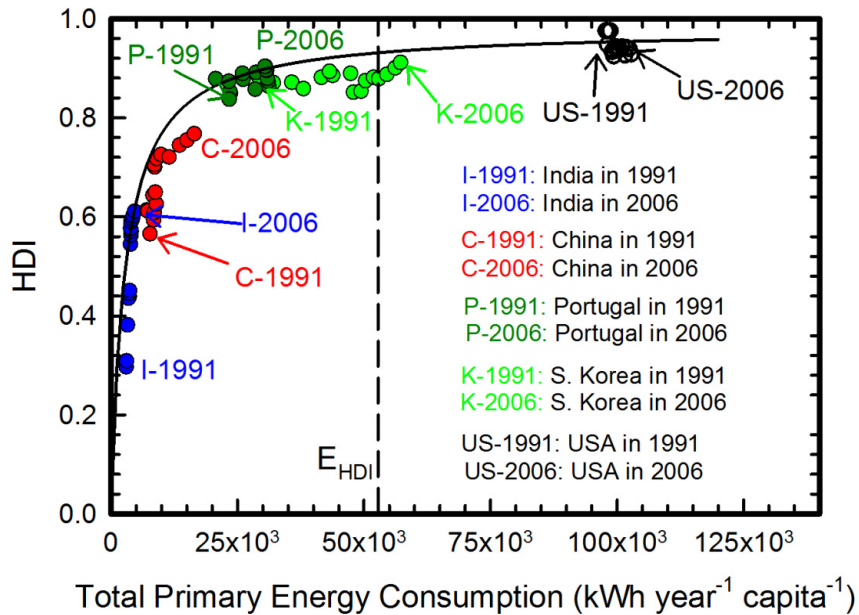


Figure 2-5: HDI as a function of per capita primary energy consumption for select nations over the time period from 1991 to 2006. Each point corresponds to a single year.

At this point, one can ask the question: what will it take for the entire world to be developed? One way to answer this question is in terms of the primary energy consumption that would be required if every person in the world lived in a country that had a per capita primary energy consumption equal to the saturation energy. The shift in primary energy consumption for every nation to move to the saturation energy can be calculated by the following equation:

$$\Delta E = \sum_{all\ nations} P_i (E_{HDI} - E_i) \quad (2-7)$$

Where ΔE is the total shift in global primary energy consumption, P_i is the population and E_i is the per capita primary energy consumption of country i . The shift in primary energy consumption for the different groups of countries is plotted in Figure 2-6. From Figure 2-6, it can be seen that to develop the entire world to the saturation energy, the increase in consumption in the developing world would be larger than efficiency gains

that could be achieved in the developed world by bringing the energy-rich countries down in energy consumption to the saturation point.

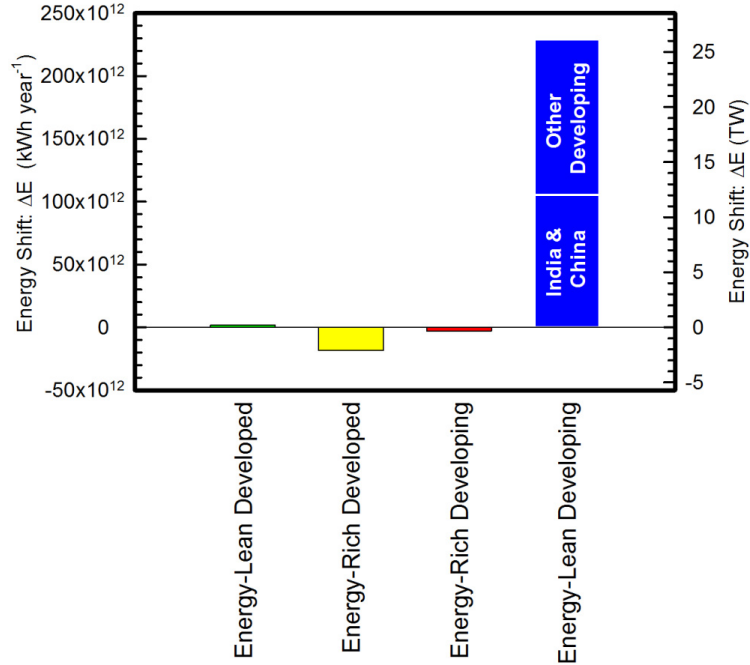


Figure 2-6: Shift in total global primary energy consumption required to bring the world to the saturation energy, corresponding to an HDI value of 0.93.

The total additional primary energy consumption required for every nation in the world to shift to the saturation energy is approximately $210 \times 10^{12} \text{ kWh year}^{-1}$, which is 1.6 times higher than the total global primary energy consumption today. This means that global primary energy consumption would have to more than double for every nation to develop to the saturation point, at current population levels.

One can ask a second question: what is the shift in total global primary energy consumption for the world to move to an arbitrary HDI value? Solving equations (2-5) and (2-7) yields:

$$\Delta E = \sum_{all\ nations} P_i (E - E_i) = \sum_{all\ nations} P_i \left(\frac{K_{HDI} * HDI}{HDI_s - HDI} - E_i \right) \quad (2-8)$$

The energy shift as a function of global HDI is plotted in Figure 2-7. It can be seen from this plot that every nation in the world could shift to an HDI value of 0.87 with no additional primary energy consumption. If every nation in the world shifted to an even lower HDI, then the global population could actually consume less energy than it does today. Looked at another way, if in the future the world's primary energy consumption is forced down too far by resource scarcity, or some other driver, it can be expected that the global community will start reducing its development level, illustrating the critical importance of developing sustainable sources of primary energy.

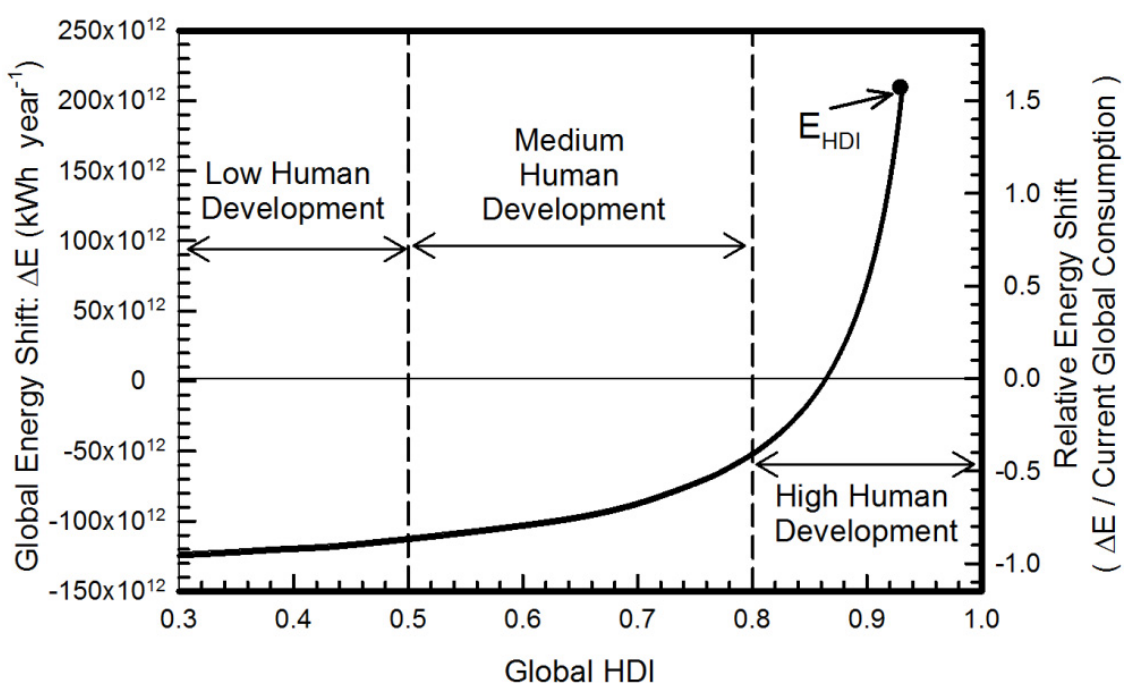


Figure 2-7: Shift in total global primary energy consumption as a function of global HDI. Negative values correspond to energy savings and positive values correspond to increases in energy consumption.

Further complicating the picture is the world population. The global population is projected to grow from its current value of 6.7 billion people to a 8 billion in 2028, and 9

billion in 2048¹². Thus the total global energy consumption will increase from development to the saturation point (210×10^{12} kWh year⁻¹ for the current population) and from population growth (282×10^{12} kWh year⁻¹ for 9 billion people in 2048).

2.6 Carbon Dioxide Emissions

The increase in energy consumption presents a significant challenge in light of climate change. Currently, the global community derives its primary energy from fossil fuels, which adversely affect global climate change. While the carbon intensity depends on the specific type of fuel, the average carbon intensities for coal, petroleum and natural gas are 322 g CO₂ kWh⁻¹, 244 g CO₂ kWh⁻¹ and 181 g CO₂ kWh⁻¹ respectively¹³. Carbon dioxide emission as a function of primary energy consumption for the countries of the world is plotted in Figure 2-8. It can be clearly seen from Figure 2-8 that as primary energy consumption goes up, so does CO₂ emission, due to the fossil fuels that are consumed.

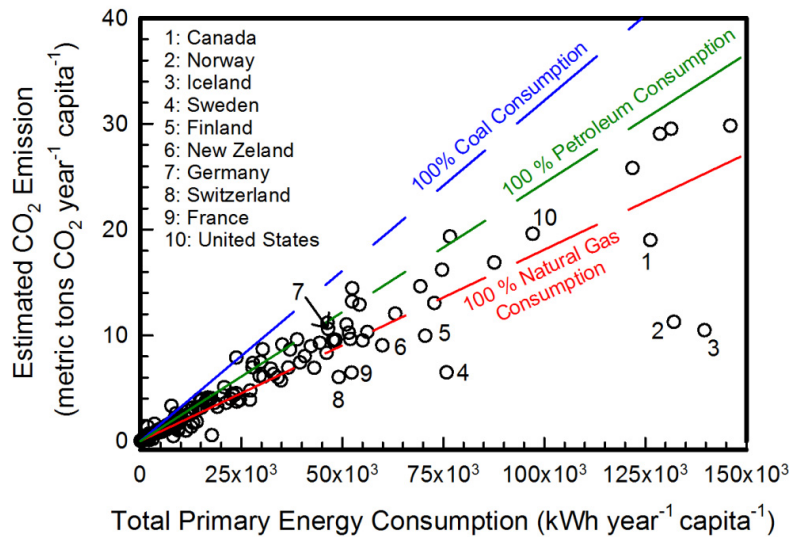


Figure 2-8: Per capita CO₂ emission as a function of per capita primary energy consumption for 170 nations.

Part of this CO₂ comes from the combustion of coal. As part of the "Clean Coal" movement, it has been proposed to sequester the emissions from coal plants. By subtracting off the contribution of coal-derived CO₂ from total CO₂ emission, the effect of these sequestration policies on CO₂ emission can be examined. The global population-averaged per capita CO₂ emissions under different sequestration scenarios for coal are presented in Figure 2-9. Sequestration of 50% of all coal-derived CO₂ yields a 22% drop in global CO₂ emissions, while 100% sequestration of coal-derived CO₂ yields a 44% drop. Large amounts of petroleum and natural gas are consumed (Figure 2-1), and even though the carbon intensity of natural gas and petroleum are smaller than coal, the net emissions are equal to or greater than that of coal. Thus the focus of CO₂ remediation efforts must be expanded beyond coal if the CO₂ emission from fossil fuels is to be addressed. Transferring transportation energy consumption from individual automobiles to centralized CCS-equipped electric plants while using electric cars or biofuels, which typically require large energy inputs¹⁴, could have large benefits to displace the CO₂ emitted by petroleum.

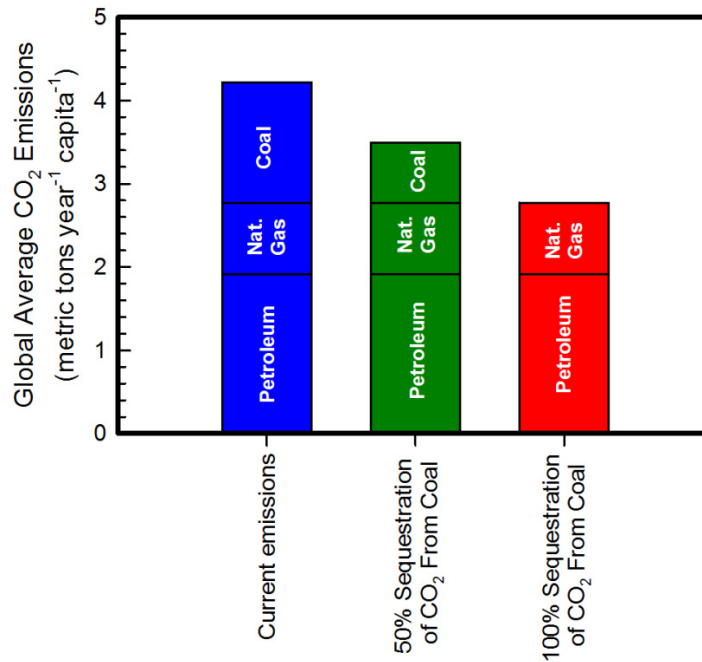


Figure 2-9: Global average per capita CO₂ emissions under different coal sequestration scenarios

Not all of the countries in the world have high CO₂ intensities. Indeed, there are several countries that have large amounts of carbon-free energy in their energy mix (Figure 2-10). Iceland has large contributions from geothermal power, Norway has large amounts of hydroelectric, Sweden has large contributions of renewable energy and nuclear, and France has large amounts of nuclear. In many cases, these countries can supply such a large fraction of their primary energy from renewable sources due to relatively small populations. However, it appears as though there is no correlation between CO₂ intensity and human development (Figure 2-11).

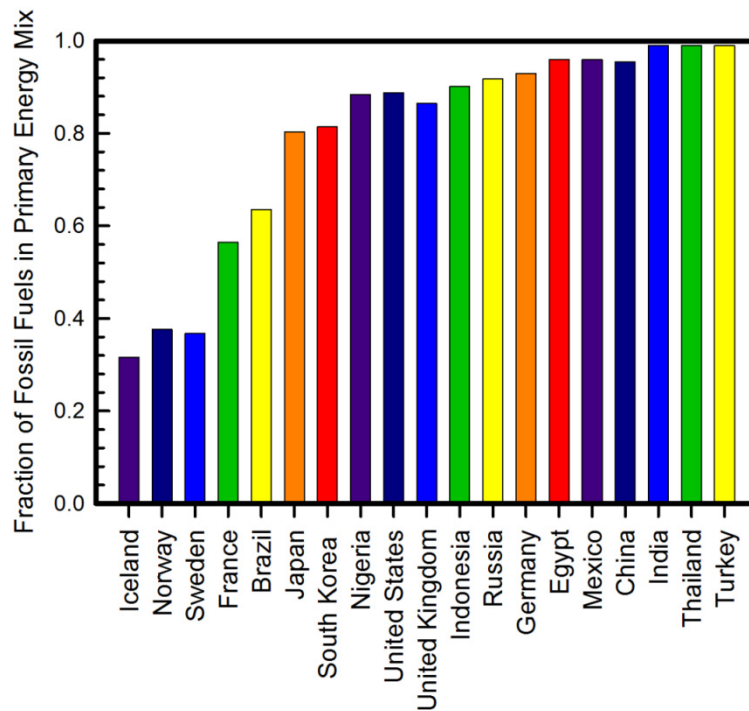


Figure 2-10: Fraction of fossil fuels in the primary energy mix of select nations.

The critical factor in determining HDI is the *amount of per capita primary energy consumed*. The world is developing, and more energy will be consumed in the future than is today. Nuclear fission plants could continue to be developed, although there are logistical concerns and very daunting challenges about what to do with the waste. Of the renewable sources, solar energy is the most attractive one that is capable of meeting, and even exceeding global energy demands¹⁵. More energy in the form of sunlight strikes the earth in an hour than is consumed by the global society in a year¹⁶. The resource is diffuse, however, necessitating large areas to be covered. There is also both a temporal and spatial mismatch between the supply of sunlight and energy demand, necessitating storage and transportation of the energy. While manufacturing and sales of photovoltaic solar panels are growing exponentially, they still provide less than 1% of the energy

consumed globally. The main barrier to widespread implementation is the cost of the energy produced, which remains 5-10 times higher than fossil alternatives¹⁵. Bringing the cost of solar-produced energy down and addressing the storage and transport issues through innovative materials and designs based on nano- and bio-technology remains an active area of research.

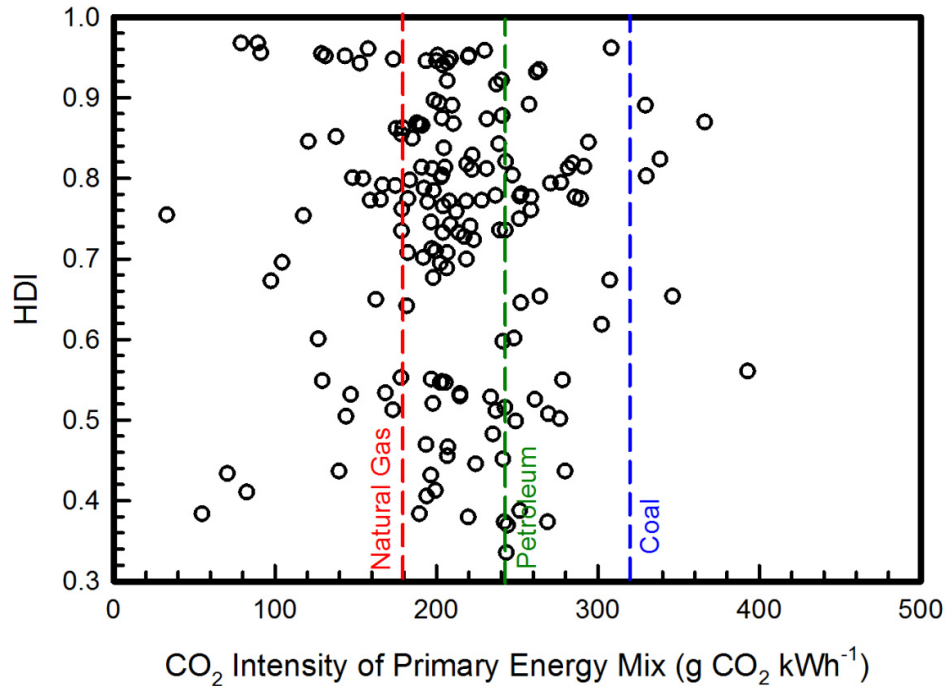


Figure 2-11: HDI as a function of CO₂ intensity for 170 nations showing no correlation.

2.7 Efficiency in the United States

Facing large future energy needs in the developing world, it is also important to focus on today. In the United States, the major consumers of primary energy are the transportation sector (29%; 27,811 kWh year⁻¹ person⁻¹), residential buildings (21%; 20,777 kWh year⁻¹ person⁻¹) and commercial buildings (18%; 17,612 kWh year⁻¹ capita⁻¹). Of transportation, approximately 63% is consumed by gasoline vehicles (18% of the

total; 17,607 kWh year⁻¹ capita⁻¹). Based on population densities and average automobile fuel economies in Europe compared to the United States, the reduction in consumption if European practices were adopted in the United States can be estimated using the following equation:

$$\eta_e = \frac{\sqrt{\frac{\rho_{USA}}{\rho_{Europe}}}}{\left(\frac{MPG_{Europe}}{MPG_{US}}\right)} = 0.24 \quad (2-9)$$

Where ρ_{US} is the average population density in the US (1,100 people km⁻²), ρ_{Europe} is the population density in Europe (7,700 people km⁻²), MPG_{US} is the average fuel economy in the US (25 miles gallon⁻¹) and MPG_{Europe} is the average fuel economy in Europe (40 miles gallon⁻¹). Thus it is estimated that the consumption of the gasoline-powered transportation sector (17,607 kWh year⁻¹ capita⁻¹) could be reduced to 4,226 kWh year⁻¹ capita⁻¹ by following European or Japanese urban design and automobile fuel economy standards.

There is much work to do in the United States on constructing more energy efficient buildings. By addressing heating and cooling, which constitute a large fraction of a building's energy use (Figure 2-12), preliminary studies suggest that using different design practices and standards could reduce the energy consumption of buildings in the US to 50% of the baseline^{17, 18}. It is estimated that building energy consumption can be reduced by 50%, reducing residential energy consumption to 10,389 kWh year⁻¹ capita⁻¹ and commercial consumption to 8,807 kWh year⁻¹ capita⁻¹. However, the financial cost of this is unclear. Efficiency gains in buildings and the transportation sector together could reduce US per capita primary energy consumption to 64,457 kWh year⁻¹ capita⁻¹,

approaching the saturation value. All of the technology and design practices are available; it is primarily a question of time, cost and political will.

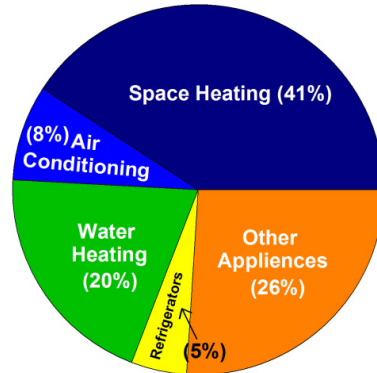


Figure 2-12: Total consumption of household energy for different end uses averaged over the United States.

2.8 Conclusions

Human development increases with primary energy consumption. There is an energy consumption level after which only small gains in development are achieved for additional primary energy consumption, called the saturation energy. Efficiency gains made by reducing consumption of energy-rich nations to the saturation energy are not enough to make up for the ever-growing needs of the developing world. Carbon Capture and Storage programs for fossil fuels along with nuclear fission and low-cost solar must be implemented on a global scale to address climate change. Efficiency programs in energy-rich developed nations should be implemented immediately; to bridge the time gap while comprehensive solutions for the developing world are formulated.

2.9 Acknowledgements:

We would like to acknowledge partial support from Corning Incorporated, DOD-MURI Grant UR523873 and the Center for Materials Innovation at Washington University in Saint Louis. We would also like to thank the McDonnell Global Energy and Environment Partnership (MAGEEP) for providing a forum in which many of these ideas developed. Elijah Thimsen would like to thank Jessica Deem for many discussions about the content while preparing this manuscript.

2.10 References:

1. Cabrera, S.; Jaffe, K., On the energetic cost of human societies: Energy consumption as an econometric index. *Interciencia* **1998**, 23, (6), 350-+.
2. *Energizing the Millennium Development Goals: A Guide to Energy's Role in Reducing Poverty*; United Nations Development Program: 2005.
3. Zakaria, F., *The post-American world*. 1st ed.; W.W. Norton & Co.: New York, 2008; p 292 p.
4. *World Urban Areas and Population Projections: 5th Comprehensive Edition*; Demographia: 2009.
5. An, F.; Gordon, D.; He, H.; Kodjak, D.; Rutherford, D. *Passenger Vehicle Greenhouse Gas and Fuel Economy Standards: A Global Update*; The International Council on Clean Transportation: 2007.
6. *Human Development Report 1990*; United Nations Development Program: 1990.
7. *Human Development Report 2007/2008*; United Nations Development Program: 2007.

8. Dias, R. A.; Mattos, C. R.; Balestieri, J. A. P., The limits of human development and the use of energy and natural resources. *Energy Policy* **2006**, 34, (9), 1026-1031.
9. Pasternak, A. *Global Energy Futures and Human Development: A Framework for Analysis*. United States Department of Energy Report UCRL-ID-140773; Lawrence Livermore National Laboratory, Livermore CA: 2000.
10. Martinez, D. M.; Ebenhack, B. W., Understanding the role of energy consumption in human development through the use of saturation phenomena. *Energy Policy* **2008**, 36, (4), 1430-1435.
11. United States DOE Energy Information Agency Country Profile Data Base (<http://tonto.eia.doe.gov/country/index.cfm>).
12. United States Census Bureau International Data Base (IDB) (<http://www.census.gov/ipc/www/idb/>).
13. *Emissions of Greenhouse Gases in the United States*. Report DOE/EIA-0573(99); U.S. Department of Energy: 1999.
14. Farrell, A. E.; Plevin, R. J.; Turner, B. T.; Jones, A. D.; O'Hare, M.; Kammen, D. M., Ethanol can contribute to energy and environmental goals. *Science* **2006**, 311, (5760), 506-508.
15. Lewis, N. S., Powering the planet. *Mrs Bulletin* **2007**, 32, (10), 808-820.
16. Turner, J. A., A realizable renewable energy future. *Science* **1999**, 285, (5428), 687-689.
17. Koch, D. C.; Kutch, J.; Hutzler, W. J.; Holt, E., Comparing Swiss and U.S. Homes in the Area of Energy Efficiency. In *IAJC-IJME International Conference*, Nashville, Tennessee, 2008.

18. Norberg-Bohm, V.; White, C. *Building America Program Evaluation: Volume 1 Main Report*; Report for Belfer Center for Science and International Affairs: 2004.

Chapter 3:

Synthesis of Nanostructured Photoactive Films with Controlled Morphology by a Flame Aerosol Reactor

The results presented here were published in:

Nanostructured photoactive films synthesized by a flame aerosol reactor, Elijah Thimsen and Pratim Biswas, *American Institute of Chemical Engineers Journal* **2007**, 53, (7), 1727-1735.

3.1 Abstract

A flame aerosol reactor (FLAR) system was used to deposit nanostructured photoactive films of titanium dioxide with well controlled morphologies. Nanoparticles were generated in the aerosol phase and then deposited onto a water-cooled substrate via thermophoresis. Two important parameters that influenced film characteristics were the titanium precursor feed rate and substrate temperature, through their effect on particle sintering dynamics on the substrate. The size of the particles as they arrived at the substrate was controlled by varying the titanium precursor feed rate. When the size was below approximately 8 nm, sintering was completed in the time available to obtain films with columnar nano-structures. Larger particle sizes resulted in granular, particulate films. The temperature of the substrate was also an important parameter as it controlled the sintering rate and the resultant crystal phase of the film. The thickness of the films was controlled by varying the precursor feed rate and deposition time. The performance of the as-synthesized photocatalytic films was established by measuring the resultant photocurrents. Well-sintered columnar morphologies and thicker films (in the range of 40 to 900 nm) resulted in the largest photocurrents.

3.2 Introduction

Coatings are applied as films to surfaces for a variety of different applications, such as to form a protective layer to prevent corrosion, to enhance appearance of the base material, for electronics applications, in magnetic media, and in engineered reactors for catalytic applications. The chemical and physical characteristics of the film, such as composition, thickness, and morphology, have to be controlled for specific applications. For example, continuous, non-porous, ceramic films were used to provide corrosion protection to steel surfaces¹. In contrast, nano-porous, open morphology films were used in photochemical reactors for synthesis of partial-oxygenates by environmentally benign routes². Nanostructured films allow the possibility of obtaining high surface area coatings with tailored characteristics suitable for applications in catalytic reactors³.

Titanium dioxide is a wide band-gap semiconducting, ceramic oxide that has been used as a coating material in several different applications for air and water purification, for sulfur removal⁴, for toxic metals capture^{5, 6}, destruction of bacteria and viruses, self cleaning building materials, and superhydrophilic fog free films⁷. It is the most widely used photocatalyst because it is relatively safe, inexpensive and stable to photocorrosion. Another exciting application is the production of hydrogen by a photosplitting reaction of water, which could provide an environmentally benign and sustainable source of hydrogen fuel for the energy industry⁸. Photosplitting of water and many other solar-energy applications of TiO₂ require that the semiconductor be immobilized as a film. The morphology of the film is an important parameter in establishing the overall effectiveness; for example, a high surface area is desirable if localized chemical reactions are to be promoted, while low internal resistance to mobility of photogenerated charge carriers is also important if these are to be extracted and transported through an external

circuit⁸⁻¹⁰. Several studies have identified relationships between film characteristics such as: thickness, morphology and feature size, and the resulting photocatalytic performance^{2, 11-14}. Film characteristics are primarily determined by the synthesis technique.

There are many synthesis processes used for the deposition of titanium dioxide films. Many of the existing techniques are multi step and require long synthesis times to produce high performance films with desirable morphologies, making them unattractive for industrial scale up. Typical film synthesis processes consist of a deposition step followed by an annealing step. The entire multi step process can take from several hours to a day to complete. Limmer et. al.¹⁵ describe a 3 to 6 hour electrophoretic sol-gel process to synthesize TiO₂ nanorods on alumina and polycarbonate substrates for high surface-area applications. For dye sensitized solar cells, dip-coating-annealing processes have been described to synthesize films in 2 hours; but the resultant granular films have limited photoactivity due to electron-hole migration barriers at particle-particle interfaces¹⁶. For photosplitting of water, Varghese et al.¹² describe a 2-step, 17 to 24 hour Ti-foil anodization process to produce TiO₂ nanotubes with controlled thickness; which is used to increase the light to hydrogen conversion efficiency by creating thicker films. To better understand and optimize film performance for important applications like photocatalytic hydrogen production, it is essential to have robust methods to synthesize films with well controlled characteristics.

Flame aerosol reactors, which have been an industrially successful route to synthesize nanomaterials, provide a single step process for deposition of nanostructured films¹. Madler et. al.³ have used FLAR systems for depositing highly porous films

relying on thermophoretic deposition. Palgrave and Parkin¹⁷ have described systems using nanoparticle precursors for the synthesis of nanocomposite thin films. Detailed deposition models have also been developed to predict both the film morphology and other characteristics¹⁸⁻²⁰. Some studies have demonstrated control over film characteristics through the application of external forces such as electrical fields²¹. However, due to the complex interactions of different process parameters such as precursor concentration, time-temperature history in the flame, deposition rate, time-temperature history on the substrate and many others, there are few studies that relate process conditions to resultant film parameters obtained from single-step flame aerosol reactors. Specifically, conditions that result in characteristics that are important to photocatalytic applications, such as hydrogen production have not been studied in detail. A more systematic demonstration is essential if practical applications are to be realized.

In this paper, a flame aerosol reactor (FLAR) to deposit nanostructured films of titanium dioxide with controlled morphology and thickness is described. An understanding of the various process parameters that affect film growth, such as precursor feed rate and deposition time, is established. The crystal phase and grain size of the film are established as a function of the process parameters. The resultant photocurrents generated in the films upon exposure to UV irradiation, which is a measure of photoelectric film properties that are important to photocatalytic hydrogen production efficiency, is determined and related to film characteristics.

3.3 Experimental Methods

3.3.1 System

The experimental unit consisted of a precursor feed system, a flame aerosol reactor (FLAR) and a temperature controlled deposition substrate (Figure 3-1). The precursor feed system consisted of a bubbler containing titanium tetra-isopropoxide (TTIP, Aldrich: 205273, 97% purity) through which argon (Grade 4.8) was bubbled at varying flow rates. The temperature of the bubbler was maintained at 30 °C. To prevent condensation of the TTIP, the lines leading up to the flame reactor were heated to approximately 50°C. The TTIP feed rate was calculated based on the saturation pressure and assumed proportional to the argon flow rate through the bubbler²². An additional argon line was added so the total argon flow rate could be held constant at 2.0 lpm (liters per minute at STP) while varying the flow through the bubbler. The FLAR was a premixed methane – oxygen burner made of a 3/8 “ O.D. stainless steel tube with three 1/8” cylinders packed into the middle to achieve an optimal outlet velocity (450 cm/s) through a 0.16 cm² area which prevented flame blow off and extinction. The methane flow rate was fixed at 0.5 lpm (liters per minute at STP) and the oxygen flow rate was fixed at 1.5 lpm, above the stoichiometric value of 1.0 lpm for complete combustion. The additional oxygen was provided to ensure complete oxidation of TTIP to produce stoichiometric TiO₂. All gas flow rates were controlled by digital mass flow controllers (MKS Instruments, Wilmington MA), and the four gas streams were combined and sent through the burner to the flame region (Figure 3-1).

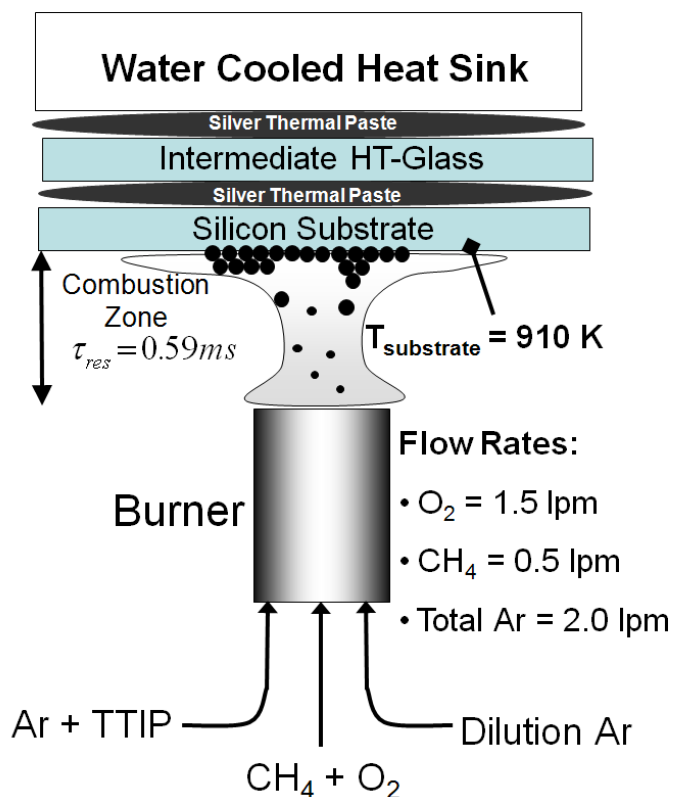


Figure 3-1: Schematic diagram of the experimental setup for deposition of nanostructured TiO₂ films.

The flame temperature distribution was measured using a type R thermocouple (Pt-Rh:Pt 2mm bead) and corrected for radiation from the thermocouple bead. The average flame temperature was $2200 K \pm 100 K$. A temperature controlled substrate was used wherein the titanium dioxide particles formed in the flame were deposited. The substrate used was a square piece of optically polished silicon, 1.5 cm on a side. The silicon substrate was attached to a water-cooled substrate holder to control the temperature of the substrate and the resultant crystal phase of the film (anatase versus rutile). Intimate thermal contact was established between the substrate and heat sink by applying a small amount of silver thermal paste (Arctic Silver, Visalia CA).

The substrate temperature was controlled by tailoring the thermal resistance of the interface between the substrate and heat sink. If the silicon substrate was pasted directly to the heat sink, the temperature was approximately 700 K, as measured by a small-bead type K thermocouple cemented to the substrate surface. The thermal resistance of the substrate to heat-sink interface was increased by inserting an intermediate piece of high-temperature glass (Ace-Glass, Vineland NJ). Under these conditions, the resulting temperature of the substrate was 910 K. An even higher temperature was achieved by inserting a second piece of glass which increased the substrate temperature to approximately 1080 K. However, unless otherwise stated, only one intermediate piece of glass was used and particles were deposited at a substrate temperature of 910 K. The substrate temperature is important to control because it alters the morphology of the particle-deposit by altering the sintering rates as discussed in detail in the Results section.

3.3.2 Characterization

Particles in the aerosol phase in the flame region (in the absence of the deposition substrate) were characterized by transmission electron microscopy (TEM) and online scanning mobility particle spectrometry (SMPS) measurements. The particle size distribution was obtained from TEM (JEOL 1200 120 kV) and SMPS (Platform 3080, Nano-DMA 3085, TSI Corp., Shoreview MN) measurements. It should be noted that the TEM and SMPS measured two different particle size distributions. From TEM images, the primary particle size distribution was obtained, which is the important quantity for dynamic processes such as sintering. The SMPS measured the mobility equivalent aerosol size distribution. The mean size measured by the SMPS could be

larger than the primary particle size, especially if agglomeration is prevalent in the system^{23, 24}.

After deposition, the TiO₂ films were characterized by scanning electron microscopy (SEM) and x-ray diffraction (XRD). The as-produced films were viewed in an SEM (Hitachi model S-4500 field emission electron microscope operating at 15 kV) to determine the film thickness and morphology. For thickness measurements the silicon substrates were cleaved down the middle of the film and attached vertically to the SEM specimen mount. The films were then imaged along a line of sight parallel to the substrate surface to obtain side view images. The crystalline phase and grain size of the films were determined using a Rigaku DMax x-ray diffractometer.

Finally, the photoelectric properties of the films were characterized by photocurrent measurements. The films were deposited onto electrically insulating high-temperature glass substrates (Borosilicate, ACE Glass, Vineland NJ) at a slightly elevated temperature of 1000 K. Under UV irradiation from a 100 watt 360 nm lamp (Blak-Ray, Model B-100A), the photocurrent was measured by applying a voltage of 22V to two silver electrodes (SPI supplies, West Chester PA) that were painted 1 cm apart on the film surface. The current between the electrodes was measured using a picoammeter (Keithly Instruments, Cleveland OH).

3.3.3 Test Plan

Two independent process parameters that affect film characteristics are the TTIP feed rate and deposition time. These parameters were independently varied to determine the effects on the aerosol phase particle size distributions, film grain size, growth rate,

film thickness, crystalline phase, and photocurrent. A summary of the experimental parameters and results is presented in Table 3-1.

Table 3-1: Summary of experimental parameters and results. Constants: methane flow rate = 0.5 lpm; oxygen flow = 1.5 lpm; total argon flow = 2.0 lpm; deposition height = 2 cm above burner; TTIP bubbler temp = 30°C. The column “Photocurrent” corresponds to current measured at 22 V applied voltage.

Exp.	Experimental Conditions		Aerosol phase Measurements		Film Measurements				
	Deposition Time (sec)	TTIP Feed Rate (mmol/hr)	Average D_p from TEM (nm)	Average D_p from SMPS (nm)	Film Thickness from SEM (nm)	Crystalline Phase from XRD	Grain Size From XRD (nm)	Average Growth Rate (nm/sec)	Photo-Current (nA)
1	90	0.27	-	10.8	180	-	-	2.00	-
2	180	0.069	4.5	4.3	79	Anatase	47.3	0.44	46.86
3	180	0.14	-	7.2	213	Anatase	49.1	1.18	22.10
4	180	0.27	-	10.8	322	Anatase	40.7	1.79	0.64
5	180	0.55	8.0	13.1	2010	Anatase	9.0	11.17	2.53
6	360	0.069	4.5	4.3	233	-	-	0.65	-
7	360	0.27	-	10.8	730	-	-	2.03	-
8	60	0.14	-	7.2	42	Anatase	-	0.70	-
9	90	0.14	-	-	64	Anatase	-	-	2.6
10	120	0.14	-	7.2	86	Anatase	-	0.72	-
11	240	0.14	-	7.2	204	Anatase	-	0.85	-
12	360	0.14	-	-	311	Anatase	-	-	1200
13	480	0.14	-	7.2	417	Anatase	-	0.87	-
14	760	0.14	-	-	692	Anatase	-	-	15000
15	960	0.14	-	7.2	889	Anatase	-	0.93	-

3.4 Results and Discussion

The gas phase precursor was rapidly oxidized in the high temperature environment to form nanoparticles. These nanoparticles were then directed by thermophoretic forces from the hot gas to the water-cooled substrate and deposited to form a film. There are two important process steps that influence the final film characteristics. The first is formation of TiO_2 particles by oxidation of the TTIP in the high temperature flame environment. The second is restructuring of the particles once

they have been deposited onto the substrate via thermophoresis. The influence of these two steps on the final film characteristics is presented in the following sections.

3.4.1 Aerosol Phase Dynamics

The timescales for different process occurring in the aerosol phase, such as chemical reaction of the precursor and aerosol dynamics, can affect the final film morphology as illustrated in Figure 3-2. If the characteristic time for the reaction of the TTIP precursor (τ_{rxn}) is larger than the residence time, a chemical vapor deposition (CVD) process would be expected²⁵. This would result in TTIP molecules being transported to the substrate and react therein to form the titanium dioxide film. Alternatively, if the characteristic reaction time is less than the residence time, the precursor will react to form particles. Other important time scales in the aerosol phase are the particle-particle characteristic collision time⁶ (τ_{coll}) and the particle sintering time²⁶ (τ_{sin}). Depending on different combinations as illustrated in Figure 3-2, the deposition process would either be individual particle deposition (IPD) or agglomerated particle deposition (APD).

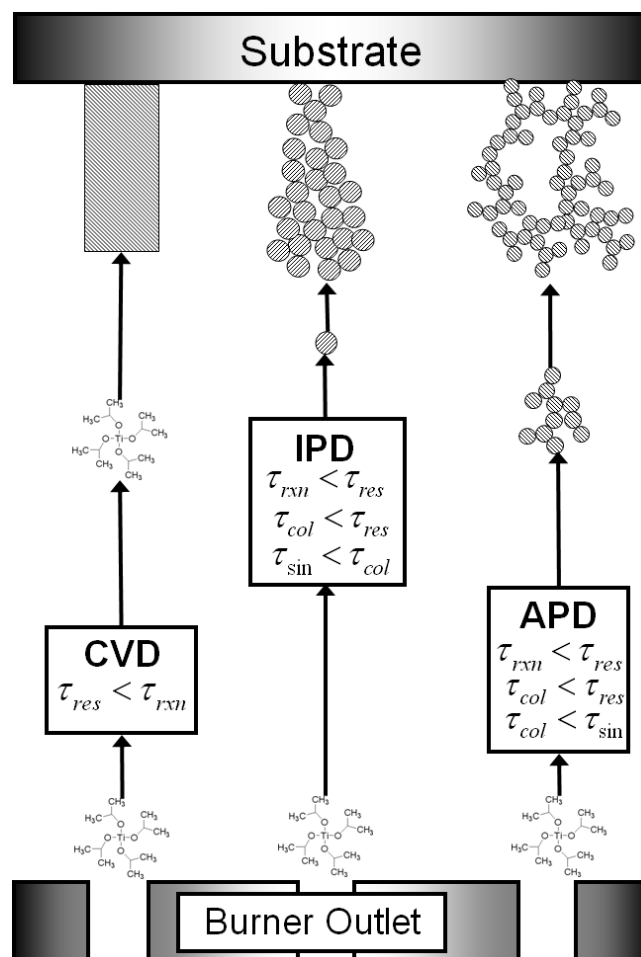


Figure 3-2: Characteristic time conditions for different film deposition processes: chemical vapor deposition (CVD) individual particle deposition (IPD) and aggregate particle deposition (APD).

To determine which deposition process was dominant, the various aerosol phase characteristic times were estimated (Table 3-2). The residence time in the flame was estimated by assuming that the flame cross-section was equal to the burner outlet area (no jet expansion or ambient fluid entrainment), gases immediately reached the flame temperature and the path-length was equal to the burner-substrate distance of 2 cm. Using these assumptions, a residence time (τ_{res}) of 0.59 ms was calculated. The calculated characteristic reaction time of the TTIP thermal decomposition was 0.12 ms, which was less than the residence time, meaning the TTIP rapidly reacts to form TiO_2

particles in the flame. The characteristic particle-particle collision time assuming 5 nm particles and a TiO₂ molecular concentration calculated from the TTIP feed rate ($\sim 10^{15} \text{ cm}^{-3}$) was ~ 0.1 ms, while the sintering time for the 5 nm particles was 7.4×10^{-5} ms, implying that particles are present as individual spheroids in the flame. Under the flame conditions used in this study, IPD was the dominant process for deposition. Later, the dynamics in the particle-deposit that result in specific morphologies of the film and the relationship of those morphologies to photocurrent generation will be illustrated.

Table 3-2: Summary of estimated characteristic times encountered in the aerosol phase.

Characteristic Time	Symbol	Value	Reference
Residence Time in Flame	τ_{res}	0.59 ms	This Work
Thermal Decomposition Reaction of TTIP to form TiO ₂	τ_{rxn}	0.12 ms	Wu and Biswas ⁶
5 nm Particle-Particle Collisions	τ_{col}	~ 0.1 ms	Wu and Biswas ⁶
5 nm Particle Sintering at 2200 K	τ_{sin}	7.4×10^{-5} ms	Kobata et al. ²⁶

The effect of TTIP feed rate on the particle size distribution is illustrated in Figure 3-3. The aerosol size distribution was measured online with the SMPS. The primary particle size distribution was measured from TEM images by measuring the diameters of approximately 130 particles. A log-normal curve fit was performed using Origin (Microcal, v 4.1) to determine distribution parameters. The particle size increased from a mean of 4.5 nm at a TTIP feed rate of 0.069 mmol/hr (Test 2) to 8.0 nm at a TTIP feed rate of 0.55 mmol/hr (Test 5), as measured by TEM. For the lower TTIP feed rate the SMPS measurement agreed well with the TEM. However, at the higher TTIP feed rate, the SMPS measured a larger diameter than the one obtained from TEM. The discrepancy between the particle size measured from TEM and SMPS at the higher feed rate was likely due to biases that resulted from agglomeration in the dilution probe during

sampling. Despite this small discrepancy, the measurements clearly illustrated the trend of increasing particle size with increasing TTIP feed rate.

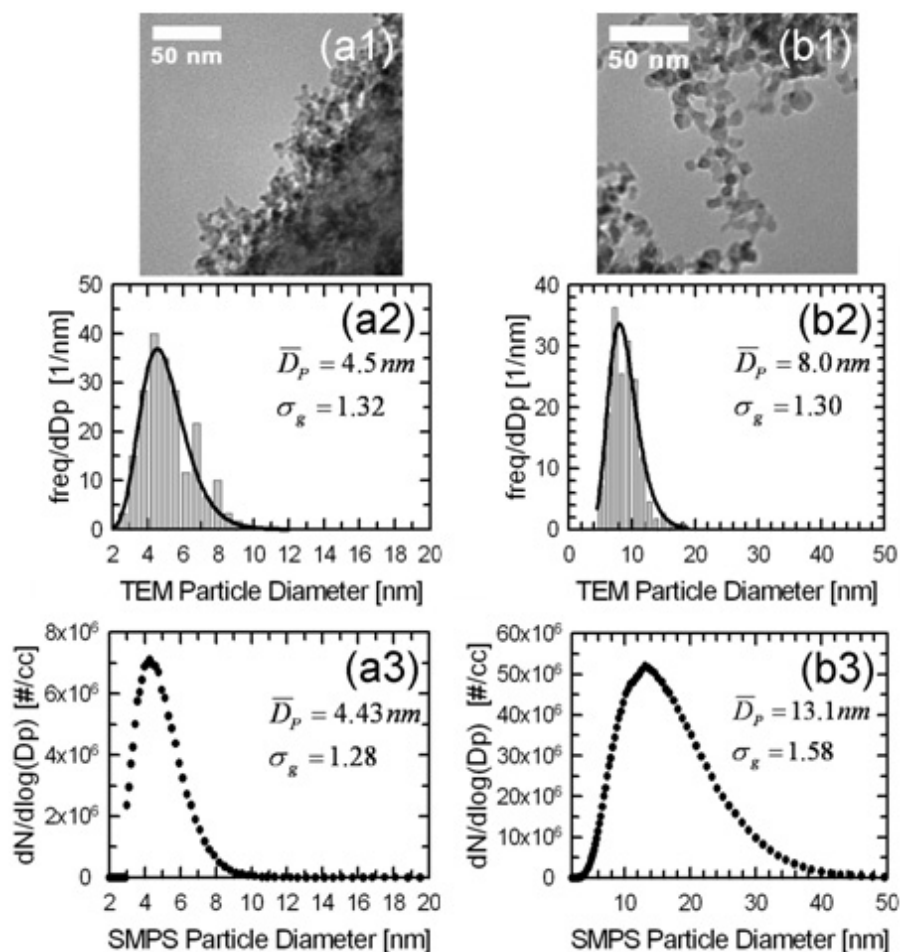


Figure 3-3: Size measurements of particles in the aerosol phase for two TTIP feed rates. (a) For TTIP = 0.069 mmol/hr and (b) for TTIP = 0.55 mmol/hr. (1) TEM image of particles; (2) particle size distribution from TEM images; and (3) aerosol size distribution measured from the SMPS.

The increase in particle size as a function of TTIP feed rate was due to enhanced coagulative growth in the flame region. At the flame temperature, the reaction to form TiO₂ molecules from TTIP was fast ($\tau_{rxn} = 0.12$ ms, Table 3-2). Once formed, the TiO₂ molecules collided to form particles that subsequently grew through a coagulative growth process²⁷. The sintering time ($\tau_{sin} = 7.4 \times 10^{-5}$ ms, Table 3-2) was much smaller

than the collision time ($\tau_{coll} \sim 0.1$ ms, Table 3-2) under these conditions, ensuring that near spherical particles resulted from the aerosol phase particle growth process. For a constant residence time, the final size of the coagulation growth process scaled with the initial concentration of TiO_2 molecules, or TTIP feed rate. Through the TTIP feed rate, the size of particles as they arrived at the substrate was tuned to control the restructuring dynamics on the substrate, which is discussed in the following section.

3.4.2 Dynamics After Particle Deposition onto the Substrate

Through its influence on the particle arrival size, which changed the film restructuring dynamics, the TTIP feed rate affected the final film grain size and morphology. The influence of particle arrival size on the film restructuring dynamics can be explained by particle sintering on the substrate. Sintering results in two small particles combining to form a larger structure with a volume equal to the sum of the two initial volumes. At constant temperature, the characteristic time for two TiO_2 particles of the same initial size to completely sinter is proportional to particle diameter to the fourth power^{26,28}. From 3-3, the arrival size of particles at the substrate was approximately 4.5 nm and 8.0 nm for TTIP feed rates of 0.069 mmol/hr (Test 2) and 0.55 mmol/hr (Test 5) respectively. The characteristic sintering time for the higher TTIP feed rate was an order of magnitude longer than for the lower TTIP feed rate, thus changing the sintering dynamics and final film morphology. This difference in morphology can be seen in Figure 3-4.

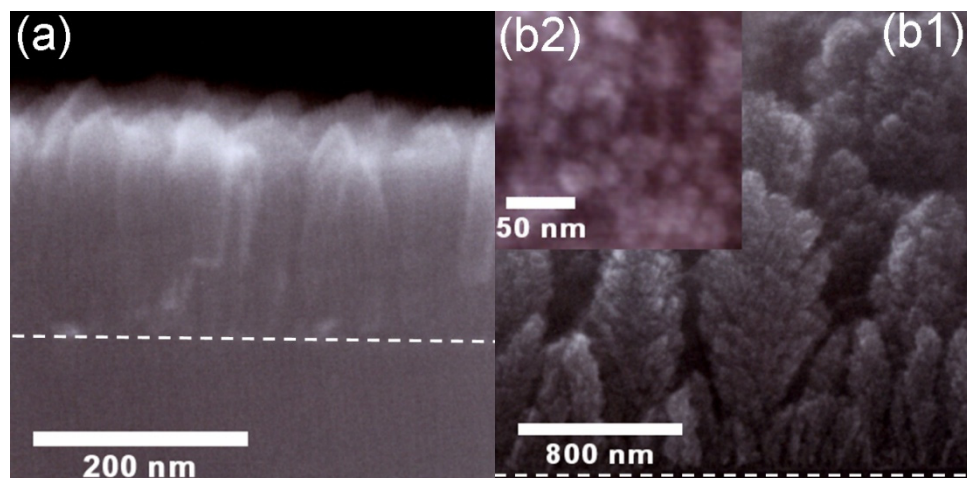


Figure 3-4: Film morphology for two TTIP feed rate for films deposited for a fixed time of 180 seconds. (a) High magnification side view SEM image for TTIP = 0.14 mmol/hr. (b) For TTIP = 0.55 mmol/hr, (b1) low and (b2) high magnification side view SEM images.

For small particle arrival size, or fast sintering dynamics, a columnar structure was observed. The sintered columnar morphology was characterized by continuous vertical columns, observed in the SEM, and large average grain size, measured from XRD peak broadening using the Scherrer equation. As small particles, which were 4.5 nm in the aerosol phase, sintered, they combined to form larger structures that had longer range crystalline order, hence the 47 nm grain size observed in the XRD (Test 2).

Alternatively, for large particle arrival size, or slow sintering dynamics, a granular particulate morphology was observed. The particulate morphology was characterized by fractal structures, observed in the SEM and a small average grain size. Due to the slow sintering dynamics, the large particles did not combine and instead remained isolated with approximately the same grain size as was present in the original particle before it deposited. This can be seen by comparing the average grain size of the unsintered film deposited at 0.55 mmol/hr TTIP feed rate (Figure 3-5) to the aerosol phase particle size

from TEM at the same conditions (Figure 3-3). Due to the 2200 K flame temperature, the particles in the aerosol phase were expected to be nearly single crystal. From the TEM measurements, the large particles were approximately 8 nm before they deposited onto the substrate, which is similar to the 9 nm grain size of the film, which would be expected if the particles did not experience significant sintering once deposited onto the substrate.

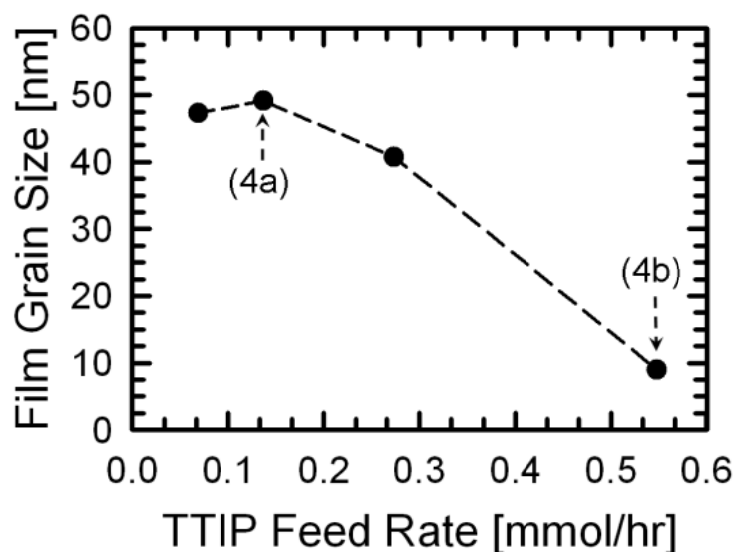


Figure 3-5: Average grain size measured from XRD peak broadening as a function of TTIP feed rate, for a fixed deposition time of 180 seconds. The points labeled as 4a and 4b correspond to the same films as the SEM images in Figure 3-4.

The temperature of the substrate (film) also affects the sintering rate^{26,28}. Temperature could also be used as a process parameter to control the morphology of the film. This was verified qualitatively by changing the substrate to heat sink thermal resistance, to alter the substrate temperature. At low temperatures, particulate films were observed in the SEM, due to low rates of sintering amongst the deposited particles. At higher substrate temperatures, well-sintered columnar films were obtained that were similar in appearance to the sintered columnar SEM images (Figure 3-4a). However, if

one increases the temperature further, the films will anneal and the columnar structures are expected to collapse as predicted by the models developed by Kulkarni and Biswas²⁰. Furthermore, undesirable crystal phase transitions from anatase to rutile will take place at elevated temperatures, which precludes increasing the substrate temperature substantially beyond 600 °C.

The film thickness can be controlled by both the deposition time and TTIP feed rate. Films were deposited for different times and imaged by SEM to measure thickness. In Figure 3-6, selected side view SEM images are shown that illustrate the evolution of film thickness for several deposition times. For the times tested, the film thickness increased roughly linearly with deposition time (Figure 3-7). In addition, the growth rate increased with TTIP feed rate which was reasonable considering the increased mass flux to the substrate.

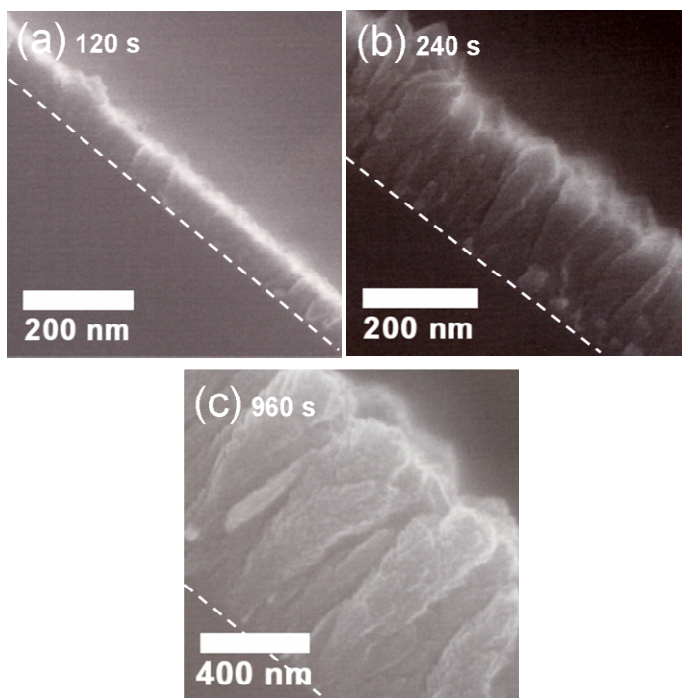


Figure 3-6: Selected side view SEM images of films showing film thickness increasing with deposition time for a fixed TTIP feed rate of 0.14 mmol / hr: (a) 120 seconds, (b) 240 seconds and (c) 960 seconds.

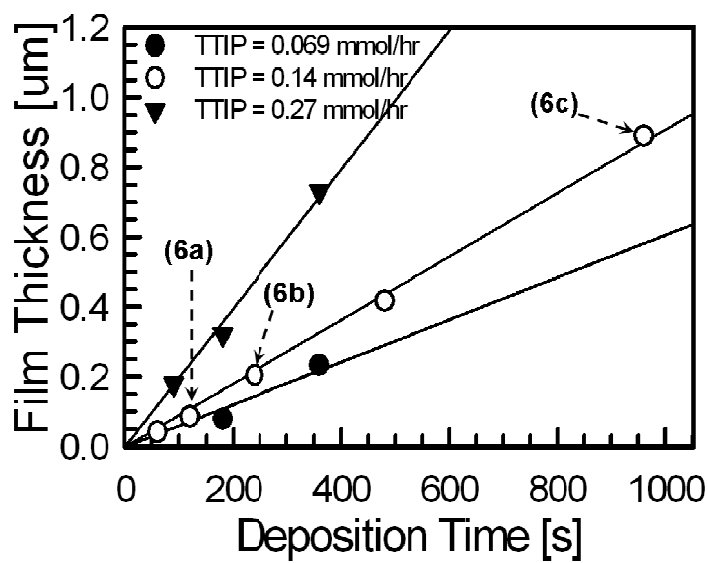


Figure 3-7: Film thickness plotted as a function of deposition time for 3 different TTIP feed rates. The points labeled as 6a, 6b and 6c correspond to the SEM images in Figure 3-6.

3.4.3 Photocurrent Measurements

With precise control over both the film morphology and thickness, photocurrent measurements were performed to understand the relationship between film characteristics and photoactivity. A simple electrical circuit was created by connecting lead wires to the film and a DC power supply. A voltage of 22V was applied and the resulting current was measured using a picoammeter. Photocurrent measurements were taken for films deposited at several TTIP feed rates and deposition times (Figure 3-8). The photocurrent was at the noise level of the picoammeter when the UV lamp was switched off.

Morphology had a significant effect on the photocurrent. The films deposited at lower TTIP feed rates exhibited greater photocurrents than the films formed with higher TTIP feed rates. At lower TTIP feed rates, the films had a sintered columnar like structure with a large grain size. At higher TTIP feed rates, the films had a particulate

like structure with a small average grain size. The photocurrent is related to grain size, but also depends on interfacial properties and can change for slight alterations of the film morphology. For instance, it is more difficult for free charge carriers to migrate to the electrodes in particulate films with small grain size because of particle-particle interfacial migration barriers¹⁶. In continuous and well-sintered films with larger grain size, free charge carriers encounter fewer migration barriers and can freely flow to the electrodes. This result is in agreement with other work that has found a higher electron drift mobility in columnar films, compared to granular particulate films²⁹.

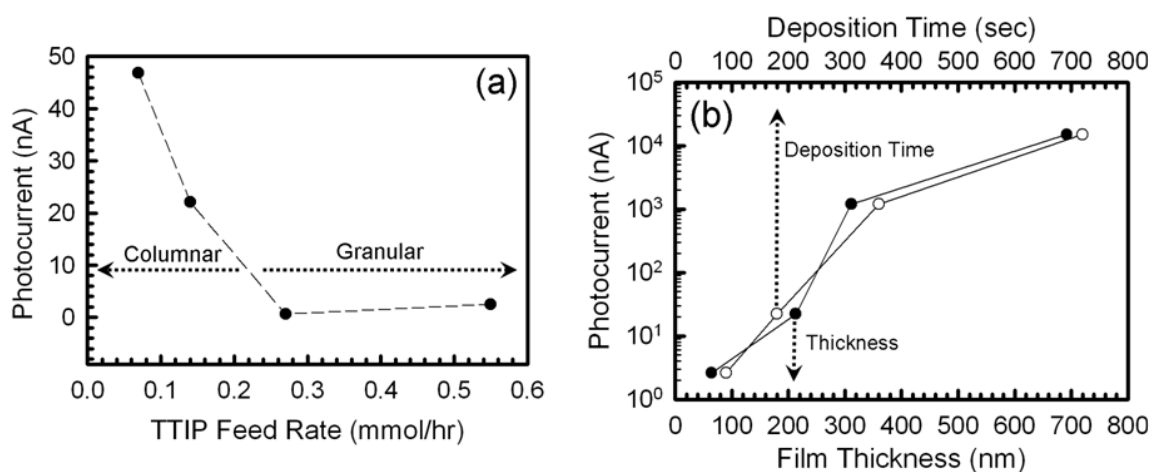


Figure 3-8: Measured photocurrents as a function of: (a) TTIP feed rate for a fixed deposition time of 180 sec. and (b) deposition time (film thickness) for a fixed TTIP feed rate of 0.14 mmol / hr.

The photocurrent was larger for the thicker films (longer deposition times), while maintaining the well-sintered, columnar morphology. As the thickness of the sintered columnar film was increased, it intercepted more light, thus generating an increased number of free charge carriers. The increased number of free charge carriers resulted in an increase in the measured photocurrent. It should be noted that there may be an upper limit on thickness beyond which the photocurrent could saturate due to no further

increase in light absorption (due to geometrical effects) . These photocurrent measurements illustrate that the deposited films are photoactive and there are clear trends in the photoactivity as a function of controllable film characteristics.

3.5 Conclusions

A robust system consisting of a flame aerosol reactor (FLAR) for the deposition of TiO₂ films has been developed. The ability to synthesize films with well-controlled morphology in a single-step process was described. Two important process parameters that influence the film morphology are TTIP feed rate and the substrate temperature. These parameters influence the final film morphology through their effect on particle sintering dynamics on the substrate. The range of particle arrival sizes was varied from 4.5 nm to 8.0 nm. Smaller particle arrival sizes ensure faster sintering after deposition resulting in the formation of well-sintered, columnar morphology films. For larger particle sizes, the sintering on the substrate is much slower, leading to a granular morphology. Good control of the film thickness was demonstrated, and the relationship to deposition time and precursor feed rate established.

The titanium dioxide films were demonstrated to be activated by light. The resultant photocurrents were measured and the performance of the well-sintered, columnar morphology films was found to be superior to the granular films. Similarly, thicker films in the range of 42 to 890 nm were demonstrated to have higher photocurrents. These photocurrent results are a measure of the photoelectric properties of the films, which are likely critical to applications such as photocatalytic hydrogen

production by watersplitting. Work is currently underway to apply these films to photocatalytic watersplitting.

The FLAR could likely be scaled up and applied to the deposition of many metal-oxide films for which suitable precursors are available. Fe₂O₃ films have been synthesized by switching the precursor in the bubbler from TTIP to Fe(CO)₅, and is the subject of a future paper.

This study provides insights into design parameters and operating conditions necessary to obtain desired film morphologies. For example, if well-sintered columnar films are desired, the particle arrival size and the substrate temperature would have to be within a certain range. The particle arrival size is controlled by the flame operating conditions and feed rate of the precursor. The results indicate that beyond a certain feed rate, the resultant particle size would be large so that well-sintered columnar morphologies would not be obtained.

3.6 Acknowledgements

We acknowledge partial support from the Center for Environmentally Beneficial Catalysis (CEBC) National Science Foundation Engineering Research Center Grant (ERC-0310689), the NSF- NIRT 0304649 Grant, and the Center for Materials Innovation (CMI) at Washington University in Saint Louis.

3.7 References

1. Yang, G.; Biswas, P.; Boolchand, P.; Sabata, A., Deposition of Multifunctional Titania Films by Aerosol Routes. *J. Am. Ceramic Soc.* **1999**, 82, (10), 2573-2579.

2. Sahle-Demessie, E.; Gonzalez, M.; Wang, M. Z.; Biswas, P., Synthesizing Alcohols and Ketones by Photoinduced Catalytic Partial Oxidation of Hydrocarbons in Titania Film Reactors Prepared by Three Different Methods. *Ind. Engr. Chem. Res.* **1999**, *38*, 3276-3284.
3. Madler, A. L.; Roessler, A.; Pratsinis, S. E., Direct Formation of Highly Porous Gas-Sensing Films by in-situ Thermophoretic Deposition of Flame-Made Pt/SnO₂ Nanoparticles. *Sensors and Actuators B-Chemical* **2006**, *114*, (1), 283-295.
4. Beck, D. D.; Siegel, R. W., The Dissociative Adsorption of Hydrogen-Sulfide over Nanophase Titanium-Dioxide. *Journal of Materials Research* **1992**, *7*, (10), 2840-2845.
5. Wu, C. Y.; Lee, T. G.; Tyree, G.; Arar, E.; Biswas, P., Capture of mercury in combustion systems by in situ-generated titania particles with UV irradiation. *Environmental Engineering Science* **1998**, *15*, (2), 137-148.
6. Biswas, P.; Wu, C. Y., Control of toxic metal emissions from combustors using sorbents: A review. *Journal of the Air & Waste Management Association* **1998**, *48*, (2), 113-127.
7. Fujishima, A.; Hashimoto, K.; Watanabe, T., *TiO₂ Photocatalysis, Fundamentals and Applications*. BKC inc., Japan: 1999.
8. Herrmann, J. M., Heterogeneous Photocatalysis: State of the Art and Present Applications. *Topics in Catalysis* **2005**, *34*, (1-4), 49-65.
9. Gratzel, M., Photoelectrochemical Cells. *Nature* **2001**, *414*, 338 - 344.
10. Nanu, M.; Schoonman, J.; Goossens, A., Nanocomposite three-dimensional solar cells obtained by chemical spray deposition. *Nano Letters* **2005**, *5*, (9), 1716-1719.

11. Adachi, M.; Murata, Y.; Okada, I.; Yoshikawa, S., Formation of Titania Nanotubes and Applications for Dye Sensitized Solar Cells. *Journal. Electrochem. Soc.* **2003**, 150, (8), G488-G493.
12. Varghese, O.; Paulose, M.; Shankar, K.; Mor, G.; Grimes, C., Water-Photolysis Properties of Micron-Length Highly-Ordered Titania Nanotube-Arrays. *J. Nanosci. and Nanotech.* **2005**, 5, 1158-1165.
13. Gratzel, M., Solar Energy Conversion by Dye-Sensitized Photovoltaic Cells. *Inorganic Chemistry* **2005**, 55, (20), 6841-6851.
14. O'Hayre, R.; Nanu, M.; Schoonman, J.; Goossens, A.; Wang, Q.; Gratzel, M., The Influence of TiO₂ Particle Size in TiO₂/CuInS Nanocomposite Solar Cells. *Advanced Functional Materials* **2006**, 16, 1566-1576.
15. Limmer, S. J.; Chou, T. P.; Cao, C. Z., A Study on the Growth of TiO₂ Nanorods using Sol Electrophoresis. *J. of Mats. Sci* **2004**, 39, 895-901.
16. Jongh, P. E. d.; Vanmaekelbergh, D., Trap-Limited Electronic Transport in Assemblies of Nanometer-Sized TiO₂ Particles. *Phys. Rev. Lett* **1996**, 77, (16), 3427-3430.
17. Palgrave, R. G.; Parkin, I. P., Aerosol Assisted Chemical Vapor Deposition using Nanoparticle Precursors: A Route to Nanocomposite Thin Films. *J. Am. Chem. Soc.* **2006**, 128, (5), 1587-1597.
18. Madler, L.; Lall, A.; Friedlander, S., One-step aerosol synthesis of nanoparticle agglomerate films: simulation of film porosity and thickness. *Nanotechnology* **2006**, 17, 4783-4795.

19. Kulkarni, P.; Biswas, P., A Brownian dynamics simulation to predict morphology of nanoparticle deposits in the presence of interparticle interactions. *Aerosol Sci and Technol.* **2004**, 38, 541-554.
20. Kulkarni, P.; Biswas, P., Morphology of Nanostructured Films for Environmental Applications: Simulation of Simultaneous Sintering and Growth. *J. of Nanoparticle Research* **2003**, 5, (3-4), 259-268.
21. Krinke, T. J.; Fissan, H.; Deppert, K., Deposition of aerosol nanoparticles on flat substrate surfaces. *Phase Transitions* **2003**, 76, (4-5), 333-345 Part B.
22. Okuyama, K.; Kousaka, Y.; Tohge, N.; Yamamoto, S.; Wu, J. J.; Flagen, R. C.; Seinfeld, J. H., Production of Ultrafine Metal Oxide Aerosol Particles by Thermal Decomposition of Metal Alkoxide Vapors. *AIChE J.* **1986**, 32, (12), 2010-2019.
23. Namiki, N.; Cho, K.; Fraundorf, P.; Biswas, P., Tubular reactor synthesis of doped nanostructured titanium dioxide and its enhanced activation by coronas and soft X-rays. *Industrial & Engineering Chemistry Research* **2005**, 44, (14), 5213-5220.
24. Nakaso, K.; Fujimoto, T.; Seto, T.; Shimada, M.; Okuyama, K.; Lunden, M. M., Size distribution change of titania nano-particle agglomerates generated by gas phase reaction, agglomeration, and sintering. *Aerosol Science and Technology* **2001**, 35, (5), 929-947.
25. Chen, C. H.; Schoonman, J., Thin-film techniques for advanced energy conversion and storage systems. *Journal of Industrial and Engineering Chemistry* **2004**, 10, (7), 1114-1125.
26. Kobata, A.; Kusakabe, K.; Morooka, S., Growth and Transformation of TiO₂ Crystallites in Aerosol Reactor. *AIChE J.* **1991**, 37, (3), 347-359.

27. Friedlander, S., *Smoke Dust and Haze: Fundamentals of Aerosol Dynamics 2nd ed.* Oxford University Press, Inc. New York, New York: 2000.
28. Cho, K.; Biswas, P., Sintering rates for pristine and doped titanium dioxide determined using a tandem differential mobility analyzer system. *Aerosol Science and Technology* **2006**, 40, (5), 309-319.
29. Aduda, B. O.; Ravirajan, P.; Choy, K. L.; Nelson, J., Effect of morphology on electron drift mobility in porous TiO₂. *International Journal of Photoenergy* **2004**, 6, (3), 141-147.

Chapter 4:

Nanostructured TiO₂ Film Morphology and the Performance of Dye-Sensitized Solar Cells and Photo Water Splitting

The results presented here were published in:

Nanostructured TiO₂ films with controlled morphology synthesized in a single step process: Performance of dye-sensitized solar cells and photo watersplitting, Elijah Thimsen, Neema Rastgar and Pratim Biswas *Journal of Physical Chemistry C* **2008**, 112, (11), 4134-4140.

4.1 Abstract

Nanostructured titanium dioxide (TiO₂) films were synthesized with controlled morphology and thickness in an ambient pressure single-step flame aerosol reactor (FLAR) for use in water splitting photocells and dye-sensitized solar cells. Two different morphologies were studied: a granular morphology and a highly-crystalline columnar morphology. The granular morphology consisted of nanoparticles, approximately 10 nm in diameter, aggregated into fractal structures on the substrate. The granular morphology contained a large number of grain boundaries and other interfacial defects. The columnar morphology consisted of single crystal structures, approximately 85 nm in width, oriented normal to the substrate. The well-controlled deposition process was used to deposit films with thicknesses in the range from 98 nm to 12 μm to establish the relationship to water splitting and dye-sensitized solar cell performance. It was found that for water splitting there was an optimum thickness (~1.5 μm), which was a tradeoff between light absorption and electron transport losses, where the conversion efficiency was maximized. Due to differences in electron transport and lifetime in the TiO₂ film, for both applications the columnar morphology outperformed the granular morphology, achieving a UV-light to hydrogen conversion efficiency of 11% for water splitting and a visible light to electricity conversion efficiency of 6.0 % for the dye-sensitized solar cell.

4.2 Introduction

Nanostructured films find application in a number of areas, such as catalysis, microelectronics, and solar energy harvesting. A key aspect of effective, next-generation solar energy technology is the ability to synthesize films with controlled morphology. Titanium dioxide (TiO_2) is a semiconductor that has been extensively utilized in next-generation solar energy technology as an inexpensive alternative to silicon-based solar cells and in environmental photocatalytic applications. In its pristine state, TiO_2 absorbs only UV-light due to its wide band-gap (~ 3.2 eV). However, many researchers have developed visible-light active TiO_2 through doping¹⁻⁵ and adsorption of light-absorbing organic molecules⁶⁻⁹, giving this material potential as a means to inexpensively harvest solar energy. Photocatalytic reactors based on TiO_2 have been employed to reduce CO_2 to more useful hydrocarbons such as methane^{10, 11} and methanol^{10, 12}, which in the future could lead to novel hydrocarbon-based CO_2 sequestration techniques. Titanium dioxide has also been extensively explored as a material to photosplit water¹³, for the generation of solar-hydrogen as a sustainable source of fuel³. However, the most prominent role TiO_2 has played in the solar energy community is in photovoltaic dye-sensitized solar cells. It is the electron conduction layer in these solar cells that are an inexpensive and economically viable alternative to conventional silicon-based technology⁷. Titanium dioxide-based solar energy technology is in the nascent stages of commercialization, but for significant breakthroughs to occur, device efficiencies must be improved.

Film morphology has been identified as an important, efficiency-limiting aspect of TiO_2 films. For water splitting cells, it has been reported that crystalline structures oriented normal to the substrate have superior performance relative to irregular

disordered structures¹⁴. In addition, TiO₂ nanotubes have the highest reported UV-light to hydrogen conversion efficiency due to their morphology¹⁵. However, a systematic comparison of morphologies synthesized by the same process has not been performed.

Morphology can also affect the performance of dye-sensitized solar cells. Dye-sensitized solar cells rely on a nanostructured interpenetrating interface between an electron-conducting layer (TiO₂⁶ or ZnO¹⁶), a light-absorbing layer (Ru-based dye¹⁷, porphyrins⁸, quantum dots¹⁸) and a hole-conducting layer (redox electrolyte¹⁷, hole-conducting polymer¹⁹, p-type semiconductor²⁰) to generate and separate charge. Electron conduction layers made of TiO₂ have typically been used because electron transfer between the light-absorber and TiO₂ is more efficient than other materials such as ZnO¹⁶. The electron-conducting TiO₂ layer serves two important functions. First, it provides a large surface area onto which the light-absorbing agent is immobilized, while maintaining short transport distances to the substrate (~ μm). Second, the TiO₂ conducts electrons generated by light-absorbing layer to the substrate where they are collected. Surface area, electron transport and electron lifetime are critical to device performance²¹. Nanoparticles are typically used to fabricate films for TiO₂ solar cells, owing to their high specific surface area^{6, 7}. However, recent studies have found that TiO₂ films fabricated using larger particles, which are believed to have better electron transport properties, resulted in improved device performance^{22, 23}. In addition, inclusion of larger particles has also been found to improve optical properties of the titania film^{17, 24}. Overall, previous research has shown that control over morphology is critical, as it can be used to optimize conversion efficiency. Morphology is ultimately determined by the synthesis process.

A variety of synthesis techniques have been employed to synthesize TiO₂ films. These synthesis methods include: thermal oxidation¹ and anodization²⁵ of titanium foils, dip-coating²⁶, screen-printing²⁷, sol-gel processes²⁸, sputtering¹⁴, spray-pyrolysis²⁹ and chemical vapor deposition³⁰, among others. High-performance film morphologies can be obtained through these processes, but the synthesis is either difficult to control, involves multiple time-consuming steps, or the use of expensive processing equipment. The use of such time-consuming and expensive processing is undesirable for the widespread industrial production of films that would be required to harvest a meaningful amount of solar energy. There is a need for a robust, inexpensive synthesis process to fabricate high-performance films in a single step that provides rational control over film morphology.

Flame aerosol reactors (FLAR) are an attractive way to synthesize TiO₂ films. Flame aerosol reactors are single step, gas-phase, most commonly atmospheric pressure, and allow rapid processing^{31, 32}. Flame-based processes are commonly used in industry to synthesize nanomaterials, and produce millions of tons per year of carbon black, paint pigments, optical fibers and many other valuable products. Detailed models have been developed to predict morphology and other characteristics of films produced by these processes³³⁻³⁵. Recently, a premixed flame reactor was used to synthesize TiO₂ films with controlled morphology and thickness, where both had a significant impact on photocurrent generation³¹. The controlled morphology of TiO₂ films produced in the FLAR can take two forms, granular and columnar, which can be used to optimize the film architecture to meet the needs of specific applications.

For this study, a premixed methane-oxygen flame aerosol reactor was used to fabricate TiO₂ films with controlled morphology and thickness. These films were then used for two different applications, photocatalytic water splitting and photovoltaic dye-sensitized solar cells. The relationship of nanostructured film morphology and thickness to performance was systematically studied, using films deposited by a single step synthesis process.

4.3 Experimental Methods

4.3.1 Film Synthesis

A detailed description of the flame aerosol reactor is presented elsewhere³¹; a brief summary of the experimental parameters is presented here. A schematic of the reactor is presented in Figure 4-1. The titanium dioxide films were deposited onto ITO coated aluminosilicate glass substrates (Delta Technologies, Stillwater MN). The thickness of the ITO coating was about 200 nm. The substrates were used as received. During deposition, intimate thermal contact was established between the substrate and substrate holder through the application of a small amount of silver thermal paste (Arctic Silver, Visalia CA) to the backside of the substrate. Titanium tetra-isopropoxide (TTIP, >98% purity, Sigma-Aldrich) was the Ti precursor, and was used as received. The substrate temperature was monitored online by a type K thermocouple embedded in the holder about 1/8" behind the backside of the substrate. The distance from the outlet of the burner to the substrate, or burner-substrate distance, was used as a process parameter to simultaneously vary the residence time in the flame and substrate temperature. The burner-substrate distance was varied in the range from 1.7 cm to 6.0 cm.

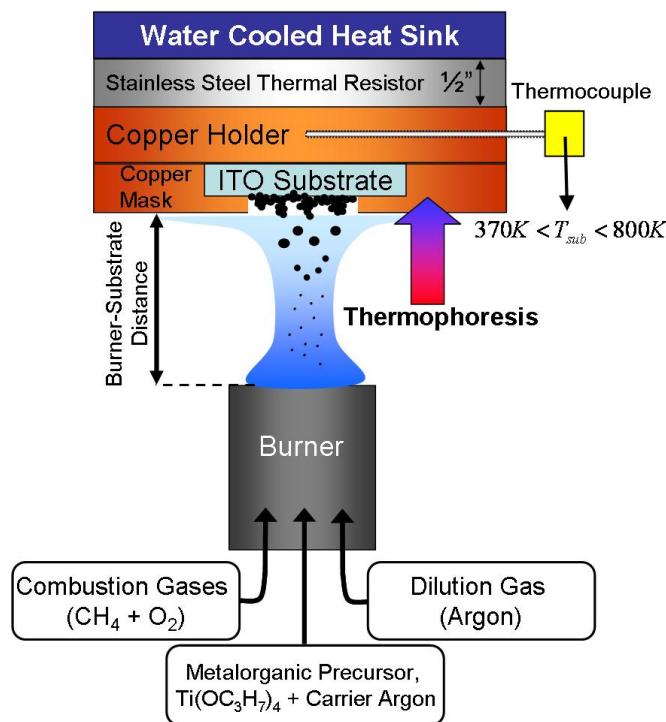


Figure 4-1: Schematic of the flame aerosol reactor (FLAR) system used to deposit nanostructured TiO₂ films with controlled morphology in a single step.

The process gasses for the flame were controlled using digital mass flow controllers (MKS Instruments, Wilmington MA). The following sets of process parameters were used for films synthesized for water splitting and the dye-sensitized solar cells. For water splitting, the total argon, oxygen and methane flow rates were held constant at 4.0 lpm (liters per minute at STP), 2.7 lpm and 0.9 lpm respectively. Using a home-made bubbler, The TTIP feed rate was held constant at approximately 1.2 mmol hr⁻¹. The burner outlet area was about 0.14 cm². The films for the dye-sensitized solar cells were synthesized at slightly different conditions. The flow rates of argon, oxygen and methane were 6.0 lpm, 4.0 lpm and 1.35 lpm respectively. The TTIP precursor feed rate was approximately 1.2 mmol hr⁻¹ and the burner outlet area was about 0.178 cm². Due to the highly oxidizing conditions and the elevated temperatures in the flame region, no partially oxidized carbonaceous products are expected in this system³⁶.

The arrival size of particles at the substrate is an important process parameter that influences the film final morphology. For size analysis, particles were extracted from the flame at the deposition point using a custom-made dilution probe and then deposited onto lacey carbon transmission electron microscope (TEM) grids. A JEOL 2100 FEG TEM operating at 200 kV was used to image the particles. From the images, the average particle size was determined by measuring the diameters of approximately 250 particles.

4.3.2 Film Characterization

The nanostructured TiO₂ films were characterized using several analytical techniques. The crystalline phase was determined by x-ray diffraction using a Rigaku DMax x-ray diffractometer. Anatase was the dominant crystalline phase for all of the films in this study. Example XRD patterns are presented in Figure 4-4. No preferred orientation was observed for the films in this study. The average grain size was measured from the broadening of the $2\theta = 25.6^\circ$ anatase peak using the Scherrer equation. The morphology and film thickness were determined from scanning electron microscopy (SEM) using a Hitachi model S-4500 field emission electron microscope operating at 15 kV. The SEM specimens were prepared by first cleaving the substrate down the middle of the area occupied by the TiO₂ film. The cleaved films were then mounted vertically on specimen mounts and subsequently coated with a 5 nm layer of gold to prevent charging. The films were imaged from the side in the SEM to verify morphology and measure thickness. Alternatively, a JEOL 2100 FEG TEM operating at 200 kV was used for TEM analysis of the films. TEM specimens were prepared by mechanically removing film elements from the substrate using a scalpel, and placing them onto lacey carbon grids (Ted Pella, Redding CA).

4.3.3 Photo Water Splitting

Water splitting performance was characterized using a standard 2 electrode photocell³ with a platinum wire counter electrode and 1 M KOH electrolyte. The pristine TiO₂ films were illuminated with a UV-light ($\lambda < 400\text{nm}$) light intensity of 24 mW cm^{-2} from a 400W Xe arc lamp (Oriel), as measured by a spectroradiometer with a NIST-traceable calibration (International Light, Peabody MA). The measured light irradiance was not corrected for intensity losses at the quartz walls of the photocell. In the external circuit, a constant bias (0.8 V vs. platinum) was applied using a DC power supply to enhance the extraction of electrons from the TiO₂ film¹. The current through the external circuit was measured using an ammeter (Keithley), normalized by the macroscopic substrate area occupied by the film, and assumed proportional to the hydrogen production rate. The current without illumination was about $30 \mu\text{A cm}^{-2}$.

4.3.4 Dye-sensitized solar cell

Dye-sensitized solar cells were constructed using conventional procedures and components^{17, 24}. A Ru-based dye (Ruthenium 535-bisTBA, Solaronix, Aubonne Switzerland) was used to sensitize the TiO₂ films to visible light. Before dye adsorption, the TiO₂ films were heated to 120 °C for about 30 minutes, to remove water from the film surface. While still warm, the films were placed into a 0.3 mM anhydrous ethanol-dye solution and soaked overnight (~12 hours), to adsorb dye onto the film surface. Counter-electrodes were fabricated by sputter-coating a ~150 nm platinum film onto ITO-coated glass substrates. The photoelectrode (dye-TiO₂) and counter electrode (Pt) were sandwiched together using multiple layers of a commercially available sealant (SX 1170, Solaronix). The two electrodes were separated by about 0.5 mm of electrolyte, which

was introduced into the cell through two small filling holes. An acetonitrile-based electrolyte (AN-50, Solaronix) with I^-/I_3^- as the redox couple was used to transfer electrons from the platinum counter electrode to complete the circuit by regenerating oxidized dye molecules on the TiO_2 film surface.

Several solar cell parameters were measured. Before cell construction, the amount of dye on the TiO_2 film surface was measured by desorbing the dye using a 1 mM KOH solution and measuring the light absorption of the desorbed dye solution with a calibrated UV-vis spectrometer²⁴ (Perkin-Elmer, Waltham MA). The amount of dye on the film surface was normalized by the macroscopic substrate area occupied by the film ($\sim 1\text{cm}^2$). For completed cells, under backside illumination by a Xe arc lamp equipped with both an AM1.5G filter and water filter, at a measured intensity of 124 mW cm^{-2} (1.24 Suns), the current-voltage (I-V) characteristics were measured to determine the open-circuit voltage (V_{oc}), short-circuit current (I_{sc}), fill factor (FF) and conversion efficiency^{17, 24}. The solar cells were masked to define an active area of about 0.2 cm^2 . Lastly, to obtain information about the electron lifetime in the TiO_2 films, photovoltage transient measurements were performed on unmasked cells by monitoring the decay of the open-circuit voltage after a $60\text{ }\mu\text{s}$, 5000 mJ pulse from a Xe flash-lamp (Newport, Stratford CT).

4.4 Results and Discussion

4.4.1 Film synthesis

Films with two different morphologies were synthesized for this study. The first morphology was granular and consisted of nanoparticles caked onto the substrate. This morphology is illustrated by the electron micrographs in Figure 4-2. For the granular

morphology, nanoparticles were deposited from the aerosol-phase to form fractal structures on the substrate and underwent little or no restructuring once deposited³¹. In Figure 4-2, low and high resolution TEM images are presented for a granular fractal that was mechanically removed from the substrate. It can be seen from the rings in the diffraction pattern that the granular morphology was polycrystalline anatase, with grains that were about 10 nm in size. This size agreed with the 13 nm average crystal size measured from XRD peak broadening using the Sherrer equation (Figure 4-4). The granular morphology contained a large number of grain boundaries and other defects located at particle-particle interfaces. These interfacial defects are known to inhibit charge-carrier transport and promote recombination in the TiO₂ film^{37, 38}.

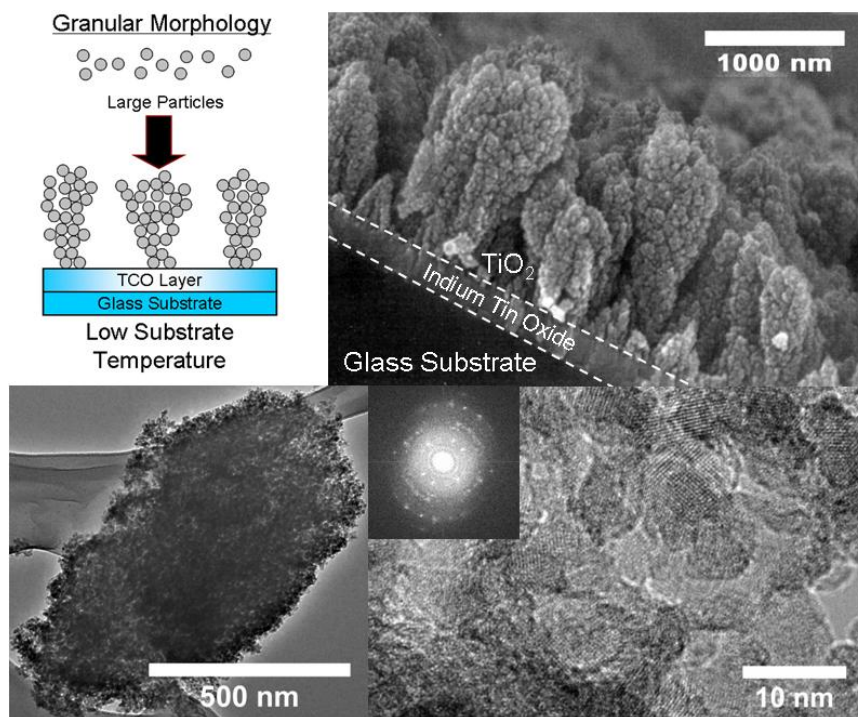


Figure 4-2: Side-view SEM image (upper right) of a granular film deposited at a burner-substrate distance of 4.1 cm, low resolution (lower left) and high resolution (lower right) TEM images of a granular fractal mechanically removed from the substrate. The inset shows the Fast Fourier Transform (FFT) of the high-resolution TEM image, exhibiting polycrystalline electron diffraction rings corresponding to the (101), (004), (200), (105) and (205) reflections of anatase, moving from the center outwards.

The second morphology was columnar, which consisted of highly crystalline structures oriented normal to the substrate (Figure 4-3). For the columnar morphology, nanoparticles were deposited out of the flame onto the substrate where they completely sintered to form continuous column-like structures³¹. From the XRD pattern (Figure 4-4), the average grain size of the columnar morphology was about 85 nm, which corresponds to the approximate width of the columns, as seen in Figure 4-3. High resolution TEM analysis of single columns scraped off the substrate revealed that the individual columns had long-range crystalline order. In many cases the columns were single crystals. There were a reduced number of grain-boundaries and interfacial defects in the columnar films.

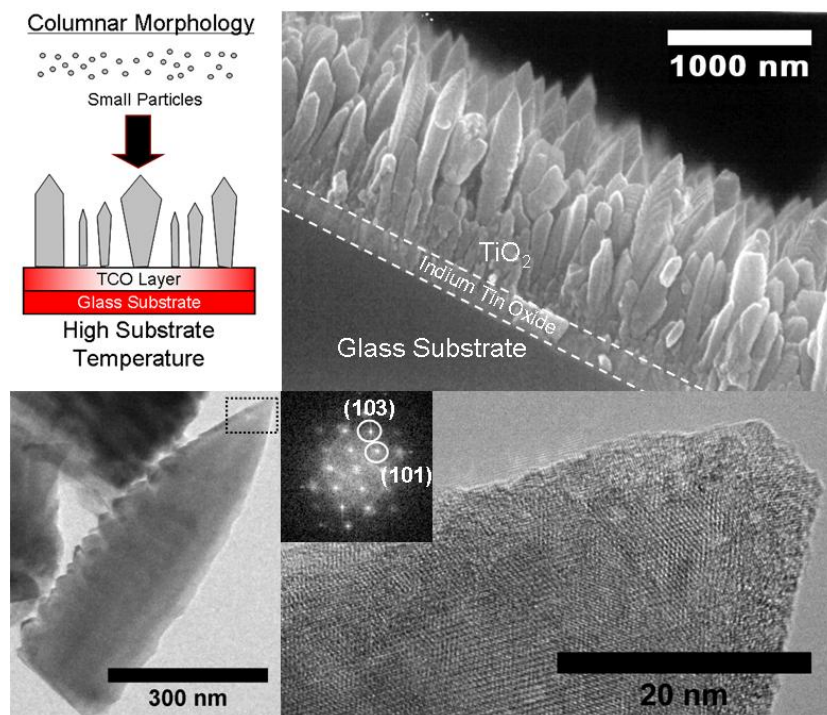


Figure 4-3: Side-view SEM image (upper right) of a columnar film deposited at a burner-substrate distance of 1.7 cm, low resolution (lower left) and high resolution (lower right) TEM images of a highly-crystalline single column mechanically removed from the substrate. The inset shows the Fast Fourier Transform (FFT) of the high-resolution TEM image, exhibiting single crystal electron diffraction from the (103) and (101) planes of anatase.

The film morphology, granular vs. columnar, is determined by the particle sintering behavior on the substrate³¹. For slow sintering dynamics, granular films are formed. Alternatively, the columnar morphology is formed when sintering dynamics are rapid. Sintering, a solid state diffusion process, is a strong function of both initial particle diameter and temperature. The characteristic time for two particles of the same initial diameter to completely sinter into an equivalent-volume sphere scales with initial diameter to the fourth power and exponentially decreases with increasing temperature^{39, 40}. Thus, for smaller particles and higher temperatures sintering is rapid; and for larger particles and lower temperatures sintering is slow. The arrival size of particles at the substrate and the substrate temperature are parameters that can be rationally varied to precisely control the film morphology through their influence on sintering dynamics.

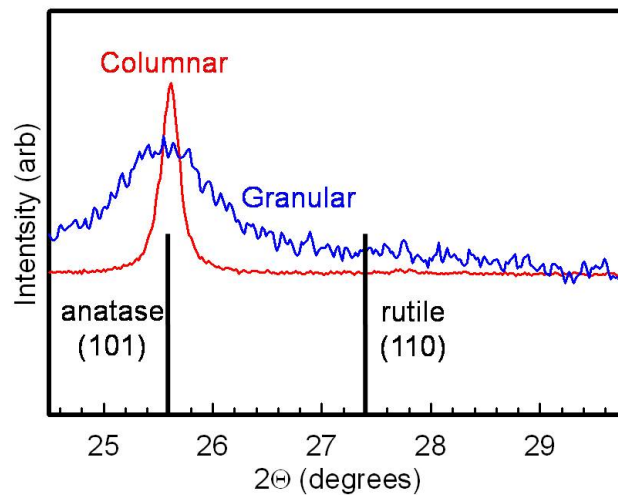


Figure 4-4: Example x-ray diffraction patterns for two as-prepared films, a 7.5 μm granular (blue) and a 6.9 μm columnar (red). The grain size measured from the peak broadening using the Scherrer equation was approximately 13 nm for the granular film and 85 nm for the columnar film.

The sintering behavior on the substrate was controlled by systematically altering the arrival size of particles at the substrate and the substrate temperature. These parameters were varied simultaneously through the burner-substrate distance. It is known that particle size increases with residence time in particle synthesis processes^{41, 42}, which in this case changed with the burner-substrate distance. In addition, the temperature distribution in the premixed flame was a function of axial position and was used to tune the substrate temperature through its influence on heat transfer to the water-cooled heat sink (Figure 4-1). The particle size and substrate temperature were measured at two burner-substrate distances, 1.7 cm and 4.1 cm. The measured substrate temperature was 190 °C and 130 °C for 1.7 cm and 4.1 cm respectively. It should be noted that the measured substrate temperature was much lower than the actual surface temperature of the substrate, due to resistance-induced temperature drops between the substrate surface and measurement location, which was 1/8" behind the substrate (Figure 4-1). The average particle size, measured from TEM images of particles extracted from the flame, was 3.1 nm and 3.9 nm at 1.7 cm and 4.1 cm. For the shorter burner-substrate distance, smaller particles were deposited at a higher substrate temperature, resulting in rapid sintering dynamics on the substrate and the formation of TiO₂ films with the columnar morphology (Figure 4-3). At the longer burner-substrate distance, slightly larger particles were deposited at a reduced substrate temperature, resulting in slower sintering dynamics and films with the granular morphology (Figure 4-2). The final film morphology proved important to control, as it significantly affected the performance of the TiO₂ films.

4.4.2 Photo Water Splitting

The water splitting photocurrent was measured for columnar and granular films of varying thickness. Columnar films were deposited at a burner-substrate distance of 1.7 cm with thicknesses in the range from 100 to 3000 nm; while granular films were deposited at 4.1 cm in the thickness range 600 to 12000 nm. The film thickness was controlled by varying the deposition time in the range from 30 seconds to 17 minutes, longer deposition times corresponding to thicker films³¹.

A new equation was used to determine the energy conversion efficiency because the conventional equations^{1, 15} are known to inaccurately estimate⁴³ the contribution of the DC power supply. The efficiency was estimated from the photocurrent by performing an energy balance on the water splitting cell. Energy entered the cell in the form of UV-light and electrical work, and left the cell in the form of hydrogen gas. The ratio of energy-output to energy-input was taken as the efficiency, using the following equation:

$$\eta = \frac{j_p E_H^o}{I_o + j_p V_{app}} \quad (4-1)$$

where j_p is the measured photocurrent ($j_p = j_{p,light} - j_{p,dark}$), E_H^o is the standard reduction potential of water formation from hydrogen and oxygen (1.23 V), I_o is the incident light intensity (24 mW cm^{-2}) and V_{app} is the output of the power supply (0.8 V). Both thickness and morphology had a significant effect on the water splitting performance. Water splitting photocurrent and conversion efficiencies are presented in Figure 4-5.

The photocurrent increased with thickness, until reaching a critical value, and then decreased for thicker films. This behavior was observed for both morphologies. The critical thickness was an optimum balance between light absorption and charge transport losses. As the film thickness increased, more light was absorbed. However, after a certain point the light absorption saturated. Any increase in thickness beyond the critical value increased the time it took for charge-carriers to migrate through the film, making recombination processes more competitive with transport. Both morphologies have a similar critical thickness, because this is the system-specific material-dependent point where light absorption is maximized. Along these lines, photocurrent-thickness plots, such as the ones in Figure 4-5 can be divided into two different regions. Films thinner than the critical value are light-absorption limited, while thicker films are transport limited.

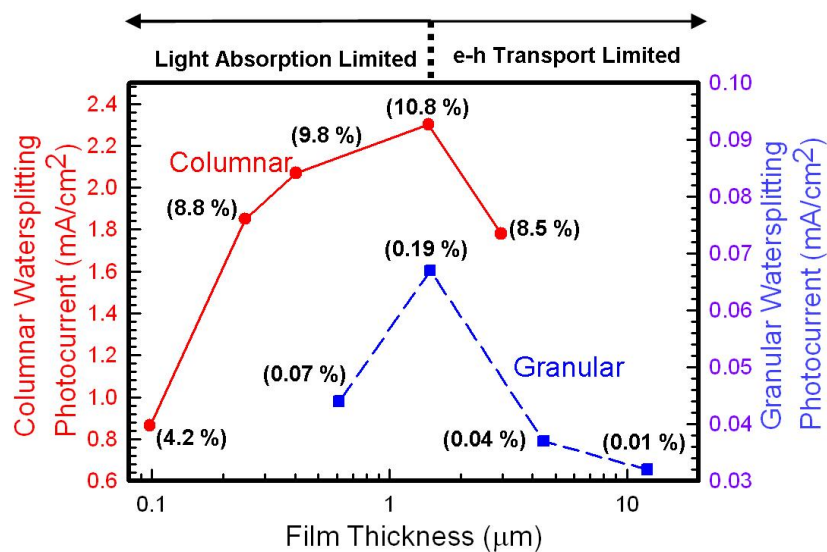


Figure 4-5: Water splitting photocurrent as a function of film thickness for the columnar films deposited at a burner-substrate distance of 1.7 cm (red); and granular films deposited at 4.1 cm (blue). The hydrogen conversion efficiency, calculated using equation 4-1, is in parenthesis next to each point.

The photocurrent was also a strong function of film morphology. It can be seen from Figure 4-5, the columnar films deposited at 1.7 cm had a maximum conversion efficiency approximately 50 times higher than the granular films deposited at 4.1 cm.

The columnar films had higher photocurrents because of their superior electronic properties. For FLAR-produced TiO₂ films, the columnar morphology has been found to have a higher photoconductivity relative to the granular morphology³¹. Also, it has been reported that particle-particle interfaces in granular films present migration barriers for electrons, increasing the time it takes for electrons to be transported in the film and thus making recombination more competitive with transport⁴⁴. Additionally, it is known that for films produced by different synthesis processes, electron drift velocities are higher in films with columnar morphologies than in granular films³⁷. However, other oriented morphologies, such as TiO₂ nanotubes, have been found to have similar transport characteristics to granular films. Despite the similar electron transport characteristics, TiO₂ nanotubes were found to have an order of magnitude longer electron lifetime relative to granular films³⁸. Experimental results from transient photovoltage measurements performed on dye-sensitized solar cells presented later in this paper suggest that the electron lifetime is longer in the columnar films than in the granular, resulting in superior electronic properties and performance. While dye-sensitized solar cells are a different system than water splitting cells, it is reasonable to conclude that in the case of water splitting, the highly crystalline columnar films have generally superior electronic properties (longer charge carrier lifetimes and shorter transport times) to the granular films, resulting in higher photocurrents, and greatly improved water splitting performance.

4.4.3 Dye-sensitized Solar Cell

Solar cells were constructed using 3 different TiO₂ films, 2 columnar films and 1 granular film. The columnar films were of different thicknesses, 1.9 μm and 6.9 μm . The granular film had a thickness of 7.5 μm .

The I-V characteristics for the three solar cells are presented in Figure 4-6, and the measured cell parameters are presented in Table 4-1. All three of the cells have similar open-circuit voltages and fill factors. The primary difference between the cells is in the short-circuit current.

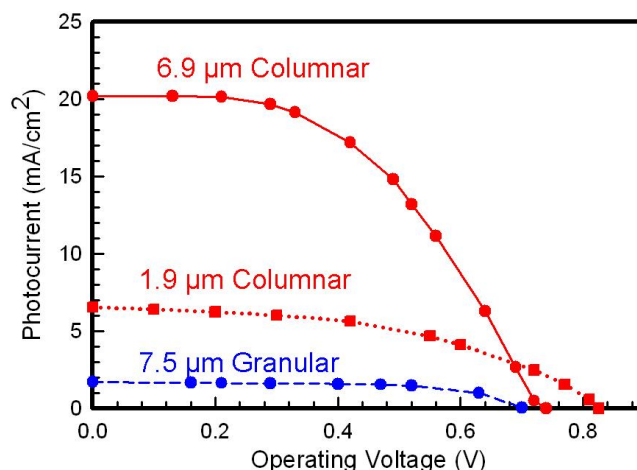


Figure 4-6: Dye-sensitized solar cell performance characteristics – photocurrent as a function of operating voltage for a 1.9 μm columnar film (dotted-red), 6.9 μm columnar (solid-red) and a 7.5 μm granular film (dashed-blue).

The current generated by the solar cells was a function of TiO₂ film thickness, through its influence on total surface area of the columnar films. For the columnar morphology, the 6.9 μm film generated 20.2 mA cm⁻² of current at short circuit conditions, while the 1.9 μm film only generated 6.55 mA cm⁻². This difference is a result of light absorption. In dye-sensitized solar cells, the dye molecules on the film surface absorb light and inject electrons into the TiO₂ film. It can be seen from Table 4-1 that the

6.9 μm film adsorbs about 2.70×10^{-8} mol of dye while the 1.9 μm film only adsorbs 1.05×10^{-8} mol. Keeping in mind that these films have a columnar nanostructure, the difference is due to a larger total surface area present on the 6.8 μm film, compared to the 1.9 μm film. Assuming that the dye is present as a monolayer on the TiO_2 film surface, more dye molecules will result in an increased number of electrons injected into the TiO_2 film, resulting in more current generated by the solar cell. If the thickness were further increased, the light absorption would eventually saturate, and then decay in a similar way to the water splitting trend with thickness.

Table 4-1: Summary of the dye-sensitized solar cell performance metrics for cells constructed using different TiO_2 films.

morphology	film thickness (μm)	dye adsorbed (10^{-8} mol cm^{-2})	V_{oc} (V)	I_{sc} (mA cm^{-2})	FF	η
columnar	1.9	1.05	0.83	6.55	0.48	2.1%
columnar	6.9	2.70	0.74	20.2	0.49	6.0%
granular	7.5	3.27	0.75	1.71	0.59	0.6%

The performance of the solar cells was also a strong function of morphology. From Table 4-1, the 6.9 μm columnar film produced 20.2 mA cm^{-2} of current at short-circuit conditions, while the 7.5 μm granular film only generated 1.71 mA cm^{-2} . In this case, the two films had a similar amount of dye adsorbed onto the film surface, 3.27×10^{-8} mol for the granular compared to 2.7×10^{-8} mol for the columnar. Therefore, these two cells absorbed similar amounts of light. The columnar film generated more current in part because of longer electron lifetimes.

The electron lifetime was measured using transient voltage measurements, for the 6.9 μm columnar and 7.5 μm granular film. The electron lifetime, which is a function of

the open-circuit voltage, can be estimated from the transient photovoltage characteristic using the following equation^{21, 45}:

$$\tau_{lifetime} = \frac{-k_b T}{e} \left(\frac{dV}{dt} \right)^{-1} \quad (4-2)$$

where $\frac{dV}{dt}$ is the time derivative of the photovoltage transient at a given V_{oc} , k_b is the Boltzmann constant, T is the solar cell temperature and e is the unit charge. The measured photovoltage transients and the calculated electron lifetimes are plotted in Figure 4-7. It can be seen from Figure 4-7 that at a given open circuit voltage, the electron lifetime in the granular film is about a factor of 10 shorter than the lifetime in the columnar film.

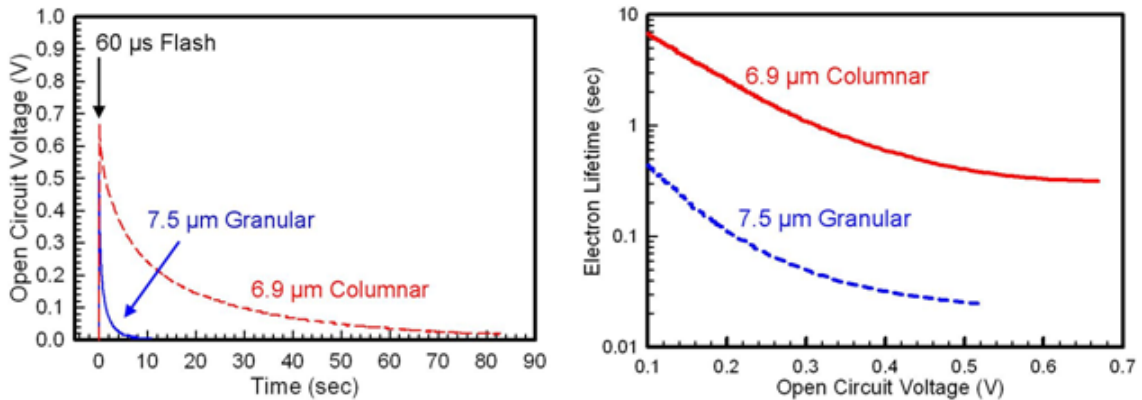


Figure 4-7: Measured photovoltage transients (left) and electron lifetimes (right). The lifetimes were calculated using equation 4-2, as a function of open circuit voltage for solar cells using columnar (red) and granular (blue) films.

The difference in electron lifetime is an explanation for the lower photocurrent measured in the granular film. In the granular film, electron recombination was faster, which influenced the number of electrons collected at the substrate. It took a finite amount of time for electrons to be transported through the film and be collected at the

substrate. For electrons to be collected, the transport time must be less than the corresponding lifetime. Considering there was a distribution of electron lifetimes and transport times, for a given amount of injected electrons, a lower fraction were collected at the substrate in the shorter-lifetime granular case, resulting in a lower short-circuit current and poorer conversion efficiency. This result further supports the hypothesis that for water splitting and dye-sensitized solar cells the granular morphology has generally inferior electronic properties when compared to the columnar morphology.

4.5 Conclusions

A robust single step film synthesis process allowed the deposition of films with well controlled characteristics. Two different morphologies of TiO₂ films were prepared at ambient pressure, using this single step process. The first morphology was polycrystalline and granular, which consisted of fractal structures of nanoparticles on the substrate. Second, a columnar morphology was studied that consisted of single crystal columns of anatase TiO₂ oriented normal to the substrate surface. The performance of these films was tested in two different devices, water splitting and dye-sensitized solar cells. For both devices, the columnar morphology outperformed the granular by a factor of 10 or more. Morphology was found to have a dominant effect on photo conversion efficiency. The single step synthesis methods demonstrated that the morphology could be readily controlled in the FLAR system.

This result has implications to novel material design. Many researchers are attempting to fabricate efficient, visible-light active oxide materials. Attention must be paid to the morphology of these materials, as the morphology can affect performance

over orders of magnitude. The flame aerosol reactor is a valuable tool to study novel material synthesis. It can be used to control the morphology of the film, and can also rapidly synthesize different materials by simply choosing appropriate gas-phase precursors.

4.6 Acknowledgements

We acknowledge partial support from the NSF- NIRT 0304649 Grant, and the Center for Materials Innovation (CMI) at Washington University in Saint Louis.

4.7 References:

1. Ingler, W. B.; Al-Shahr, M.; Kahn, S. U. M., Efficient Photochemical Water Splitting by a Chemically Modified n-TiO₂. *Science* **2002**, 297, 2243-2245.
2. Park, J. H.; Kim, S.; Bard, A. J., Novel carbon-doped TiO₂ nanotube arrays with high aspect ratios for efficient solar water splitting. *Nano Letters* **2006**, 6, (1), 24-28.
3. Nowotny, J.; Sorell, C. C.; Sheppard, L. R.; Bak, T., Solar-hydrogen: Environmentally safe fuel for the future. *International Journal of Hydrogen Energy* **2005**, 30, 521-544.
4. Kisch, H.; Sakthivel, S.; Janczarek, M.; Mitoraj, D., A low-band gap, nitrogen-modified titania visible-light photocatalyst. *Journal of Physical Chemistry C* **2007**, 111, (30), 11445-11449.
5. Reyes-Garcia, E. A.; Sun, Y. P.; Reyes-Gil, K.; Raftery, D., N-15 solid state NMR and EPR characterization of N-doped TiO₂ photocatalysts. *Journal of Physical Chemistry C* **2007**, 111, (6), 2738-2748.

6. Nazeeruddin, M. K.; Kay, A.; Rodicio, I.; Humphry-Baker, R.; Muller, E.; Liska, P.; Vlachopoulos, N.; Gratzel, M., Conversion of Light to Electricity by *cis*-X₂Bis(2,2'-bipyridyl-4,4'-dicarboxylate)ruthenium(II) Charge Transfer Sensitizers (X=Cl-, Br-, I-, CN-, and SCN-) on Nanocrystalline TiO₂ Electrodes. *J. Am. Chem. Soc.* **1993**, 115, 6382-6390.
7. Gratzel, M., Photoelectrochemical Cells. *Nature* **2001**, 414, 338 - 344.
8. Campbell, W. M.; Jolley, K. W.; Wagner, P.; Wagner, K.; Walsh, P. J.; Gordon, K. C.; Schmidt-Mende, L.; Nazeeruddin, M. K.; Wang, Q.; Gratzel, M.; Officer, D. L., Highly Efficient Porphyrin Sensitizers for Dye-Sensitized Solar Cells. *J. Phys. Chem. C* **2007**, 111, (32), 11760-11762.
9. Huijser, A.; Marek, P. L.; Savenije, T. J.; Siebbeles, L. D. A.; Scherer, T.; Hauschild, R.; Szmytkowski, J.; Kalt, H.; Hahn, H.; Balaban, T. S., Photosensitization of TiO₂ and SnO₂ by Artificial Self-Assembling Mimics of the Natural Chlorosomal Bacteriochlorophylls. *J. Phys. Chem. C* **2007**, 111, (31), 11726-11733.
10. Yamashita, H.; Kamada, N.; He, H.; Tanaka, K.; Ehara, S.; Anpo, M., Reduction of CO₂ with H₂O on TiO₂(100) and TiO₂(110) Single-Crystals under UV-Irradiation. *Chemistry Letters* **1994**, (5), 855-858.
11. Ozcan, O.; Yukruk, F.; Akkaya, E. U.; Uner, D., Dye sensitized artificial photosynthesis in the gas phase over thin and thick TiO₂ films under UV and visible light irradiation. *Applied Catalysis B-Environmental* **2007**, 71, (3-4), 291-297.
12. Wu, J. C. S.; Lin, H. M., Photo reduction of CO₂ to methanol via TiO₂ photocatalyst. *International Journal of Photoenergy* **2005**, 7, (3), 115-119.

13. Fujishima, A.; Honda, K., Electrochemical Photolysis of Water at a Semiconductor Electrode. *Nature* **1972**, 238, 37.
14. Su, Y. F.; Chou, T. C.; Ling, T. R.; Sun, C. C., Photocurrent performance and nanostructure analysis of TiO₂/ITO electrodes prepared using reactive sputtering. *Journal of the Electrochemical Society* **2004**, 151, (9), A1375-A1382.
15. Paulose, M.; Shankar, K.; Yoriya, S.; Prakasam, H. E.; Varghese, O. K.; Mor, G. K.; Latempa, T. A.; Fitzgerald, A.; Grimes, C. A., Anodic growth of highly ordered TiO₂ nanotube arrays to 134 μm in length. *Journal of Physical Chemistry B* **2006**, 110, (33), 16179-16184.
16. Quintana, M.; Edvinsson, T.; Hagfeldt, A.; Boschloo, G., Comparison of dye-sensitized ZnO and TiO₂ solar cells: Studies of charge transport and carrier lifetime. *Journal of Physical Chemistry C* **2007**, 111, (2), 1035-1041.
17. Chiba, Y.; Islam, A.; Watanabe, Y.; Komiya, R.; Koide, N.; Han, L. Y., Dye-sensitized solar cells with conversion efficiency of 11.1%. *Japanese Journal of Applied Physics Part 2-Letters & Express Letters* **2006**, 45, (24-28), L638-L640.
18. Plass, R.; Pelet, S.; Krueger, J.; Gratzel, M.; Bach, U., Quantum dot sensitization of organic-inorganic hybrid solar cells. *Journal of Physical Chemistry B* **2002**, 106, (31), 7578-7580.
19. Bach, U.; Lupo, D.; Comte, P.; Moser, J. E.; Weissortel, F.; Salbeck, J.; Spreitzer, H.; Gratzel, M., Solid-state dye-sensitized mesoporous TiO₂ solar cells with high photon-to-electron conversion efficiencies. *Nature* **1998**, 395, (6702), 583-585.
20. Nanu, M.; Schoonman, J.; Goossens, A., Nanocomposite three-dimensional solar cells obtained by chemical spray deposition. *Nano Letters* **2005**, 5, (9), 1716-1719.

21. Frank, A. J.; Kopidakis, N.; van de Lagemaat, J., Electrons in nanostructured TiO₂ solar cells: transport, recombination and photovoltaic properties. *Coordination Chemistry Reviews* **2004**, 248, (13-14), 1165-1179.
22. O'Hayre, R.; Nanu, M.; Schoonman, J.; Goossens, A.; Wang, Q.; Gratzel, M., The Influence of TiO₂ Particle Size in TiO₂/CuInS Nanocomposite Solar Cells. *Advanced Functional Materials* **2006**, 16, 1566-1576.
23. Chou, T. P.; Zhang, Q. F.; Russo, B.; Fryxell, G. E.; Cao, G. Z., Titania particle size effect on the overall performance of dye-sensitized solar cells. *Journal of Physical Chemistry C* **2007**, 111, (17), 6296-6302.
24. Wang, Z. S.; Kawauchi, H.; Kashima, T.; Arakawa, H., Significant influence of TiO₂ photoelectrode morphology on the energy conversion efficiency of N719 dye-sensitized solar cell. *Coordination Chemistry Reviews* **2004**, 248, (13-14), 1381-1389.
25. Varghese, O.; Paulose, M.; Shankar, K.; Mor, G.; Grimes, C., Water-Photolysis Properties of Micron-Length Highly-Ordered Titania Nanotube-Arrays. *J. Nanosci. and Nanotech.* **2005**, 5, 1158-1165.
26. Sahle-Demessie, E.; Gonzalez, M.; Wang, Z. M.; Biswas, P., Synthesizing alcohols and ketones by photoinduced catalytic partial oxidation of hydrocarbons in TiO₂ film reactors prepared by three different methods. *Industrial & Engineering Chemistry Research* **1999**, 38, (9), 3276-3284.
27. Karthikeyan, C. S.; Thelakkat, M.; Willert-Porada, M., Different mesoporous titania films for solid-state dye sensitised solar cells. *Thin Solid Films* **2006**, 511, 187-194.

28. Limmer, S. J.; Chou, T. P.; Cao, C. Z., A Study on the Growth of TiO₂ Nanorods using Sol Electrophoresis. *J. of Mats. Sci* **2004**, 39, 895-901.
29. Kavan, L.; Gratzel, M., Highly Efficient Semiconducting TiO₂ Photoelectrodes Prepared by Aerosol Pyrolysis. *Electrochimica Acta* **1995**, 40, (5), 643-652.
30. Goossens, A.; Maloney, E. L.; Schoonman, J., Gas-phase synthesis of nanostructured anatase TiO₂. *Chemical Vapor Deposition* **1998**, 4, (3), 109-114.
31. Thimsen, E.; Biswas, P., Nanostructured photoactive films synthesized by a flame aerosol reactor. *Aiche Journal* **2007**, 53, (7), 1727-1735.
32. Madler, A. L.; Roessler, A.; Pratsinis, S. E., Direct Formation of Highly Porous Gas-Sensing Films by in-situ Thermophoretic Deposition of Flame-Made Pt/SnO₂ Nanoparticles. *Sensors and Actuators B-Chemical* **2006**, 114, (1), 283-295.
33. Madler, L.; Lall, A.; Friedlander, S., One-step aerosol synthesis of nanoparticle agglomerate films: simulation of film porosity and thickness. *Nanotechnology* **2006**, 17, 4783-4795.
34. Kulkarni, P.; Biswas, P., Morphology of Nanostructured Films for Environmental Applications: Simulation of Simultaneous Sintering and Growth. *J. of Nanoparticle Research* **2003**, 5, (3-4), 259-268.
35. Kulkarni, P.; Biswas, P., A Brownian dynamics simulation to predict morphology of nanoparticle deposits in the presence of interparticle interactions. *Aerosol Sci and Technol.* **2004**, 38, 541-554.
36. Yang, G.; Biswas, P.; Boolchand, P.; Sabata, A., Deposition of Multifunctional Titania Films by Aerosol Routes. *J. Am. Ceramic Soc.* **1999**, 82, (10), 2573-2579.

37. Aduda, B. O.; Ravirajan, P.; Choy, K. L.; Nelson, J., Effect of morphology on electron drift mobility in porous TiO₂. *International Journal of Photoenergy* **2004**, 6, (3), 141-147.
38. Zhu, K.; Neale, N. R.; Miedaner, A.; Frank, A. J., Enhanced charge-collection efficiencies and light scattering in dye-sensitized solar cells using oriented TiO₂ nanotubes arrays. *Nano Letters* **2007**, 7, (1), 69-74.
39. Kobata, A.; Kusakabe, K.; Morooka, S., Growth and Transformation of TiO₂ Crystallites in Aerosol Reactor. *AIChE J.* **1991**, 37, (3), 347-359.
40. Cho, K.; Biswas, P., Sintering rates for pristine and doped titanium dioxide determined using a tandem differential mobility analyzer system. *Aerosol Science and Technology* **2006**, 40, (5), 309-319.
41. Mangolini, L.; Thimsen, E.; Kortshagen, U., High-yield plasma synthesis of luminescent silicon nanocrystals. *Nano Letters* **2005**, 5, (4), 655-659.
42. Jiang, J.; Chen, D. R.; Biswas, P., Synthesis of nanoparticles in a flame aerosol reactor with independent and strict control of their size, crystal phase and morphology. *Nanotechnology* **2007**, 18, (28), -.
43. Lackner, K. S., Comment on "Efficient photochemical water splitting by a chemically modified n-TiO₂" - (III). *Science* **2003**, 301, (5640), -.
44. Jongh, P. E. d.; Vanmaekelbergh, D., Trap-Limited Electronic Transport in Assemblies of Nanometer-Sized TiO₂ Particles. *Phys. Rev. Lett* **1996**, 77, (16), 3427-3430.

45. Zaban, A.; Greenshtein, M.; Bisquert, J., Determination of the electron lifetime in nanocrystalline dye solar cells by open-circuit voltage decay measurements. *Chemphyschem* **2003**, 4, (8), 859-864.

Chapter 5:

Impact of Different Electrolytes on Photocatalytic Water Splitting

The results presented here were published in:

Impact of Different Electrolytes on Photocatalytic Water Splitting, Samuel Crawford, Elijah Thimsen and Pratim Biswas. *Journal of the Electrochemical Society* **2009**, 156, (5), H346-H351.

5.1 Abstract

Despite extensive research in photocatalytic water splitting, electrolyte usage varies greatly across different photocells. Photocatalytic water splitting continues to be performed in a wide range of electrolytes, from very acidic to very basic, with incomplete understanding of how the electrolyte composition affects performance. This study provides guidelines for electrolyte selection in water splitting applications. To determine properties that comprise an ideal electrolyte for photocatalytic electrolysis, the effects of several parameters were studied: pH, dissolved oxygen, conductivity, and composition. The photoactive anode was a nanostructured thin TiO₂ film synthesized by a flame aerosol process. The photocatalytic conversion efficiency increased with both pH and conductivity, but changes in dissolved oxygen levels had no discernable effect. The electrolyte composition was adjusted using selected salts and bases. Although the effect of the cation was negligible, anions were found to reduce efficiencies if their oxidation potential makes them thermodynamically favored over water molecules for oxidation. The results of these studies were applied in an analysis of the prospects for splitting seawater to produce hydrogen.

5.2 Introduction

Photocatalytic water splitting is a promising candidate for the clean, renewable, and cost-effective production of hydrogen. This pathway was originally demonstrated in the 1970's by Fujishima and Honda¹, then ignored for awhile after the end of the energy crisis, but has gained substantial focus in recent years. One of the most commonly studied photocatalysts for this method is TiO₂. This material is promising for many reasons. Most importantly, it has suitable conduction and valence band positions to catalyze the water-splitting reaction². However, TiO₂ does have one major drawback – it is a wide gap semiconductor ($E_g \sim 3.2$ eV) that can only absorb 4 % of the energy in sunlight³. This limitation can be partially overcome by doping⁴, but increasing the visible light response remains an active area of research. Despite this absorption limitation, pristine TiO₂ remains an excellent model photocatalyst to study surface reactions. In addition, the resources for TiO₂ are abundant and relatively cheap, and the compound is highly stable⁵, which also make it an attractive system to study.

Most research in photocatalytic oxidation has been material-based⁶⁻¹³. Few have looked into the effects of the electrolytic environment on photocatalytic efficiency, and those studies generally focused on photocatalytic oxidative pollutant degradation¹⁴⁻¹⁶. Those who investigated the effect of dissolved oxygen found system based results. In some studies, it reduced the overall efficiency of photocatalytic oxidation¹⁴, in others improved it¹⁷, or had no significant effect¹⁵. Some researchers have looked at the effect of pH and found that electrolytes at high pH are more effective in promoting photocatalytic oxidation^{15, 16}. Authors have noted, as well, that a change in pH shifts the valence band and conduction band edges of the material^{2, 15, 18}. However, the causes of

these effects have not been analyzed in detail. In addition, studies have not been carried out for the photocatalytic water splitting reaction.

This study focuses on the effect of electrolyte composition on photocatalytic splitting of water, developing a fundamental understanding of the role of ionic species in the reaction. The role of ionic species in determining photocatalytic water splitting performance is discussed in terms of their role in reaction kinetics and thermodynamics, as well as their influence on charge transport in the photoelectrochemical cell. To determine these roles and effects, four electrolyte properties were examined for their impact on the hydrogen evolution rate: (1) pH, (2) dissolved oxygen, (3) electrolyte conductivity, and (4) electrolyte composition. In addition to looking at these properties' individual effects, this paper analyzes how they overlap, which factors dominate, and which considerations are most important in selecting an electrolyte for this application. Furthermore, it examines how these findings affect the prospects for seawater splitting. Seawater provides an abundant resource for industrial-scale photoelectrolysis, and the results of this study elucidate some issues that must be addressed in order for the practicability of seawater splitting to be properly evaluated.

5.3 Experimental Methods

5.3.1 Materials

The experimental setup is illustrated in Figure 5-1. The reaction cell contains 400 mL of electrolyte and a small amount of headspace for gas flow. The cell body is composed of optical grade quartz glass with a stainless steel top bearing all ports,

including a gas inlet, outlet, and a port for each electrode. All connections were made gas-tight so that the environment could be strictly controlled.

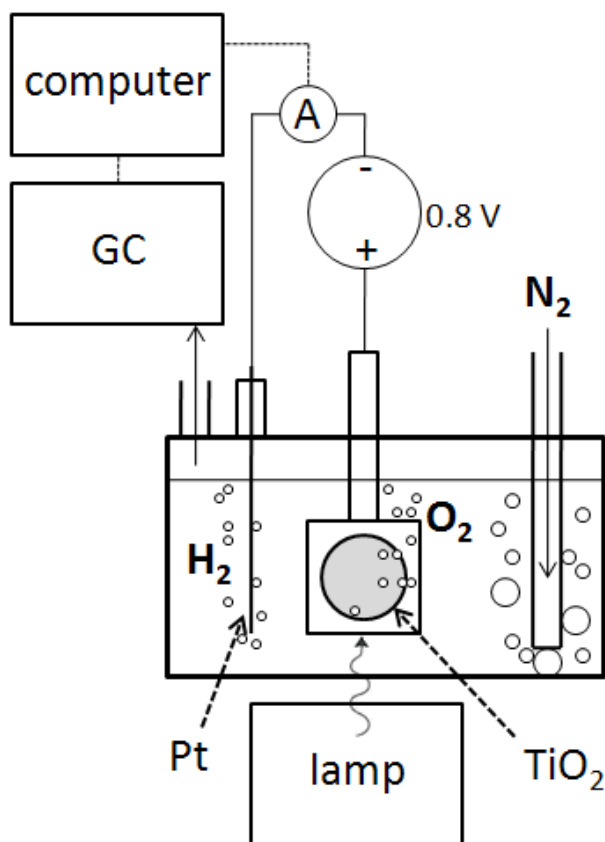


Figure 5-1. Schematic diagram of the experimental setup for water splitting.

The photocatalytic anode used in all experiments was a nanostructured TiO₂ thin film deposited on an ITO-coated glass substrate (Delta technologies, Stillwater MN). The TiO₂ film was synthesized by a premixed flame aerosol reactor (FLAR), the details of which are described in our earlier papers^{5, 19}. The flow rates of process gases were: Ar = 12.0 liter per minute at standard temperature and pressure (lpm), O₂ = 8.0 lpm, CH₄ = 2.2 lpm. The feed rate of the titanium precursor (87% titanium tetra-isopropoxide, Sigma Aldrich) was controlled by feeding 1.0 lpm of Ar through a homemade bubbler maintained at 43 °C. The burner-substrate distance was 1.5 cm. The measured substrate temperature was 212 °C, which corresponded to an approximate surface temperature of

600 °C. The film consisted of single-crystal TiO₂ columnar nanorods oriented normal to the substrate¹⁹. The crystal phase was anatase with an average grain size of 100 nm, as measured by X-ray diffraction. The nanorods were approximately 1 μm in thickness and 100 nm in width, as measured by side-view scanning electron microscope (SEM) images. The macroscopic area of the film on the substrate was 1.3 cm². A platinum wire (Bioanalytical Systems, MW-1032) was used as the counter electrode.

5.3.2 Data Collection

The entire film was illuminated with a columnated beam from an Oriel 66021 UV Lamp with a UV light intensity of 40 mW cm⁻² at the surface of the film. The irradiance was measured by a spectroradiometer (RPS900-R, International Light, Peabody MA) and was not corrected for losses at the cell walls. A bias of 0.8 V was applied using a Hewlett Packard E363-A power supply. Current was measured with a Keithley 6485 Picoammeter. The current data was acquired using a Keithley KUSB-488A GPIB data acquisition card and Keithley Excel-Linx software.

The accuracy of the current measurements was confirmed in selected experiments using gas chromatography to ensure that the measured current corresponded to hydrogen production. The effluent gas from the cell was analyzed using an Agilent 6895N Gas Chromatograph (GC). The GC signal was calibrated by blending two gas streams – hydrogen standard at 2000 ppm (balance nitrogen) and pure nitrogen – and feeding them through the reaction cell. The stream was fed directly from the cell to an automatic gas sampling valve in the GC. Nitrogen was used as the carrier gas in both the reaction cell and the GC. The sample was fed through a Supelco Carboxen 1010 PLOT column and analyzed using a thermal conductivity detector (TCD).

5.3.3 Electrolytes

The electrolytes were created by adding various amounts of NaOH (97+% ACS, Sigma-Aldrich), NaCl (99+% ACS, Sigma-Aldrich), HCl (37%, Fisher), KOH (85+% ACS, Sigma-Aldrich), KCl (99.7%, Fisher) and KI (99.6%, Mallinckrodt) to 400 mL of deionized water (Millipore). The conductivity of each solution was measured using a Thermoelectron Orion 162A conductivity probe. Measurements were carried out primarily at basic pH values. Acidic conditions were rarely used for several reasons. First, there is a possible risk of damage to the photocatalyst at low pH³. Furthermore, high pH was of greater interest, because the photocurrent was higher under basic conditions.

5.3.4 Procedure

Before each experiment, an inert nitrogen atmosphere was created by bubbling nitrogen gas through the electrolyte. The flow of nitrogen through the cell was controlled by a mass flow controller (MKS instruments). After purging the atmosphere with nitrogen at a flow rate of 200 cm³ min⁻¹ for 10 minutes, the flow rate was reduced to 20 cm³ min⁻¹. In addition to removing dissolved oxygen and carbon dioxide from solution, the flowing gas allowed the effluent to be analyzed with the GC using an automated gas sampling valve, which yielded more reproducible results than syringe samples.

The film was then irradiated for 5 minutes, and the steady state current was determined. During GC analysis, the film was irradiated for approximately 1 hour until the GC signal reached steady state.

The effects of the following electrolyte parameters were investigated: (1) pH, (2) dissolved oxygen, (3) conductivity, and (4) composition. Table 1 provides an outline of

the experimental parameters in each set of experiments. The pH was varied between 3 and 14, controlled through the addition of various strong bases (NaOH and KOH) and acids (HCl). The reaction cell was not equipped for in situ pH measurement, so reported values are based on the assumption that all dissolved carbon dioxide was purged from solution. Thus the electrolytes could be assumed to contain only deionized water, protons, hydroxide ions, and any added salts, bases, or acids. Slight deviations from reported pH values may be present in the case of 0 M and 1 M NaOH. Dissolved oxygen levels were controlled by adjusting the oxygen content in the reaction cell carrier gas. Experiments were performed with pure nitrogen carrier gas and pure oxygen carrier gas. Conductivity was controlled through the addition of bases and salts. In general, NaOH was used as the base and NaCl as the salt. However, for the experiments on electrolyte composition, KOH, KCl and KI were used to examine the effect of the cation and anion on the water splitting reaction. In this method, the roles of the cation and anion species were studied independently.

Table 5-1. Experimental outline.

Set	Parameter	Salt	Acid / Base	Purge Gas	pH
I	[OH ⁻]	NaCl (0.0-0.5 M)	NaOH (0.0-1.0 M)	N ₂	7-14
		NaCl (0.5 M)	HCl (10 ⁻⁴ -10 ⁻³ M)	N ₂	3-4
II	Conductivity	NaCl (0.0-0.5 M)	NaOH (0.0-1.0 M)	N ₂	7-14
III	Dissolved Oxygen	-	NaOH (1 M)	N ₂	14
		-	NaOH (1 M)	O ₂	14
IV	Cation / Anion Species	-	NaOH (0.0-1.0 M)	N ₂	7-14
		NaCl (0.5 M)	NaOH (0.0-1.0 M)	N ₂	7-14
		-	KOH (0.01 M, 1.0 M)	N ₂	12,14
		KCl (0.0-0.5 M)	KOH (0.0-1.0 M)	N ₂	7, 12, 14
		KI (0.5 M)	KOH (0.0-1.0 M)	N ₂	7, 12, 14

5.4 Results and Discussion

5.4.1 Effect of OH

While others^{15, 16} have researched the effect of pH on photocatalytic oxidation, this study focuses specifically on water splitting and conducts a more systematic investigation of desirable electrolyte properties. Most notably, this study concurrently investigates the effect of electrolyte composition and concentration on photocurrent, which are discussed further in subsequent sections.

The trend of photocurrent with pH was studied at various concentrations of NaCl (0 M, 0.005 M, 0.05 M, and 0.5 M) in previously deionized water. The pH of the electrolyte was controlled by adding NaOH (for basic electrolytes) or HCl (for acidic electrolytes). GC analysis was used, in some cases, to confirm that the photocurrent readings corresponded to hydrogen production. The GC analysis was performed with 0.5 M NaCl at pH 7, 0.5 M NaCl at pH 14, and salt-free electrolyte at pH 14. All GC experiments confirmed that the photocurrent readings corresponded to hydrogen production.

The data in Figure 5-2, which illustrates the hydrogen production rate as a function of pH for various concentrations of NaCl, indicate that high pH substantially improves the photocatalytic hydrogen production rate. With 0.5 M NaCl, the photocurrent is nearly 4 times greater at pH 14 than it is at pH 10. The effect of increasing pH is strongest between pH 11 and pH 13, meaning that the photocurrent increases most rapidly with the addition of hydroxide ions in that pH region. After pH 13, this effect begins to diminish, but photocurrent still increases with pH through pH 14. Below pH 10, however, the concentration of hydroxide ions has little impact on the

photocurrent. These results are similar to those found by others in the investigation of photocatalytic oxidative pollutant degradation.^{16,17}

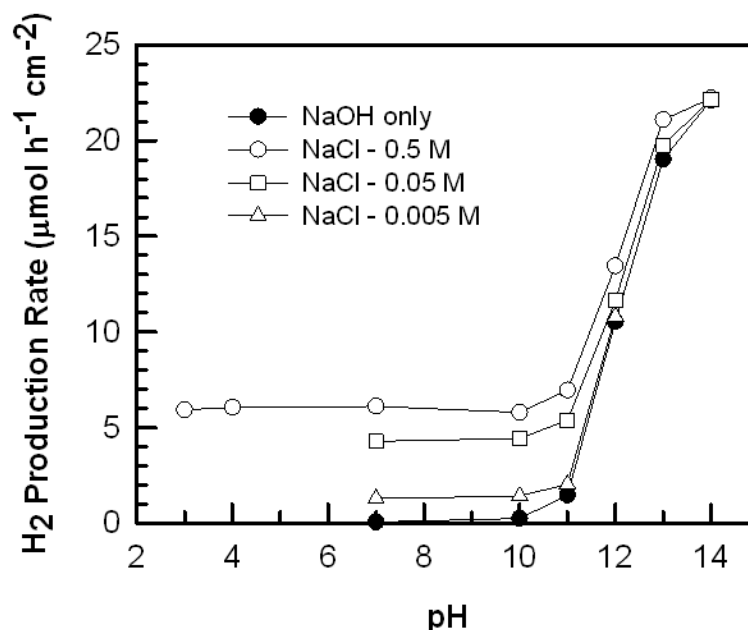


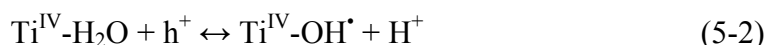
Figure 5-2. Hydrogen production rate as a function of pH. The pH was controlled in all cases by NaOH except acidic conditions in which HCl used.

Nakamura and Nakato have proposed mechanisms for oxygen evolution from water on rutile TiO₂ surfaces.²⁰ At low pH, the proposed initiation step is the simultaneous attack of a Ti-O-Ti site by a water molecule and a hole to produce neighboring Ti-O and Ti-OH.²⁰ While at high pH, the critical intermediate is neighboring Ti-O and Ti-O groups.²⁰ There are multiple proposed pathways in which these species may subsequently react to evolve oxygen. While these steps provide insight into the oxygen evolution reactions once radicals are formed, the initiation mechanism does not account for the effect of pH witnessed in this study. This motivates the development of an alternative to the “nucleophilic attack” and “surface-OH photooxidation” models.

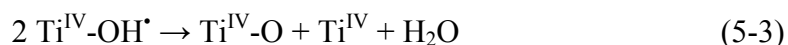
The effect of pH can be understood in terms of surface reactions on the TiO₂ film. Below a proposed reaction scheme is presented for the pathways believed to be dominant under the conditions tested. One pathway is the oxidation of water molecules. First, a water molecule adsorbs to the TiO₂ surface.



Then a hole is trapped, a hydroxyl radical formed, and a proton released.



Then radicals react in two irreversible steps to form water and oxygen.



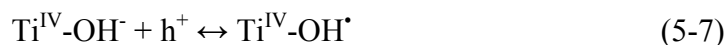
The net oxidation reaction consumes water to produce protons (which are subsequently reduced at the cathode) and oxygen gas.



Another pathway is the oxidation of hydroxide ions. First, a hydroxide ion adsorbs to the surface.

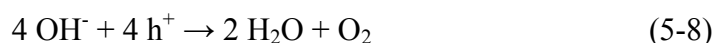


Then a hole is trapped and a hydroxyl radical formed.



The radical reactions are identical to those in water oxidation (reactions (5-3) and (5-4)).

The net oxidation reaction consumes hydroxide ions to produce oxygen gas and water.

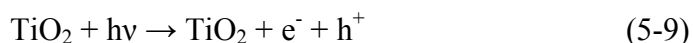


The oxidation mechanisms in each pathway are very similar. Both water molecules and hydroxide ions adsorb to the TiO₂ surface. These adsorbed species trap

holes and form adsorbed hydroxyl radicals that react irreversibly in two steps to form oxygen. The radical reactions to evolve oxygen gas are identical in both pathways. The two reactions that differ between the two oxidation pathways are the adsorption and hole trapping reactions. When considering just adsorbed species, the difference is the hole trapping mechanism.

The photocurrent is greater at higher pH, and therefore oxygen evolves more rapidly. Also, the number of adsorption sites occupied by hydroxide ions increases with pH until saturation^{21, 22}. Therefore, hydroxide ions must evolve oxygen quicker than water molecules. Because the step that differentiates the oxygen evolution mechanisms of adsorbed hydroxide ions and water molecules is the hole trapping step, hydroxide ions must trap holes more efficiently than water molecules. This is reasonable, considering that the electrostatic interaction between a negative hydroxide ion and positive hole is much greater than that between a neutral water molecule and positive hole.

The net reaction that occurs in both cases is water splitting. Hydrogen evolution driven by oxidation of water molecules contains three main steps: (1) photon adsorption to create electron-hole pairs,



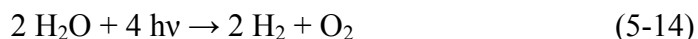
(2) anodic oxidation to form oxygen gas (reaction (5-5)), and (3) cathodic reduction to form hydrogen gas. The reactions on the platinum surface are described below.



The net half-reaction at the platinum cathode is the evolution of hydrogen through the consumption of protons, which are produced during anodic oxidation.



The overall net reaction in the photocell is water splitting.



Hydrogen evolution from oxidation of hydroxide ions differs from the first pathway in two ways. First, the anodic oxidation step is different (reaction (5-8)), which consumes hydroxide ions rather than water. Second, the consumption of water occurs through an extra step – water dissociation.



To maintain equilibrium and satisfy charge neutrality, water molecules must dissociate as protons and hydroxide ions are consumed in the production of hydrogen and oxygen. Thus the net reaction in the system is the same (reaction (5-14)), and water splitting still occurs. Therefore, hydroxide ions act as a catalyst for the photocatalytic water splitting reaction.

In summary, two pathways can lead to water splitting. Under neutral and acidic conditions, the water adsorption pathway dominates. As the solution becomes more basic, the hydroxide pathway becomes more prevalent. Because the hydroxide pathway evolves oxygen more rapidly, the rate of photocatalytic oxidation increases with the increased hydroxide concentration at higher pH.

5.4.2 Effect of Dissolved Oxygen

In previous research, dissolved oxygen has been found to either inhibit photocatalytic oxidation¹⁴, promote it¹⁷, or have no significant effect¹⁵. While these referenced studies also used TiO₂ for the photoactive component, the application was not water splitting. In this study, adjustment of dissolved oxygen levels was found to have no observable impact on the photocurrent. However, it seems reasonable that dissolved oxygen would have a negative impact, considering dissolved oxygen's role at the surface.

The dissolved oxygen levels were controlled by adjusting the oxygen content in the reaction cell carrier gas. The photocurrent was tested under two different atmospheres – one oxygen-rich and one oxygen-starved. A 1 M NaOH solution was used as the electrolyte in both cases. First, oxygen was purged from the system using pure nitrogen, and the photocurrent was tested under this pure nitrogen atmosphere. Second, pure oxygen was used to purge the nitrogen from the cell, and the photocurrent was measured under a pure oxygen atmosphere. Dissolved oxygen was found to have no discernable effect on the photocatalytic conversion efficiency. The photocurrents of the oxygen-rich and oxygen-starved atmospheres were negligibly different, indicating a minimal impact of dissolved oxygen on this system.

Although these experiments found no effect of dissolved oxygen on the photocurrent, it is reasonable that dissolved oxygen would inhibit – rather than promote – photocatalytic oxidation, considering oxygen's role at the TiO₂ surface. Oxygen can adsorb to the surface and trap electrons. While electron trapping prevents recombination of electron-hole pairs (potentially improving photo-oxidation¹⁷), it also keeps electrons static rather than allowing them to flow freely through the external circuit in order to

reduce protons at the cathode. Additionally, by trapping electrons, oxygen occupies surface sites that could possibly be held by water molecules or hydroxide ions, both of which trap holes (thereby preventing recombination) and participate in subsequent reactions which lead to the evolution of oxygen. Thus, while adsorbed oxygen may help prevent recombination, it occupies surface sites that could be held by molecules that are more effective in promoting oxygen evolution, which consumes holes and frees electrons. Thus, in two-electrode systems such as the present photocell, oxygen may deactivate surface sites and inhibit photocatalysis. Furthermore, although dissolved oxygen had no significant impact on the photoanode in this study, it is possible that the oxygen could have been reduced at the platinum surface to react with protons and produce H_2O_2 – instead of H_2 – without changing the photocurrent, an effect that would also be undesirable.

5.4.3 Effect of Conductivity

Solutions were prepared with 0.0-0.5 M NaCl and 0.0-1.0 M NaOH in order to study the effect of conductivity and its impact relative to pH. The photocurrent increased with conductivity. In electrochemical surface reactions, diffusion plays a large role. Anions diffuse to the surface and form intermediates that diffuse across the surface to form products that diffuse away from the surface. Diffusion is facilitated by increasing conductance. The more conductive the solution, the more effectively charge can be transported through the solution, including the shuttling of ions to and from electrode surfaces²³.

Figure 5-3 illustrates the extent of conductivity's effect and how it compares with the effect of pH. The increased photocurrent due to additional conductivity from bases is always greater than or equal to that from salts, because bases increase the pH in addition to increasing conductivity. In Figure 5-3, the salt-free (dashed) curve is the minimum conductivity at a given pH using NaOH as the base. The solid curves extending from the dashed curve each correspond to increasing conductivity at a given pH, controlled through the addition of NaCl. At each pH, the hydrogen production rate increased with conductivity. The effect of increasing conductivity is greatest from about $10^3 - 10^4 \mu\text{S cm}^{-1}$ ($0.005 \text{ M} - 0.05 \text{ M NaCl}$). Although the extent of the effect begins to diminish above that region, photocurrent increased with conductivity throughout the investigated range.

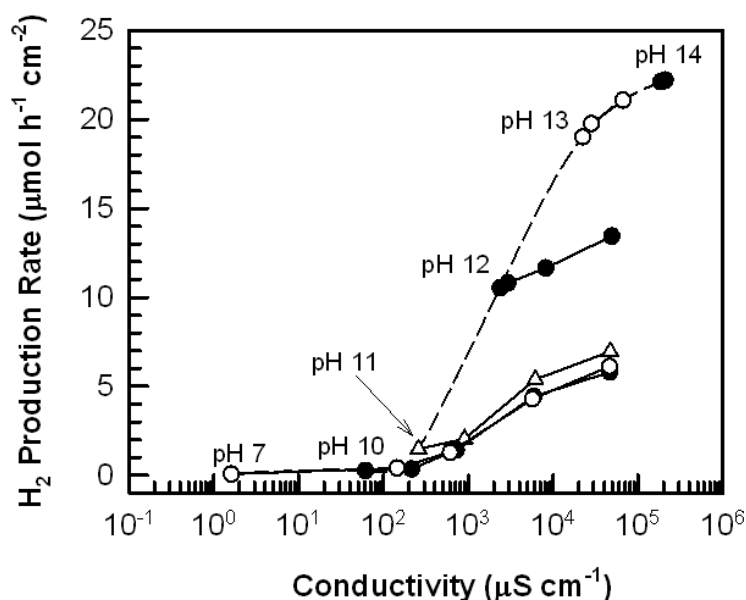


Figure 5-3. Hydrogen production rate as a function of conductivity. The dashed curve represents salt-free electrolytes containing only NaOH and corresponds to the minimum conductivity at a given pH. The curves extending from the dashed curve are at constant pH, and the conductivity increase corresponds to an increasing concentration of NaCl, which ranges from 0.0-0.5 M.

At high pH, it appears that the effect of additional conductivity from NaCl is equal to that from NaOH, as the pH 13 curve in Figure 5-3 coincides with the dashed NaOH curve. Thus, above pH 13, the effect of increased current with pH seems to be due mostly to increased conductivity rather than the increased hydroxide ion concentration. This indicates that, by pH 13, the TiO₂ surface has become saturated with hydroxide ions. Therefore it may be unnecessary to operate at the highest pH possible (thus an extremely caustic environment) in order to achieve the greatest photocurrent. Instead, one can use a basic electrolyte to set the pH at 13 and then use cheaper, neutral electrolytes to increase the photocurrent by increasing the conductivity.

5.4.4 Effect of Cation and Anion Species

Researchers investigating photocatalytic oxidation in water have used a variety of electrolytes, including H₂SO₄⁹⁻¹¹, KNO₃²⁴, NaCl¹⁴, Sodium Acetate²⁵, H₃PO₄^{12, 26}, NaClO₄¹³, and KOH¹⁹. However, there has been little comparison between different electrolytes. While all these studies had functional systems that produced photocurrents, it is possible that better electrolyte selection could have substantially improved reported efficiencies. In the sections above, it has been shown that bases increase the photocurrent by increasing the concentration of hydroxide ions at the TiO₂ surface, and salts can also increase the photocurrent by increasing conductivity. This section analyzes which specific salts and bases are preferable by investigating the effect of the identity of the cation and anion species on the water splitting rate. In order to avoid undesirable oxidation pathways, the oxidation potential of the anion is the most important factor to consider for an electrolyte.

To investigate the effect of the cation, solutions of KOH were made at pH 12 and 14, and solutions of 0.5 M KCl were made at pH 7, 12, and 14 (set by KOH). These solutions all had the same ion concentrations as solutions in previous experiments, with the only change being the replacement of Na^+ with K^+ . As shown in Figure 5-4, this change yielded negligible differences in the photocurrent.

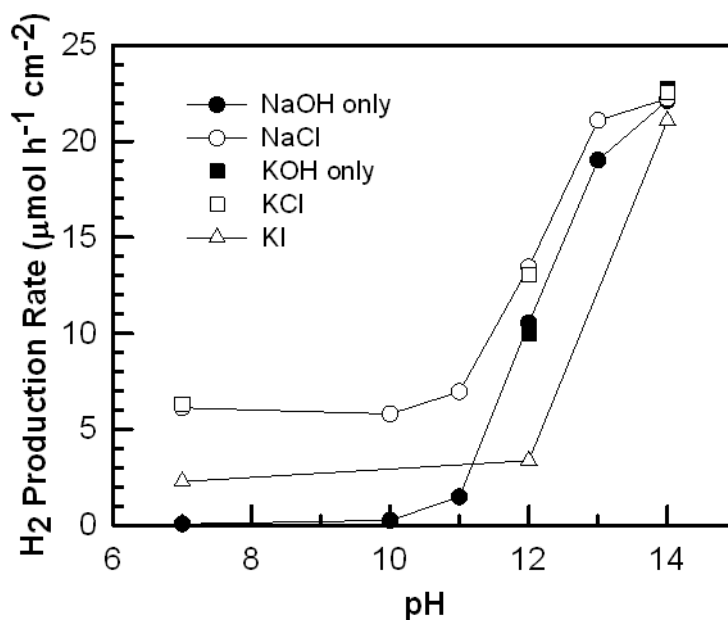
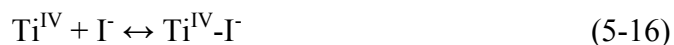


Figure 5-4. Hydrogen production rate as a function of pH for multiple electrolytes. All salts were at a concentration of 0.5 M. Base was added in varying concentrations to increase the pH. Only one cation was used in each solution. For NaCl, NaOH was used as the base. For KCl and KI, KOH was used as the base.

To investigate the effect of anion species, KCl was replaced by KI. Solutions of 0.5 M KI were made with pH values of 7, 12, and 14 (set by KOH). During illumination, the solutions developed a slight yellow discoloration over time. This indicated that iodide ions from the salt were being oxidized to I_2 . Thus the presence of iodide in solution opens up a third oxidation pathway at the anode, in addition to water oxidation and hydroxide oxidation.

The reactions in the iodide oxidation pathway are as follows. This analysis assumes iodide is the species involved in the surface reaction, although other species could be involved as well. First, an iodide ion adsorbs to the TiO₂ surface.



Then a hole is trapped and an iodine radical formed.



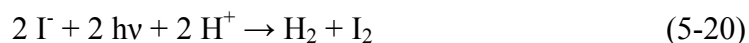
Then radicals react in a single irreversible step to form iodine.



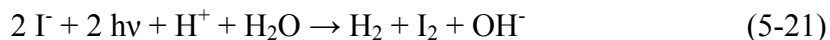
The net oxidation reaction consumes iodide ions to produce iodine.



Combining this reaction with photon adsorption and hydrogen evolution, the net reaction is the consumption of protons and iodide ions to produce elemental hydrogen and iodine.



To preserve equilibrium, water may dissociate to regenerate protons and form hydroxide ions. At pH 7, a water molecule will dissociate (reaction (5-15)) once every other time that a proton is consumed. The net system reaction, with dissociation included, produces hydroxide ions and makes the solution more basic.



The KI solutions produced substantially lower photocurrents than respective KCl solutions due to the oxidation of iodide, which is thermodynamically favored over the oxidation of water (see Figure 5-5). While standard reduction potentials are used here, the effect of pH on the energy levels is discussed in Appendix II. The standard reduction potential for water, shown below, is 1.23 V/NHE.



The standard reduction potential for iodine is 0.54 V/NHE, less than that of water.



Although iodide is thermodynamically favored over water for oxidation, water is favored over chloride. The standard reduction potential of chlorine is 1.33 V/NHE.



The reduced photocurrent during iodide oxidation could be the result of two causes. First, the iodide oxidation mechanism could be slower than the water oxidation mechanism, making the kinetics unfavorable despite favorable thermodynamics. If this is true, the step that slows down oxidation must be the radical reaction. As stated previously, hydroxide ions scavenge holes faster than water because of an electrostatic attraction between the positive hole and negative ion. Because iodide is negatively charged, it has a similar attraction to the hole and should also scavenge holes faster than neutral water molecules. However, it still produces less photocurrent than water does, so the radical reaction must be slower for iodine radicals than hydroxyl radicals.

Second, the presence of iodide may deactivate the surface by reducing the likelihood of reaction and increasing the probability of trapped holes escaping. With just water and hydroxide ions present, the only adsorbed radicals formed at the TiO_2 surface are hydroxyl radicals. Therefore, the probability of two radicals finding one another and reacting is relatively high. In the presence of iodide ions in solution, the surface becomes covered by iodine radicals as well, decreasing the probability of two hydroxyl radicals reacting.

Even in the presence of iodide, the current increases with pH, indicating that hydroxide oxidation still increases with pH. The standard reduction potential of hydroxide formation is 0.40 V/NHE, which means that hydroxide oxidation is thermodynamically more favorable than iodide oxidation.



Hydroxide oxidation dominates at high pH, as evidenced by the elevated photocurrent. Because hydroxide oxidation does not dominate at pH 7 (10^{-7} M OH⁻), despite its thermodynamic favor, iodide oxidation must dominate because of its occupation of more surface sites as a result of its higher concentration. Therefore, anodic oxidation must be determined by both electrode potential thermodynamics and competition for surface site adsorption.

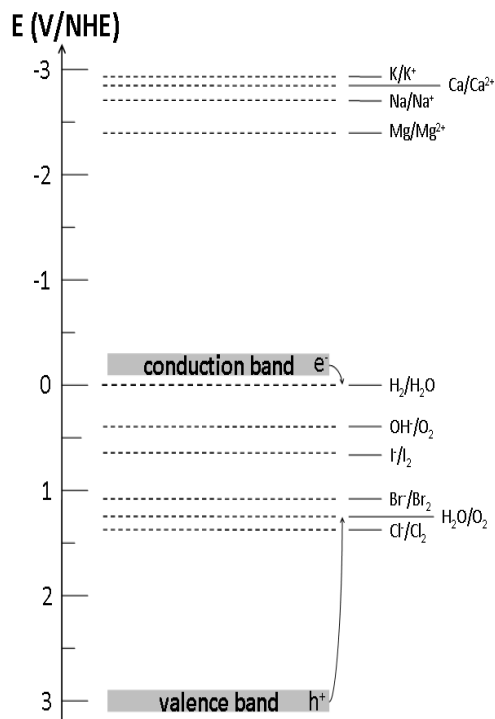


Figure 5-5. Energy level diagram indicating the valence and conduction band energy levels for TiO₂ relative to certain standard reduction potentials²⁸. Excited electrons move down from the conduction band to reduce, while holes move up from the valence band to oxidize.

The relative standard reduction potentials of the half-reactions also explain why the effect of the cation identity is negligible. Protons are reduced at the cathode because of their strong thermodynamic favor. The standard reduction potential for proton reduction to hydrogen gas is 0.00 V/NHE, as it is defined as the reference potential for all other half-reactions.



The standard reduction potential for sodium ion reduction to solid sodium is -2.71 V/NHE, which is substantially more negative.



The standard reduction potential for potassium ion reduction to solid potassium is even more negative, -2.93 V/NHE.



Because the potential of proton reduction is more positive than that of either metal ion, proton reduction is substantially more thermodynamically favorable. Moreover, K^+ and Na^+ reduction are at a more negative reduction potential than the TiO_2 conduction band (see Figure 5-5). Because electrons only move downward from the conduction band²⁷, proton reduction is the only pathway that will occur at the cathode. Thus all of the photocurrent goes toward hydrogen production, which the GC measurements confirm.

Reduction potential of dissolved species is an important consideration for electrolytes, especially in the case of seawater splitting, as seawater is a very complex electrolyte²⁸. Bromide ions present in seawater may be oxidized to bromine (see Figure 5-5). Dissolved organics may be favored for oxidation as well. While most dissolved

species in seawater are present at low concentrations, these concentrations will increase over time as water is consumed. While this accumulation would have the positive effect of increasing the conductivity of the solution, it would also present issues with undesired oxidation (possibly reduction as well) and precipitation. Specifically, Mg^{2+} ions would consume catalytic OH^- ions to form $\text{Mg}(\text{OH})_2$. Thus some species may need to be filtered from seawater in order to prevent these issues, but minimal pretreatment is desirable economically. The results of this study have important implications for seawater splitting and indicate the need for further investigation.

5.5 Conclusions

The effects of various electrolyte parameters on photocatalytic water splitting were tested using a thin TiO_2 film, synthesized in a flame aerosol reactor, as the photoactive anode. To determine the role and impact of OH^- ions in water splitting, the pH was varied in solutions containing a variety of concentrations of NaCl. In all cases, the water splitting rate was relatively constant with pH until after pH 10, at which point performance improved with increasing pH, which was attributed to the use of a more effective water splitting pathway through the direct oxidation of OH^- ions rather than water molecules. Although dissolved oxygen was found to have a negligible impact on this system, it is likely that the decreased performance observed in photocatalytic pollutant degradation¹⁵ is due to the deactivation of surface sites. The water splitting rate increased with electrolyte conductivity due to the improved transport of ions. Beyond pH 13, it was found that the improved photocurrent from the addition of more base was due mostly to increased conductivity. Thus the impact of increased pH above this point is minimal. The cation species did not substantially affect the water splitting rate. The

anion species, however, may reduce the water splitting rate if its oxidation potential makes it thermodynamically favorable over water. This issue of anion oxidation complicates the idea of splitting seawater. Furthermore, Mg^{2+} ions can consume hydroxide ions to precipitate base. Other precipitates may present problems as well. Further investigation would help determine the extent of pretreatment necessary for efficient photoelectrolysis of seawater.

5.6 Acknowledgments

This work was supported partially by grants from the Center of Materials Innovation, the Jens Endowment and the McDonnell Academy Global Energy and Environmental Partnership (MAGEEP) at Washington University in St. Louis.

5.7 References

1. Fujishima, A.; Honda, K., Electrochemical Photolysis of Water at a Semiconductor Electrode. *Nature* **1972**, 238, 37.
2. Gratzel, M., Photoelectrochemical Cells. *Nature* **2001**, 414, 338 - 344.
3. Nowotny, J.; Sorerell, C. C.; Sheppard, L. R.; Bak, T., Solar-hydrogen: Environmentally safe fuel for the future. *International Journal of Hydrogen Energy* **2005**, 30, 521-544.
4. Ingler, W. B.; Al-Shahr, M.; Kahn, S. U. M., Efficient Photochemical Water Splitting by a Chemically Modified n-TiO₂. *Science* **2002**, 297, 2243-2245.
5. Thimsen, E.; Biswas, P., Nanostructured photoactive films synthesized by a flame aerosol reactor. *Aiche Journal* **2007**, 53, (7), 1727-1735.

6. Li, J.; Yun, H.; Lin, C. J., A photoelectrochemical study of n-doped TiO₂ nanotube arrays as the photoanodes for cathodic protection of SS. *Journal of the Electrochemical Society* **2007**, 154, (11), C631-C636.
7. Wang, H. L.; Deutsch, T.; Turner, J. A., Direct water splitting under visible light with nanostructured hematite and WO₃ photoanodes and a GaInP₂ photocathode. *Journal of the Electrochemical Society* **2008**, 155, (5), F91-F96.
8. Bae, E.; Choi, W., Effect of the anchoring group (carboxylate vs phosphonate) in Ru-complex-sensitized TiO₂ on hydrogen production under visible light. *Journal of Physical Chemistry B* **2006**, 110, (30), 14792-14799.
9. Baeck, S. H.; Choi, K. S.; Jaramillo, T. F.; Stucky, G. D.; McFarland, E. W., Enhancement of photocatalytic and electrochromic properties of electrochemically fabricated mesoporous WO₃ thin films. *Advanced Materials* **2003**, 15, (15), 1269-+.
10. Greeley, J.; Jaramillo, T. F.; Bonde, J.; Chorkendorff, I. B.; Norskov, J. K., Computational high-throughput screening of electrocatalytic materials for hydrogen evolution. *Nature Materials* **2006**, 5, (11), 909-913.
11. Ingler, W. B.; Khan, S. U. M., A self-driven p/n-Fe₂O₃ tandem photoelectrochemical cell for water splitting. *Electrochemical and Solid State Letters* **2006**, 9, (4), G144-G146.
12. Miller, E. L.; Marsen, B.; Paluselli, D.; Rocheleau, R., Optimization of hybrid photoelectrodes for solar water-splitting. *Electrochemical and Solid State Letters* **2005**, 8, (5), A247-A249.

13. Su, Y. F.; Chou, T. C.; Ling, T. R.; Sun, C. C., Photocurrent performance and nanostructure analysis of TiO₂/ITO electrodes prepared using reactive sputtering. *Journal of the Electrochemical Society* **2004**, 151, (9), A1375-A1382.
14. Belghazi, A.; Bohm, S.; Worsley, D. A.; McMurray, H. N., Photoelectrochemically driven charge transport across free standing TiO₂ pigmented organic polymer films. *Zeitschrift Fur Physikalische Chemie-International Journal of Research in Physical Chemistry & Chemical Physics* **2005**, 219, (11), 1539-1546.
15. Zhang, S. Q.; Zhao, H. J.; Jiang, D. L.; John, R., Photoelectrochemical determination of chemical oxygen demand based on an exhaustive degradation model in a thin-layer cell. *Analytica Chimica Acta* **2004**, 514, (1), 89-97.
16. Zhao, H. J.; Jiang, D. L.; Zhang, S. Q.; Catterall, K.; John, R., Development of a direct photoelectrochemical method for determination of chemical oxygen demand. *Analytical Chemistry* **2004**, 76, (1), 155-160.
17. Almquist, C. B.; Biswas, P., A mechanistic approach to modeling the effect of dissolved oxygen in photo-oxidation reactions on titanium dioxide in aqueous systems. *Chemical Engineering Science* **2001**, 56, (11), 3421-3430.
18. Hameed, A.; Gondal, M. A.; Yamani, Z. H., Effect of transition metal doping on photocatalytic activity of WO₃ for water splitting under laser illumination: role of 3d-orbitals. *Catalysis Communications* **2004**, 5, (11), 715-719.
19. Thimsen, E.; Rastgar, N.; Biswas, P., Nanostructured TiO₂ films with controlled morphology synthesized in a single step process: Performance of dye-sensitized solar cells and photo watersplitting. *Journal of Physical Chemistry C* **2008**, 112, (11), 4134-4140.

20. Nakamura, R.; Nakato, Y., Primary intermediates of oxygen photoevolution reaction on TiO₂ (rutile) particles, revealed by in situ FTIR absorption and photoluminescence measurements. *Journal of the American Chemical Society* **2004**, 126, (4), 1290-1298.
21. Sugimoto, T.; Zhou, X. P., Synthesis of uniform anatase TiO₂ nanoparticles by the gel-sol method - 2. Adsorption of OH⁻ ions to Ti(OH)₄ gel and TiO₂ particles. *Journal of Colloid and Interface Science* **2002**, 252, (2), 347-353.
22. Chan, H. Y. H.; Takoudis, C. G.; Weaver, M. J., Oxide film formation and oxygen adsorption on copper in aqueous media as probed by surface-enhanced Raman spectroscopy. *Journal of Physical Chemistry B* **1999**, 103, (2), 357-365.
23. Cussler, E. L., *Diffusion, mass transfer in fluid systems*. Cambridge University Press: Cambridge ; New York, 1984; p xii, 525 p.
24. Jaramillo, T. F.; Baeck, S. H.; Kleiman-Shwarsstein, A.; Choi, K. S.; Stucky, G. D.; McFarland, E. W., Automated electrochemical synthesis and photoelectrochemical characterization of Zn_{1-x}CoxO thin films for solar hydrogen production. *Journal of Combinatorial Chemistry* **2005**, 7, (2), 264-271.
25. Baeck, S. H.; Jaramillo, T. F.; Kleiman-Shwarsstein, A.; McFarland, E. W., Automated electrochemical synthesis and characterization of TiO₂ supported Au nanoparticle electrocatalysts. *Measurement Science & Technology* **2005**, 16, (1), 54-59.
26. Miller, E. L.; Marsen, B.; Cole, B.; Lum, M., Low-temperature reactively sputtered tungsten oxide films for solar-powered water splitting applications. *Electrochemical and Solid State Letters* **2006**, 9, (7), G248-G250.

27. Gondal, M. A.; Hameed, A.; Yamani, Z. H., Laser induced photocatalytic splitting of water over WO₃ catalyst. *Energy Sources* **2005**, 27, (12), 1151-1165.
28. Lide, D. R., *Handbook of Chemistry and Physics*. 77 ed.; CRC Press: 1996.

Chapter 6:

Band Structure of Mixed Metal Oxides: Theory and Experiment

The results presented here were published in:

Predicting the Band Structure of Mixed Transition Metal Oxides: Theory and Experiment, Elijah Thimsen, Subhashis Biswas, Pratim Biswas and Cynthia Lo. *Journal of Physical Chemistry C* **2009**, 113, (5), 2014-2021.

6.1 Abstract

Fuel production from sunlight using mixed metal-oxide photocatalysts is a promising route for harvesting solar energy. While photocatalytic processes can operate with high efficiency using UV light, it remains a challenge of paramount importance to drive them with visible light. Engineering the electronic energy band structure of mixed metal-oxides through judicious control of atomic composition is a promising route to increasing visible light photoresponse. The goal of this paper is to develop a simple Mixed Metal-Oxide Band Structure (MMOBS) method to predict the electronic band structure of mixed metal-oxides. Several materials in the Ti-Fe-O system that span the composition spectrum were considered in this study: anatase TiO_2 , Fe-doped anatase TiO_2 , ilmenite TiFeO_3 , Ti-doped hematite $\alpha\text{-Fe}_2\text{O}_3$, and hematite $\alpha\text{-Fe}_2\text{O}_3$. The predictions by the MMOBS method for the Ti-Fe-O system were tested and confirmed using first-principles density functional theory (DFT) calculations and experimental UV-visible absorption spectroscopy measurements. The band gap energy of the compounds decreases with increasing Fe content until Fe and Ti are present in approximately the same concentration, and then the band gap energy remains constant and equal to that of hematite (~ 2.0 eV), independent of Ti content. The positions of the conduction and valence bands, which are critical to driving photocatalytic reactions, are also predicted using the MMOBS method. Finally, the applicability of the MMOBS method to the rational design of photocatalysts for reduction-oxidation reactions in watersplitting is discussed.

6.2 Introduction

An attractive solution to global energy challenges is the conversion of solar energy to fuels such as hydrogen¹⁻⁵. Metal-oxides are increasingly being investigated for their potential in photocatalytic fuel production due to their demonstrated ability to convert UV light to fuels, chemical stability, and low production costs. Many metal-oxide semiconductors are stable in chemically aggressive environments, particularly in oxidative environments such as the atmosphere and aqueous media, which affords them long-term stability. Furthermore, metal-oxides such as TiO_2 and Fe_2O_3 are produced in quantities of millions of tons per year. These materials are used in a variety of applications where low cost is critical due to the volume of material required, such as for house paint and building glass. Thus, it is desirable to use these low-cost, industrially-relevant materials for widespread solar energy harvesting.

The main hurdle in photocatalytic fuel production is the efficient conversion of sunlight, which primarily contains photons at visible wavelengths. Some materials have shown promising efficiencies for solar hydrogen production when driven by AM1.5G simulated sunlight, such as Fe_2O_3 (~2%)^{6, 7} and WO_3 (~4%)^{8, 9}. Unfortunately, these materials are not ideal for photocatalytic hydrogen production due to inherent limitations in their electronic structure¹⁰, so further improvements must be made. A principal challenge is to develop novel materials that can drive photocatalytic fuel production using visible light with an efficiency of over 10%, which is the level at which the United States Department of Energy (DOE) predicts the technology will be economically viable².

The conversion efficiency of metal-oxide semiconductors is highly dependent on photon absorption, which in turn is determined by the band gap of the material. Photon

absorption results in the promotion of an electron from the filled valence band to the empty conduction band. The difference in energy between these bands is the band gap, which determines the amount of sunlight a material will absorb and the maximum possible solar conversion efficiency. The material will absorb photons in the solar spectrum with energies greater than or equal to the band gap, resulting in excited electron-hole pairs available for initiating photochemistry. Most oxide semiconductors have band gap values greater than 3.0 eV, which lies in the UV portion of the spectrum. For photocatalytic hydrogen production, the optimum band gap is approximately 2.0 eV, which is small enough to absorb a significant amount of sunlight, but larger than the energy required to split a water molecule (1.23 eV)^{2, 9}. As mentioned previously, some oxides have band gap values in this range, such as Fe₂O₃ (2.2 eV) and CuO (1.7 eV). Unfortunately, these compounds have relatively low incident photon to current conversion efficiencies⁷ or experience photocorrosion¹¹. Thus, for widespread solar fuel production, there is a need to develop new materials that have a band gap more suitably matched to the solar spectrum.

Other factors controlling the photocatalytic activity of metal-oxides are the positions of the valence and conduction bands on a relative energy scale. Photocatalytic reactions can be thought of as reduction-oxidation reactions with electrons in the conduction band as the reducing species and holes in the valence band being the oxidizing species. In general, the conduction band must be at a higher energy (more negative reduction potential) than the potential of the reduction half reaction while the valence band must be at a lower energy (more positive reduction potential) than the oxidation half reaction. For instance, in order to promote the watersplitting reaction, the

conduction band edge of the photocatalyst must be at a higher energy (more negative reduction potential) than the $\text{H}_2/\text{H}_2\text{O}$ potential (0 V/NHE) while the valence band edge must be at a lower energy (more positive reduction potential) than the $\text{H}_2\text{O}/\text{O}_2$ potential (1.23 V/NHE). TiO_2 is an example of a material that meets these criteria^{2, 9}. As new materials are explored, there is a need to control the positions (oxidation and reduction potentials) of the photocatalyst valence and the conduction bands.

Much work has already been done on developing new metal-oxide based materials for photocatalytic hydrogen production. In particular, many researchers have worked with chemically-modified materials based on TiO_2 . For instance, oxygen-deficient TiO_2 , has been shown to increase the visible light photoresponse^{12, 13}. Perhaps the most common and successful route for extending the photo response of TiO_2 into the visible spectrum is the addition of small amounts (< 10 atom %) of impurities into the semiconductor. By doping TiO_2 with nonmetals such as carbon¹⁴⁻¹⁶ and nitrogen¹⁷⁻²¹, efficient photocatalytic watersplitting can be achieved using visible light. By doping with transition metals such as V^{22, 23}, Fe^{23, 24} and Cr^{25, 26}, similar enhancements in the photocatalytic performance have also been observed. Some theoretical work based on first-principles density functional theory (DFT)^{16, 17, 19, 27} calculations has also been performed to investigate changes in band structure induced upon nonmetal and transition metal doping. While the net effect varies depending on the dopant, the general consensus is that doping introduces additional energy levels (mid-gap states) into the TiO_2 band gap that lowers the energy required to excite electrons from the valence to the conduction band; this allows photoactivation by visible photons. Unfortunately, the light absorption in the visible spectrum for these doped materials still remains too low to efficiently

harvest sunlight. This has recently led researchers to begin to explore new mixed metal oxides, such as the Ti-Fe-O²⁴, Ti-Cu-O²⁸ and Ti-W-O²⁹ compounds. These mixed metal oxides show great promise for photocatalytic fuel production, compared to their basis compounds.

The current understanding of fundamental changes in electronic structure with atomic composition of metal-oxide semiconductors is insufficient to rationally design the atomic composition of new compounds. Current research remains largely combinatorial³⁰ or “guess-and-check” in nature. To guide the search, a theoretical procedure is needed to rationally predict the band gap and band positions of mixed metal-oxides. First-principles DFT calculations may aid in this task, but they are computationally expensive and time-consuming for complex chemical systems. Experimental synthesis combined with UV-visible spectroscopy and electrochemical measurements can also be used to screen potential configurations, but the procedure is again time-consuming and costly.

The objective of this paper is to develop a simple Mixed Metal Oxide Band Structure (MMOBS) procedure to predict the band gaps and band positions of mixed transition metal-oxides using catalogued band position data. The MMOBS procedure is used to predict the band structure of various Ti-Fe-O compounds with different compositions. The Ti-Fe-O system is used as a model because of its promising performance in photocatalytic watersplitting^{24, 31} and the wealth of available data from prior characterization^{10, 11, 32}. The MMOBS procedure could likely be generally extended to other mixed metal-oxides. In this study, the results of MMOBS predictions are corroborated by first-principles DFT calculations and experimental measurements on

nanostructured synthetic thin films. The use of the MMOBS procedure to design the chemical composition of mixed metal oxide semiconductors for optimum photocatalytic watersplitting performance is also discussed.

6.3 Methods

6.3.1 Test Plan

Five different oxides in the Ti-Fe-O system were studied: anatase TiO_2 , Fe-doped anatase TiO_2 , ilmenite TiFeO_3 , Ti-doped hematite $\alpha\text{-Fe}_2\text{O}_3$ and hematite $\alpha\text{-Fe}_2\text{O}_3$. These compounds span the composition spectrum, from TiO_2 to Fe_2O_3 , with different amounts of Ti and Fe. Pristine anatase TiO_2 was chosen for its robust performance in UV light-driven photocatalytic water splitting^{33, 34}. Fe-doped anatase TiO_2 was chosen for its promise in enhancing visible light absorption²⁰ and photocatalytic performance²³. Ilmenite (TiFeO_3) was chosen as the representative of a mixed metal-oxide that contains equal amounts of Ti and Fe. In addition, relatively little characterization has been performed on TiFeO_3 . Finally, Ti-doped hematite $\alpha\text{-Fe}_2\text{O}_3$ and pristine hematite $\alpha\text{-Fe}_2\text{O}_3$ were chosen for their excellent light absorption characteristics in the visible region of the spectrum, moderate watersplitting ability^{6, 7, 11, 31}, and completion of the composition series.

6.3.2 MMOBS Analysis

The prediction of the electronic structure of mixed metal-oxide compounds by the MMOBS method is based on the electronic structure of the basis compounds from which the mixed compound is formed. The basis compounds are the thermodynamically stable pristine oxides. For the Ti-Fe-O system, the basis compounds are TiO_2 and $\alpha\text{-Fe}_2\text{O}_3$

(Figure 6-1). The valence and conduction band positions for these compounds are readily available in the literature^{10, 11, 32}. The TiO₂ valence band lies at a lower energy than the Fe₂O₃ valence band, while the TiO₂ conduction band lies at a higher energy than the Fe₂O₃ conduction band (Figure 6-2).

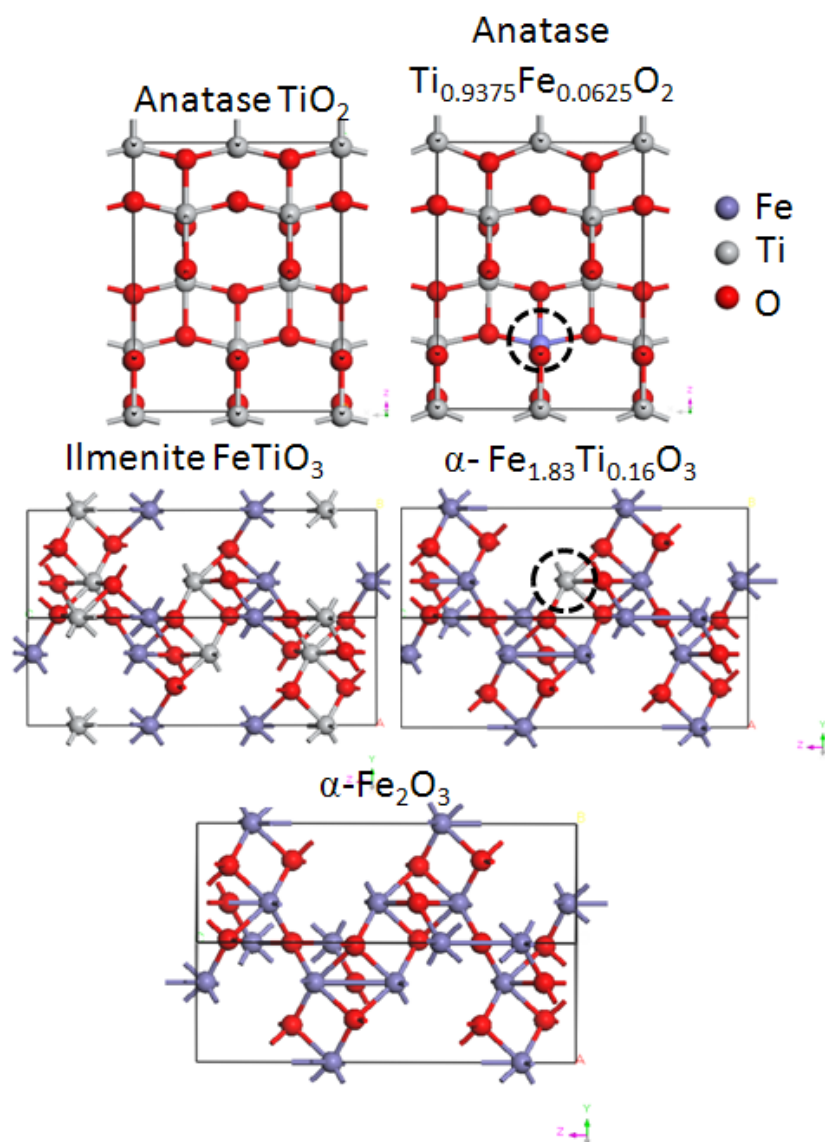


Figure 6-1: Crystal structures for the 5 model Ti-Fe-O compounds used in the DFT calculations. The pristine and Fe-doped anatase TiO₂ supercells are positioned with the [001] direction perpendicular to the page. The ilmenite and hematite crystal structures are positioned such that the c-axis points to the left and the long axis of the a-b plane is perpendicular to the page.

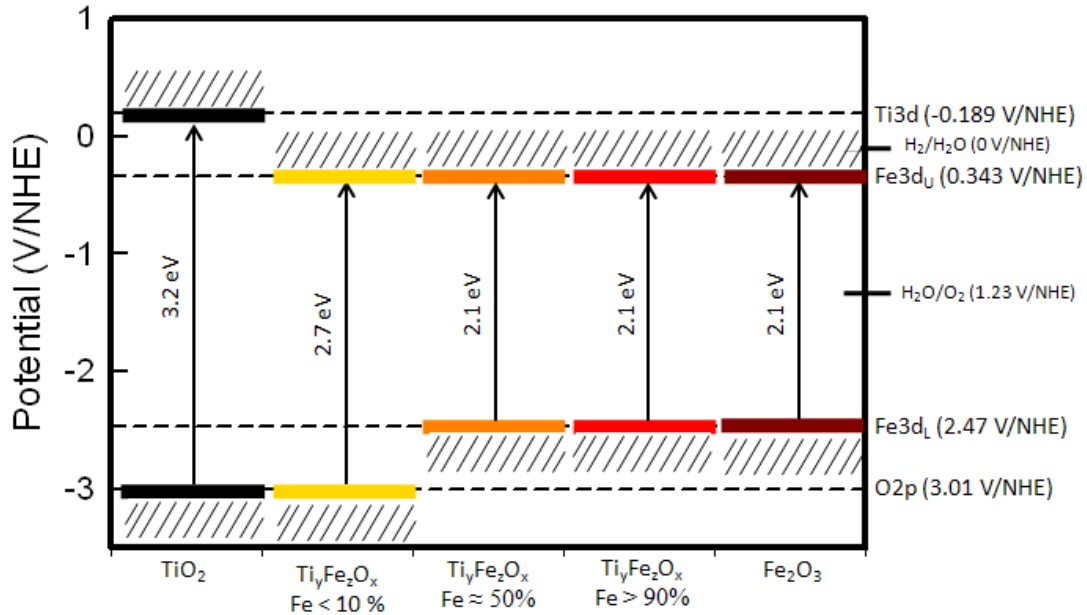


Figure 6-2: Electronic band edge positions of the Ti-Fe-O compounds determined by the MMOBS analysis using experimental basis values. The valence bands lie on the lower portion of the diagram while the conduction bands lie on the upper portion.

The electronic band structure of mixed Ti-Fe-O compounds is a combination of the energy band structures of the respective basis oxides. The energy levels in the mixed oxides have the same band positions as the respective basis pristine oxides. This analysis assumes that the bonding present in the mixed phase is nominally the same as in the pristine compounds. In other words, in the mixed phases, the Ti and Fe atoms are bonded to oxygen atoms with a similar coordination to the basis compounds. If one metal species is present at over 90 % based on metal atoms, the compound is described as doped with the metal species present in dilute concentration. The valence band in doped compounds has the same position as the valence band in the basis (majority) compound. The conduction bands have the same positions as the conduction bands of both of the respective basis compounds. Depending on the conduction band positions of the basis

compounds, the ones in doped compounds may mix, if they are close in energy, or remain isolated to form a mid-gap state, if they are sufficiently separated in energy. If both metal species are present in roughly the same concentration, then the valence bands in the mixed compound have the same band positions as the valence bands in the basis compounds; and the conduction bands in the mixed compound have the same band positions as the conduction bands in the basis compounds.

6.3.3 DFT Calculations

The electronic band structures of five Ti-Fe-O systems (listed above) were calculated using density functional theory as implemented in CASTEP³⁵. All crystal structures were taken from the American Mineralogist online database³⁶. A pseudopotential plane wave (PSPW) approach with a kinetic energy cutoff of 300 eV for the plane wave basis set was used, along with the generalized gradient approximation (GGA) of Perdew, Burke and Ernzerhof³⁷ (PBE) for the exchange-correlation functional. This approach employed periodic boundary conditions and thus modeled an infinite (bulk) crystalline system. Ultra-soft pseudopotentials³⁸ were used to approximate the core electrons to reduce computational cost. The geometry of each system was optimized using the BFGS algorithm to obtain lattice parameters and atomic positions corresponding to the ground state, or lowest energy configuration.

In contrast to Γ -point calculations, which only calculate the energy states for one wave vector, k -point sets were used to characterize the behavior of the band structure at different wave vectors, since the valence band maximum and conduction band minimum can occur at k -points other than the Γ -point. Thus, calculations at multiple k -points allow

the description of both indirect and direct band gaps, while Γ -point calculations can only describe direct band gaps.

The density of states (DOS) and band structure were calculated to characterize the electronic structure of each material. A smearing of 0.05 eV was used to generate the DOS plots. All of the DOS plots were shifted such that the highest lying molecular orbital with predominant O 2p character was at zero energy, which was determined by inspection of the molecular orbital isosurfaces. The band gaps were measured from the valence band maximum to the conduction band minimum in the band structure plots (not shown here).

6.3.4 Model systems for DFT calculations

The crystal structures for the 5 different Ti-Fe-O compounds are presented in Figure 6-1. Pristine anatase TiO_2 was modeled using a $2 \times 2 \times 1$ 48 atom supercell (tetragonal: $a = 3.7842 \text{ \AA}$, $c = 9.5146 \text{ \AA}$; I41/AMD symmetry group). Calculations were performed using a $3 \times 3 \times 2$ k -point set. The supercell contained 16 Ti atoms and 32 O atoms. The lattice parameters and atomic positions were optimized to find the lowest energy configuration. The optimized lattice parameters ($a = 3.7878 \text{ \AA}$, $c = 9.8386 \text{ \AA}$) were in close agreement with the experimental values ($\approx 2 \%$) and the atoms retained the experimental I41/AMD symmetry.

Fe-doped anatase TiO_2 was modeled by substituting one Ti atom in the 48 atom anatase supercell with an Fe atom to form $\text{Ti}_{0.9375}\text{Fe}_{0.0625}\text{O}_2$. Calculations were performed using a $3 \times 3 \times 2$ k -point set. The optimized lattice parameters were taken from the pristine anatase TiO_2 calculations. The effect of the Fe atom position in the crystal, as tested by

replacing different Ti atoms, on the total energy of the system and DOS plots was found to be minimal. The initial magnetic spin of the Fe atom was set to the high spin state for Fe^{3+} and optimized during calculations, achieving a final spin state of $+1.6 \mu_{\text{B}}$. The atomic positions were optimized to find their lowest energy configuration. Minimal distortion was observed around the Fe atom and the system largely retained I41/AMD symmetry. The effect of oxygen vacancies was not considered in this study.

Ilmenite TiFeO_3 was modeled using a 30-atom unit cell (hexagonal: $a = 5.1108 \text{ \AA}$, $c = 14.3566 \text{ \AA}$; R-3 symmetry group), which is similar to the corundum ($\alpha\text{-Fe}_2\text{O}_3$) structure. Calculations were performed using a $5 \times 5 \times 1$ k -point set. Various initial magnetic configurations for the Fe atoms were screened to find the lowest energy configuration. The lowest energy magnetic configuration was found to be ferromagnetic, with all spins at $+1.83 \mu_{\text{B}}$ in the (0001) basal plane³⁹. The optimized lattice parameters ($a = 5.1100 \text{ \AA}$, $c = 14.3819 \text{ \AA}$) were in close agreement with the experimental values ($\approx 2\%$), and the atoms retained the experimental R-3 symmetry.

Ti-doped hematite $\alpha\text{-Fe}_2\text{O}_3$ was modeled by substituting one Fe atom in the pristine hematite $\alpha\text{-Fe}_2\text{O}_3$ unit cell (described below) with a Ti atom to form $\text{Fe}_{1.834}\text{Ti}_{0.166}\text{O}_3$. Calculations were performed using a $5 \times 5 \times 1$ k -point set. The optimized lattice parameters were taken from the pristine $\alpha\text{-Fe}_2\text{O}_3$ calculation. After minimization, the atoms retained both the R-3C symmetry and the antiferromagnetic configuration of hematite, save for the slight overall magnetic moment ($+1.8 \mu_{\text{B}}$) due to the Fe in the unit cell.

Pristine hematite $\alpha\text{-Fe}_2\text{O}_3$ was modeled using a 30-atom unit cell (hexagonal: $a = 5.038 \text{ \AA}$, $c = 13.772 \text{ \AA}$; R-3C symmetry group). Calculations were performed using a

5x5x1 k -point set. The lowest energy magnetic configuration was found to be antiferromagnetic, with the spins ($\pm 1.83 \mu_B$) ordered antiferromagnetically in the direction normal to the basal planes but ferromagnetically within the metal bilayers; this agrees well with experimental observations³⁹. The optimized lattice parameters ($a = 5.0665 \text{ \AA}$, $c = 13.9576 \text{ \AA}$) were in close agreement with the experimental values ($\approx 2\%$) and the atoms retained the experimental R-3C symmetry group.

6.3.5 Experimental

Mixed oxide semiconductor films were synthesized using a premixed flame aerosol reactor (FLAR, Figure 6-3). The details of the experimental setup have been published previously^{34, 40}. This synthesis reactor was chosen because it allows precise, rational control over film morphology and chemical composition, both of which are critical to device performance in applications of interest³⁴. The FLAR can be used to form highly crystalline thin films in a single-step, taking approximately 10 to 30 minutes. The synthesis process is based on the deposition of nanoparticles out of the gas phase onto a temperature-controlled substrate.

Metal-oxide nanoparticles were generated by thermal oxidation of metal-organic precursors in a premixed methane-oxygen flame. As the nanoparticles traversed the flame, they grew to reach a controlled size ($d_p < 10 \text{ nm}$) as they arrived at the water-cooled substrate. There was a strong temperature gradient from the hot flame ($T \sim 2000 \text{ }^\circ\text{C}$) to the water-cooled substrate, thus directing the particles to be deposited by thermophoresis. Once on the substrate, due to the elevated substrate temperature ($\sim 600 \text{ }^\circ\text{C}$) and small particle size ($< 10 \text{ nm}$), the nanoparticles sintered together to form large

structures with a bulk electronic band structure, mitigating potential errors due to quantum confinement.

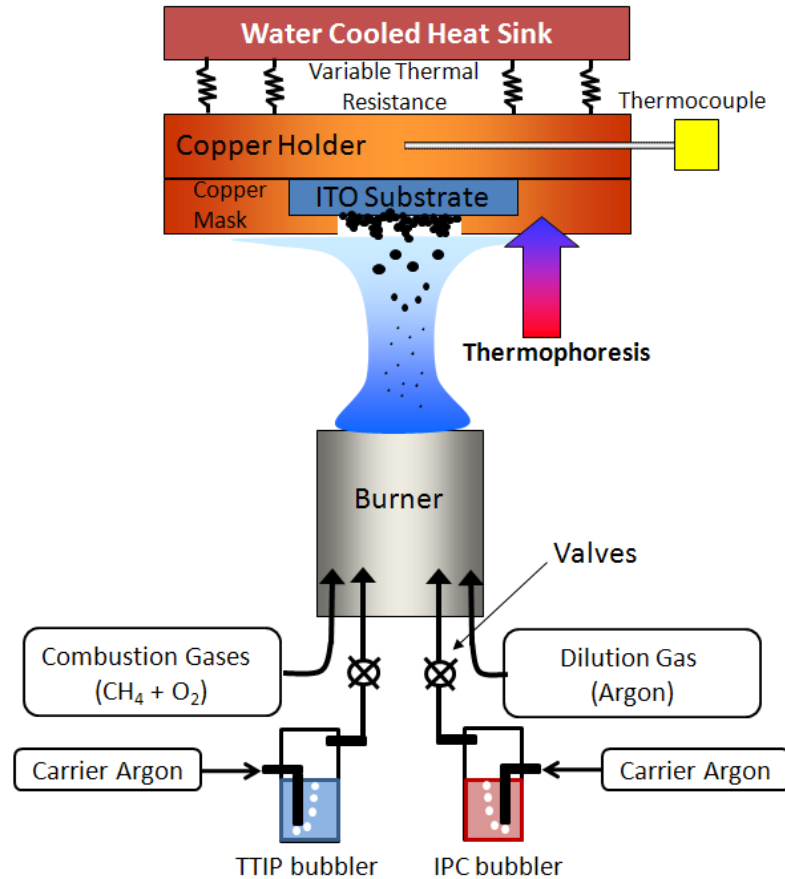


Figure 6-3: Schematic of the FLAR synthesis reactor. The Ti precursor was titanium tetraisopropoxide (TTIP) and the Fe precursor was iron pentacarbonyl (IPC). Details of the synthesis reactor are provided in Thimsen et al^{34, 40}.

The experimental reactor parameters included process gas feed rates of 2.2 lpm (liters per minute at STP) for CH₄, 8.0 lpm for O₂, and an argon flow rate of 12.0 lpm. The substrate was positioned approximately 1.7 cm from the burner outlet. All films were deposited for 15 to 20 min onto indium-tin-oxide (ITO) coated aluminosilicate glass substrates (Delta technologies, Stillwater MN). The measured substrate temperature was approximately 200 °C, corresponding to a surface temperature of approximately 600 °C³⁴.

The films had thicknesses of approximately 1 μm , as measured by scanning electron microscopy.

Mixed Ti-Fe-O thin films were synthesized by co-feeding titanium tetra isopropoxide (TTIP, Sigma-Aldrich) and iron pentacarbonyl (IPC, Sigma-Aldrich) at controlled feed rates. Argon was fed through the bubblers, maintained at a controlled temperature ($T_{\text{TTIP}} = 45\text{ }^{\circ}\text{C}$, $T_{\text{IPC}} = 1.5\text{ }^{\circ}\text{C}$). For TTIP and IPC, the feed rates were calculated from the vapor pressure^{41, 42} and the argon flow rate through the bubbler. A summary of the feed rates and measured chemical compositions of the various experimental thin films is given in Table 1. The feed rates were tuned to deposit films with chemical compositions to match the calculations for the TiO_2 , Fe-doped TiO_2 , TiFeO_3 and $\alpha\text{-Fe}_2\text{O}_3$ cases.

Table 6-1: Summary of the atomic concentrations and crystalline phases of the various experimental films, and the precursor feed rates used to synthesize them. The column A_{TTIP} and A_{IPC} correspond to the flow rate of argon through the TTIP bubbler (43 $^{\circ}\text{C}$) and IPC bubbler (1.5 $^{\circ}\text{C}$).

Target Material	A_{TTIP} (lpm)	A_{IPC} (ccm)	Ti feed Rate (mmol/hr)	Fe feed rate (mmol/hr)	Measured Ti conc. (atom %)	Measured Fe conc. (atom %)	Crystal phase from XRD
1 TiO_2	1.0	0.0	0.90	0.00	100%	0%	anatase TiO_2
2 $\text{Ti}_{0.9375}\text{Fe}_{0.0625}\text{O}_x$	2.0	3.3	1.80	0.12	$93.3 \pm 1.5\%$	$6.7 \pm 1.5\%$	anatase TiO_2
3 TiFeO_x	0.5	13.0	0.45	0.49	$48 \pm 1.0\%$	$52 \pm 1.0\%$	--
4 Fe_2O_3	0.0	18.0	0.00	0.67	0%	100%	$\alpha\text{-Fe}_2\text{O}_3$

The nanostructured thin films were characterized by several techniques. The atomic composition was measured by quantitative x-ray energy dispersion spectroscopy

(EDS) using a Hitachi model S-4500 field emission electron microscope operating at 15 kV equipped with an EDS spectrometer (Noran Instruments). The atomic fraction was measured at 10 locations on the surface of the film, each with an approximate area of 50 μm^2 . The crystal structure of the thin films was characterized with x-ray diffraction using a Rigaku DMax x-ray diffractometer. All of the films were highly scattering, and thus diffuse reflectance spectroscopy was employed to measure the UV-visible light absorption characteristics using a Cary 100 spectrophotometer equipped with an integrating sphere and internal detector for the reference and sample beam (Labsphere, DRA-CA-30I). For diffuse reflectance measurements, the sample was mounted to a certified reflectance standard (Labsphere) before measurements to mitigate errors induced by photon transmission through the sample. All spectra were taken using a certified reflectance standard as the zero-absorbance reference, baseline-subtracted, and normalized. All spectroscopic measurements were performed at room temperature. The absorption edge was taken as the photon energy where the absorbance was 30 % of the maximum. This value corresponds to the energy point where 50 % of the incident photons are absorbed. This approach was taken instead of the conventional approach due to difficulties in assigning the linear region near the absorption edge for the modified absorption cross section plots⁴³.

6.4 Results and Discussion

The predictions of the MMOBS analysis were corroborated by the DFT calculations and experimental results. All three techniques show a decrease in band gap

with increasing Fe content in the Ti-Fe-O compounds until the Fe concentration reaches 50 %, after which the band gap remains constant with increasing Fe content.

6.4.1 MMOBS Analysis

The MMOBS procedure was first used to predict the band structure of the various Fe-Ti-O compounds (Figure 6-2). The term band position in this context refers to the position of the band edge. Thus there are four possible band positions depending on the concentration of Fe and Ti atoms in the compound: two from the valence and conduction bands of TiO₂, and two from the valence and conduction bands of Fe₂O₃. For TiO₂, the valence band is the O 2p level, while the conduction band is the Ti 3d level. For Fe₂O₃, the valence and conduction bands arise from crystal field splitting of the Fe 3d levels due to the octahedral coordination of oxygen around Fe⁴⁺. These levels are given the designation Fe 3d_L (lower) and Fe 3d_U (upper).

The band positions and gaps for 5 Ti-Fe-O compounds are presented in Figure 6-2. For Fe-doped TiO₂, the valence band lies at the O 2p level, the same as TiO₂. There are two conduction bands, one at the Fe 3d_U level, and another at the Ti3d level. The result is a narrowing of the band gap from 3.2 eV for pristine TiO₂, to 2.7 eV for Fe-doped TiO₂. It should be noted that this could be a mid-gap state, or a true conduction band, depending on the mixing with the Ti 3d level.

Mixed Ti-Fe-O compounds with roughly the same amount of Fe and Ti have valence bands at the O 2p and Fe 3d_L levels, and conduction bands at the Fe 3d_U and Ti 3d levels. In these compounds, since the O 2p level is below the Fe 3d_L level, and the Ti 3d level is above the Fe 3d_U level, the band gap is between the Fe 3d_L and Fe 3d_U levels,

with a value identical to that of pristine α -Fe₂O₃ (2.1 eV). The result for Ti-doped α -Fe₂O₃ is similar to that of the mixed Ti-Fe-O.

The MMOBS predictions have implications for the use of materials in the Ti-Fe-O system for photocatalytic water splitting. As soon as there is enough Fe in the semiconductor to red-shift the light absorption, the conduction band edge falls to a slightly lower energy (more positive reduction potential) than the H₂/H₂O potential (see Figure 6-2). To efficiently drive photocatalytic watersplitting, iron-containing oxide semiconductors should be incorporated as thin films into tandem cells^{32, 45}, so a small external voltage can be applied to raise the conduction band edge above the H₂/H₂O redox potential.

6.4.2 DFT Calculations

The DFT results qualitatively agree with the MMOBS analysis (Figure 6-4 and 6-7). The density of states plots for the various compounds is presented in Figure 6-4. For pristine TiO₂, the band gap was between the O 2p band and the Ti 3d band, with a value of 2.2 eV. This value agrees well with published DFT calculations on anatase TiO₂ using the PBE functional^{16, 17}. For the Fe-doped anatase TiO₂, a mid gap state was introduced into the band gap that corresponded to the Fe 3d_U level. Thus the lowest energy band gap for the Fe-doped TiO₂ was between the O 2p and Fe 3d_U level, with a value of 1.3 eV, while another band gap between the O 2p level and Ti 3d level had a value of 2.3 eV. For the remaining compounds, the band gap was between the Fe 3d_L and Fe 3d_U levels. The calculated band gaps for TiFeO₃ (0.78 eV), Ti-doped α -Fe₂O₃ (0.68 eV) and α -Fe₂O₃ (0.73 eV), were all approximately the same. The value for pristine α -Fe₂O₃ is slightly

larger than that reported by Rollmann and others⁴⁶. However, Rollmann and others used the functional of Perdew and Wang (PW91), and it is known that band gap values can change with the functional employed in calculations⁴⁷.

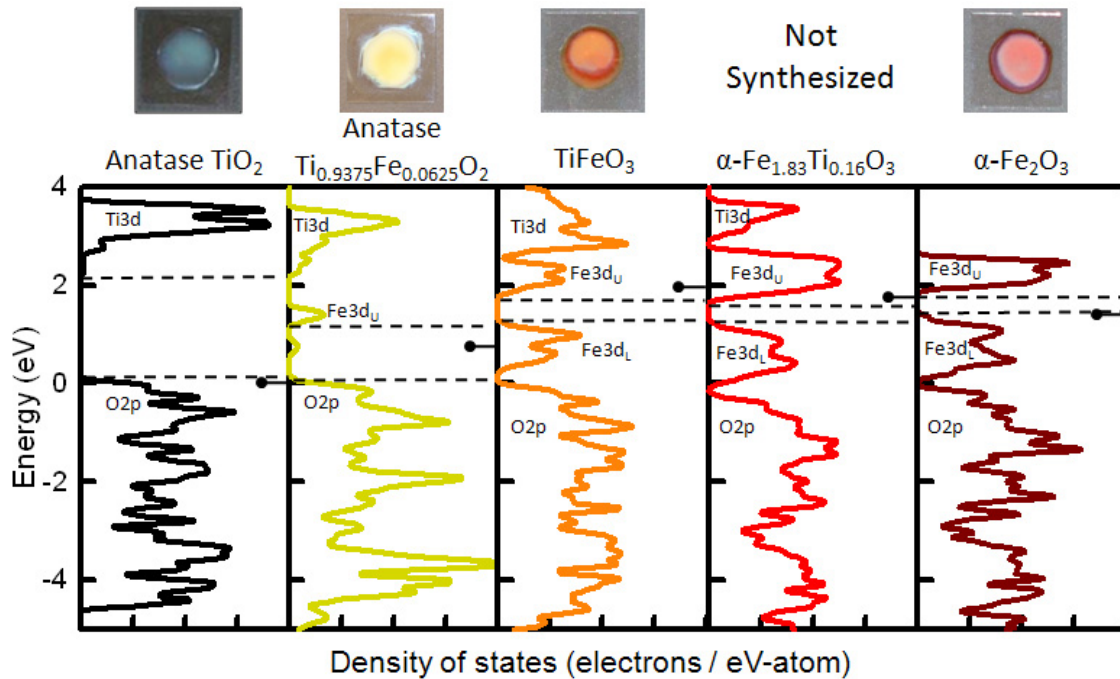


Figure 6-4: Density of state plots generated from DFT calculations for the various Ti-Fe-O compounds. The band gap is indicated by the dashed lines. The Fermi level is indicated by the ball-arrow on the right of each plot. For Fe-doped anatase, the lowest energy band gap is between the O2p band and the midgap state (Fe3d_U), while another band gap exists between the O2p and Ti3d levels. Digital images for the experimental films that correspond to each calculation are presented above the respective plot.

All of the band gap values calculated by DFT are systematically underestimated. The underestimation of band gap values calculated by DFT is a result of a well-known error stemming from the failure of most exchange correlation functionals to cancel out the electronic self-interaction energy⁴⁸, and has been observed many times for the PBE functional^{16, 17, 19, 47}. There are methods to overcome this error, such as the addition of Hubbard correction factors (DFT+U)^{49, 50}, the use of exact Hartree exchange as

implemented in hybrid functionals⁴⁷ and the direct cancellation of the self-interaction error⁴⁸. However, these corrections can introduce an additional level of complexity, difficulty and computational expense to the DFT calculations, and thus were not performed for this study although they could be the focus of future work.

6.4.3 Nanostructured Thin Films

A summary of the experimental results on the nanostructured synthetic thin films is presented in Table 1. The chemical composition, measured by EDS, matched the compositions used in the MMOBS analysis and DFT calculations to within the experimental error. For the Fe-doped TiO₂ film (film 2), the Fe concentration was 6.7 ± 1.5 % based on Ti. For the mixed Ti-Fe-O compound (film 3), the Fe concentration was 52 ± 1.0 % based on Ti. The oxygen concentration in these films could not be determined by EDS, and was not directly measured. Thus these compounds were given the stoichiometric formulas Ti_{0.933}Fe_{0.067}O_x (film 2) and Ti_{0.96}Fe_{1.04}O_y (film 3), where x is in the range from 1.5 to 2 for film 2, and in the range from 3 to 4 for film 3.

The crystal structure of each film was characterized by XRD, as presented in Figure 6-5. Film 1 showed strong XRD peaks that correspond to anatase TiO₂, which is the expected crystal phase for the FLAR synthesis conditions used in this study³⁴. The 6.7 % doped TiO₂ sample (film 2) showed primarily anatase peaks in the XRD pattern, with a small amount of rutile. The rutile is likely a result of the presence of the Fe dopant, which is known to affect the crystallinity of doped TiO₂²⁰. The mixed oxide, Ti_{0.96}Fe_{1.04}O_x, showed virtually no peaks in the XRD pattern over the measured angular range. While it is possible that the film is entirely amorphous, the evidence from the XRD pattern does not necessarily support that conclusion. Rather, it is more reasonable

to assume that the film would not be pure crystalline ilmenite; the highly oxidative flame environment⁵¹, which oxidized the Ti to Ti^{4+} and Fe to Fe^{3+} , naturally prevents the formation of crystalline ilmenite TiFeO_3 with its slightly lower average oxidation state. Film 4 had the $\alpha\text{-Fe}_2\text{O}_3$ crystal structure with a preferred orientation along the (104) direction. Film 3 did not match the presumed ilmenite crystal structure. However, as will be discussed in the upcoming sections, crystal structure appears to play only a minor role in determining band structure.

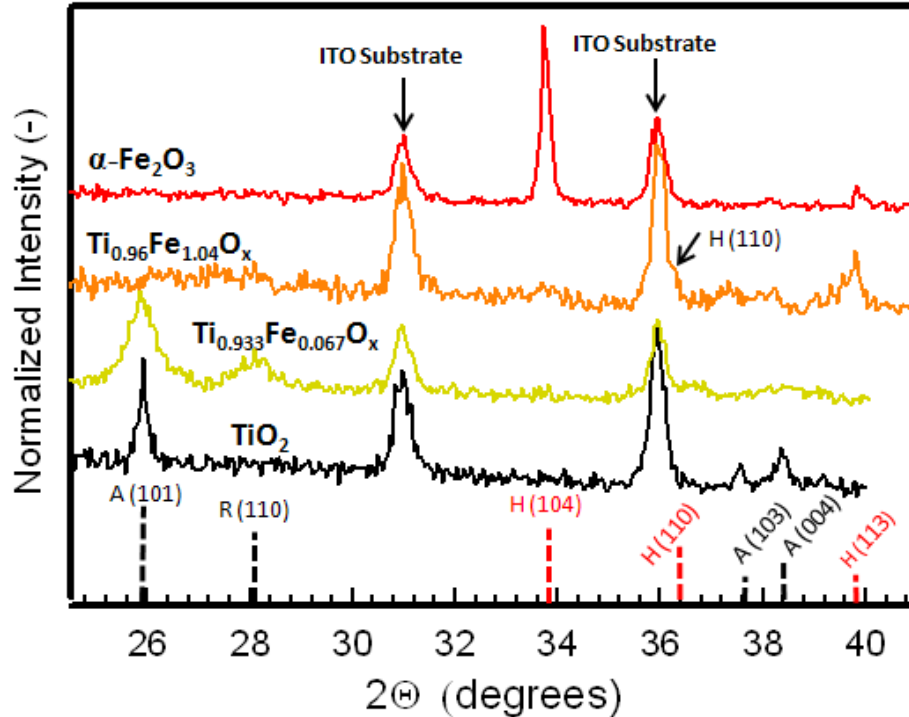


Figure 6-5: X-ray diffraction (XRD) patterns for the 4 experimental films. The two large peaks that were present in all samples correspond to the indium-tin-oxide (ITO) deposition substrate.

The dominant factor affecting the band gap and light absorption characteristics seems to be the atomic composition, which can be seen by examining the UV-visible

absorption spectra in Figure 6-6. As the Fe content of the films was varied from pristine TiO_2 (film 1) to pristine Fe_2O_3 (film 4), the light absorption progressively red-shifted.

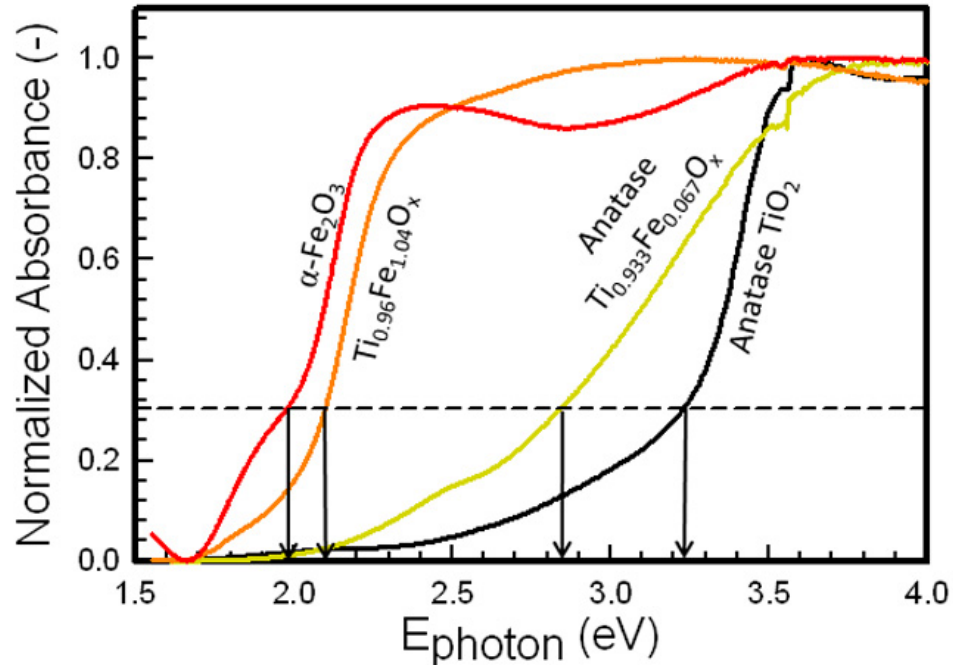


Figure 6-6: Normalized UV-visible absorption spectra measured by diffuse reflectance spectroscopy. The band gap was determined by finding the photon energy at which the normalized absorbance edge reached 30% of its maximum value.

6.4.4 Confirmation of Predictions

The MMOBS predictions were confirmed by the DFT and the experimental results. To illustrate, the band gaps of the various mixed Ti-Fe-O compounds are plotted as a function of Fe concentration in Figure 6-7. As previously mentioned, quantitative agreement with the DFT calculations is not expected due to self-interaction errors that result in the underestimation of band gaps. However, if one uses the DFT band positions for TiO_2 and Fe_2O_3 as the basis values for the MMOBS analysis, the two methods agree at all points except for the Fe-doped TiO_2 , where the DFT calculations predict a narrower band gap than do the MMOBS analysis. This result could stem from the self-interaction

error in the DFT calculations, or could suggest that the MMOBS analysis does not predict the band structure of doped compounds as accurately as mixed compounds. The experimental results also confirmed the MMOBS prediction, as seen in Figure 6-7.

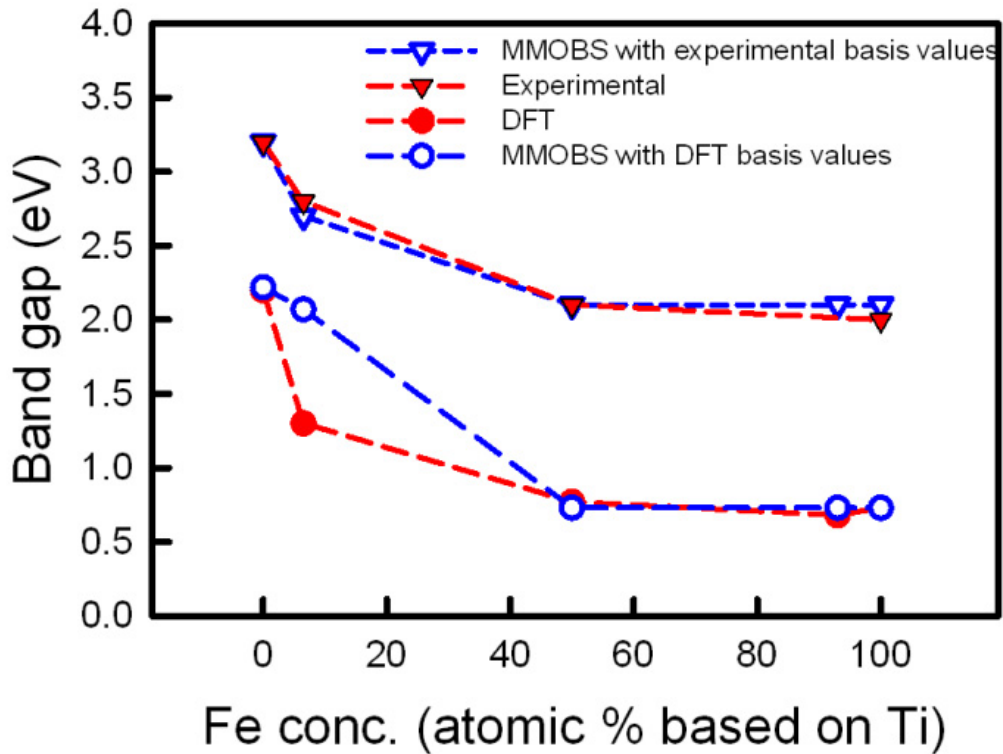


Figure 6-7: Band gaps predicted by MMOBS using experimental and DFT basis values compared to the band gap, as measured experimentally and predicted by DFT.

The atomic composition of semiconductors appears to play a dominant role in determining electronic band structure. The effect of atomic composition on the electronic structure of semiconductors can be illustrated by examining the band gaps of various III-V and II-VI compounds. For instance, the zinc-blende III-V semiconductors InN (1.89 eV), InP (1.34 eV), InAs (0.354 eV) and InSb (0.23 eV) have band gaps that become progressively narrower as the anion increases in atomic number⁵². The same trend in the

band gap can be seen as the atomic number of the cation increases⁵² – 2.15 eV (AlAs) 1.42 eV (GaAs), 0.35 eV (InAs). Again, the same trend is observed in the II-VI semiconductors for the anion⁵² – 3.68 eV (ZnS) 2.70 eV (ZnSe) 2.28 eV (ZnTe), and cation – 2.70 eV (ZnSe) 1.75 eV (CdSe).

By contrast, the crystal structure plays a lesser role than atomic composition in determining the electronic band positions in mixed metal-oxide semiconductors. This is reasonable if one examines other types of semiconductors and compares the effect of atomic composition to the effect of crystal structure. For instance, in the TiO₂ system, the anatase and rutile crystal structures have roughly the same band gaps, 3.2 eV (anatase) and 3.0 eV (rutile), despite the fact that they have different lattice parameters and bulk densities¹⁰; they do both contain octahedral-coordinated Ti atoms. The band-gaps of the hexagonal and cubic polymorphs of II-VI semiconductors typically differ by less than 10 %. For example, the band gap of hexagonal-CdS is 2.49 eV, while cubic-CdS is 2.52 eV⁵². The more important effect of atomic composition relative to crystal structure explains why the Ti_{0.96}Fe_{1.04}O_x compound (Film 3) had the same band gap as that predicted by MMOBS, despite its apparent amorphous structure.

It should be noted that significant differences in crystal structure can in some cases lead to large differences in the electronic energy band structure. This can be illustrated by examining the carbon system. Graphite, which consists of parallel planes of aromatic rings of carbon, is a conductor. By contrast, diamond, which has a face-centered cubic crystal structure, is an insulator with a band gap of 5.4 eV⁵³. In addition, it should also be noted that crystal structure plays a critical role in determining other important properties such as electron transport characteristics and catalytic activity. For

instance, parameters such as crystal defect density can significantly affect electron-hole recombination rates, which in turn can affect the performance of the photocatalyst.

6.4.5 Photocatalyst Design for Water Splitting

The MMOBS procedure is a simple tool that can be used to design new mixed oxide semiconductors that have tailored band gaps and band positions to suit the needs of the application. While this study focused on the Ti-Fe-O system, preliminary DFT calculations we have performed on the Ti-V-O and Ti-Ni-O systems suggest that MMOBS is applicable to those materials as well, indicating that the procedure may be general.

To design a mixed metal-oxide photocatalyst for water splitting with an optimum band gap, several criteria must be met. A general mixed metal-oxide compound containing the transition metal atoms M1 and M2 has the basis compounds (M1)Oxide and (M2)Oxide. The basis compounds must meet the following criteria for (M1)(M2)Oxide to be an efficient photo catalyst for water splitting driven by sunlight.

- 1) At least one of (M1)Oxide and (M2)Oxide must have a conduction band edge at a higher energy (more negative reduction potential) than the H_2/H_2O potential.
- 2) Both (M1)Oxide and (M2)Oxide must have valence band edges at a lower energy (more positive reduction potential) than the H_2O/O_2 potential.
- 3) If a band gap lower than either basis compound is desired, then (M1)Oxide and (M2) Oxide must have a staggered, type-II band offset. Otherwise, the mixed oxide photocatalyst has roughly the same band positions and band gap

as the semiconductor with the narrower band gap (e.g. Fe_2O_3 in the Ti-Fe-O system).

- 4) Between (M1)Oxide and (M2)Oxide, the difference between the highest valence band and lowest conduction band, which is the band gap in the mixed compound, should be approximately 2 eV.

In addition to water splitting, photocatalysts could be designed for arbitrary reduction-oxidation reactions using the above criteria, by simply replacing the $\text{H}_2/\text{H}_2\text{O}$ potential with the potential of the reduction half reaction and the $\text{H}_2\text{O}/\text{O}_2$ potential by the potential of the oxidation half reaction, and adjusting the photocatalytic composition to meet the criteria. To do this, high quality data about the basis compounds must first be obtained from the literature, experimental measurements or quantum mechanical calculations. If this data were compiled, potential combinations could be rapidly screened in a rational fashion.

6.5 Conclusions

A simple Mixed Metal-oxide Band Structure (MMOBS) procedure to predict the electronic energy band structure of mixed metal-oxides was developed. This procedure was applied to the Ti-Fe-O system to determine the band gap and band positions of the compounds representing the range of composition and crystal structures: anatase TiO_2 , Fe-doped TiO_2 , TiFeO_x , Ti-doped $\alpha\text{-Fe}_2\text{O}_3$ and hematite $\alpha\text{-Fe}_2\text{O}_3$. The predictions of the MMOBS procedure were compared to first principles DFT calculations on TiO_2 , $\text{Ti}_{0.9375}\text{Fe}_{0.0625}\text{O}_2$ (Fe-doped anatase TiO_2), ilmenite TiFeO_3 , $\alpha\text{-Fe}_{1.84}\text{Ti}_{0.16}\text{O}_3$ (Fe-doped hematite $\alpha\text{-Fe}_2\text{O}_3$) and $\alpha\text{-Fe}_2\text{O}_3$. The trend in band gap and band position calculated by DFT was qualitatively the same as that predicted by MMOBS. A well-controlled, robust

flame aerosol reactor (FLAR) was then used to fabricate metal-oxide semiconductor thin films with matched composition to compare to the MMOBS analysis and DFT results. The experimental thin films showed the same trend in band gap as that predicted by the MMOBS analysis and DFT calculations. Assuming it can be generally applied, the MMOBS procedure can be used to predict the band structure of mixed metal-oxides, allowing the chemical composition of novel materials to be strategically designed to meet photocatalytic criteria.

6.6 Acknowledgments

We would like to acknowledge partial support from the Washington University Center for Materials Innovation (CMI) and DOD-MURI Grant UR523873. We would also like to thank Chris Hogan, Keith Gilmore, and Emily Jarvis for their helpful comments and conversations while preparing this manuscript.

6.7 References

1. Turner, J. A., Sustainable hydrogen production. *Science* **2004**, 305, (5686), 972-974.
2. Nowotny, J.; Sorrell, C. C.; Sheppard, L. R.; Bak, T., Solar-hydrogen: Environmentally safe fuel for the future. *International Journal of Hydrogen Energy* **2005**, 30, 521-544.
3. Turner, J. A., A realizable renewable energy future. *Science* **1999**, 285, (5428), 687-689.

4. Lewis, N. S.; Nocera, D. G., Powering the planet: Chemical challenges in solar energy utilization. *Proceedings of the National Academy of Sciences of the United States of America* **2006**, 103, (43), 15729-15735.
5. Lewis, N. S., Light work with water. *Nature* **2001**, 414, (6864), 589-590.
6. Cesar, I.; Kay, A.; Martinez, J. A. G.; Gratzel, M., Translucent Thin Film Fe₂O₃ Photoanodes for Efficient Water Splitting by Sunlight: Nanostructure-Directing Effect of Si Doping. *J. Am. Chem. Soc.* **2006**, 128, 4582-4583.
7. Kay, A.; Cesar, I.; Gratzel, M., New benchmark for water photooxidation by nanostructured alpha-Fe₂O₃ films. *Journal of the American Chemical Society* **2006**, 128, (49), 15714-15721.
8. Miller, E. L.; Marsen, B.; Cole, B.; Lum, M., Low-temperature reactively sputtered tungsten oxide films for solar-powered water splitting applications. *Electrochemical and Solid State Letters* **2006**, 9, (7), G248-G250.
9. Alexander, B. D.; Kulesza, P. J.; Rutkowska, L.; Solarska, R.; Augustynski, J., Metal oxide photoanodes for solar hydrogen production. *Journal of Materials Chemistry* **2008**, 18, (20), 2298-2303.
10. Nozik, A. J.; Memming, R., Physical chemistry of semiconductor-liquid interfaces. *Journal of Physical Chemistry* **1996**, 100, (31), 13061-13078.
11. Hardee, K. L.; Bard, A. J., Semiconductor Electrodes. X. Photoelectrochemical Behavior of Several Polycrystalline Metal Oxide Electrodes in Aqueous Solutions. *J. Electrochem. Soc.* **1977**, 124, (2), 215-224.

12. Ihara, T.; Miyoshi, M.; Ando, M.; Sugihara, S.; Iriyama, Y., Preparation of a visible-light-active TiO₂ photocatalyst by RF plasma treatment. *Journal of Materials Science* **2001**, 36, (17), 4201-4207.
13. Dhumal, S. Y.; Daulton, T. L.; Jiang, J.; Khomami, B.; Biswas, P., Synthesis of Visible-Light-Active Nanostructured TiO_x (x < 2) Photocatalysts in a Flame Aerosol Reactor. *Applied Catalysis B: Environmental* **2008**, (Accepted).
14. Park, J. H.; Kim, S.; Bard, A. J., Novel carbon-doped TiO₂ nanotube arrays with high aspect ratios for efficient solar water splitting. *Nano Letters* **2006**, 6, (1), 24-28.
15. Ingler, W. B.; Al-Shahr, M.; Kahn, S. U. M., Efficient Photochemical Water Splitting by a Chemically Modified n-TiO₂. *Science* **2002**, 297, 2243-2245.
16. Di Valentin, C.; Pacchioni, G.; Selloni, A., Theory of carbon doping of titanium dioxide. *Chemistry of Materials* **2005**, 17, (26), 6656-6665.
17. Di Valentin, C.; Pacchioni, G.; Selloni, A., Origin of the different photoactivity of N-doped anatase and rutile TiO₂. *Physical Review B* **2004**, 70, (8), 085116 (1-4).
18. Asahi, R.; Morikawa, T.; Ohwaki, T.; Aoki, K.; Taga, Y., Visible-light photocatalysis in nitrogen-doped titanium oxides. *Science* **2001**, 293, (5528), 269-271.
19. Di Valentin, C.; Finazzi, E.; Pacchioni, G.; Selloni, A.; Livraghi, S.; Paganini, M. C.; Giamello, E., N-doped TiO₂: Theory and experiment. *Chemical Physics* **2007**, 339, (1-3), 44-56.
20. Rane, K. S.; Mhalsiker, R.; Yin, S.; Sato, T.; Cho, K.; Dunbar, E.; Biswas, P., Visible light-sensitive yellow TiO₂-xN_x and Fe-N co-doped Ti_{1-y}Fe_yO₂-xN_x anatase photocatalysts. *Journal of Solid State Chemistry* **2006**, 179, (10), 3033-3044.

21. Ghicov, A.; Macak, J. M.; Tsuchiya, H.; Kunze, J.; Haeublein, V.; Frey, L.; Schmuki, P., Ion implantation and annealing for an efficient N-doping of TiO₂ nanotubes. *Nano Letters* **2006**, 6, (5), 1080-1082.
22. Namiki, N.; Cho, K.; Fraundorf, P.; Biswas, P., Tubular reactor synthesis of doped nanostructured titanium dioxide and its enhanced activation by coronas and soft X-rays. *Industrial & Engineering Chemistry Research* **2005**, 44, (14), 5213-5220.
23. Choi, W. Y.; Termin, A.; Hoffmann, M. R., The Role of Metal-Ion Dopants in Quantum-Sized TiO₂ - Correlation between Photoreactivity and Charge-Carrier Recombination Dynamics. *Journal of Physical Chemistry* **1994**, 98, (51), 13669-13679.
24. Mor, G. K.; Prakasam, H. E.; Varghese, O. K.; Shankar, K.; Grimes, C. A., Vertically oriented Ti-Fe-O nanotube array films: Toward a useful material architecture for solar spectrum water photoelectrolysis. *Nano Letters* **2007**, 7, (8), 2356-2364.
25. Ghicov, A.; Schmidt, B.; Kunze, J.; Schmuki, P., Photoresponse in the visible range from Cr doped TiO₂ nanotubes. *Chemical Physics Letters* **2007**, 433, (4-6), 323-326.
26. Yu, J. C.; Li, G. S.; Wang, X. C.; Hu, X. L.; Leung, C. W.; Zhang, Z. D., An ordered cubic Im $\bar{3}m$ mesoporous Cr-TiO₂ visible light photocatalyst. *Chemical Communications* **2006**, (25), 2717-2719.
27. Umebayashi, T.; Yamaki, T.; Itoh, H.; Asai, K., Analysis of electronic structures of 3d transition metal-doped TiO₂ based on band calculations. *Journal of Physics and Chemistry of Solids* **2002**, 63, (10), 1909-1920.
28. Mor, G. K.; Varghese, O. K.; Wilke, R. H. T.; Sharma, S.; Shankar, K.; Latempa, T. J.; Choi, K.-S.; Grimes, C. A., p-Type Cu $\bar{2}$ Ti $\bar{2}$ O Nanotube Arrays

and Their Use in Self-Biased Heterojunction Photoelectrochemical Diodes for Hydrogen Generation. *Nano Lett.* **2008**, 8, (7), 1906-1911.

29. Fernandez-Garcia, M.; Martinez-Arias, A.; Fuerte, A.; Conesa, J. C., Nanostructured Ti-W mixed-metal oxides: Structural and electronic properties. *Journal of Physical Chemistry B* **2005**, 109, (13), 6075-6083.

30. Woodhouse, M.; Parkinson, B. A., Combinatorial Discovery and Optimization of a Complex Oxide with Water Photoelectrolysis Activity. *Chem. Mater.* **2008**, 20, (7), 2495-2502.

31. Glasscock, J. A.; Barnes, P. R. F.; Plumb, I. C.; Savvides, N., Enhancement of photoelectrochemical hydrogen production from hematite thin films by the introduction of Ti and Si. *Journal of Physical Chemistry C* **2007**, 111, (44), 16477-16488.

32. Gratzel, M., Photoelectrochemical Cells. *Nature* **2001**, 414, 338 - 344.

33. Varghese, O.; Paulose, M.; Shankar, K.; Mor, G.; Grimes, C., Water-Photolysis Properties of Micron-Length Highly-Ordered Titania Nanotube-Arrays. *J. Nanosci. and Nanotech.* **2005**, 5, 1158-1165.

34. Thimsen, E.; Rastgar, N.; Biswas, P., Nanostructured TiO₂ films with controlled morphology synthesized in a single step process: Performance of dye-sensitized solar cells and photo watersplitting. *Journal of Physical Chemistry C* **2008**, 112, (11), 4134-4140.

35. Clark, S. J.; Segall, M. D.; Pickard, C. J.; Hasnip, P. J.; Probert, M. J.; Refson, K.; Payne, M. C., First principles methods using CASTEP. *Zeitschrift Fur Kristallographie* **2005**, 220, (5-6), 567-570.

36. Downs, R. T.; Hall-Wallace, M., The American mineralogist crystal structure database. *American Mineralogist* **2003**, 88, (1), 247-250.
37. Perdew, J. P.; Burke, K.; Ernzerhof, M., Generalized gradient approximation made simple. *Physical Review Letters* **1996**, 77, (18), 3865-3868.
38. Vanderbilt, D., Soft Self-Consistent Pseudopotentials in a Generalized Eigenvalue Formalism. *Physical Review B* **1990**, 41, (11), 7892-7895.
39. Lo, C. S.; Tanwar, K. S.; Chaka, A. M.; Trainor, T. P., Density functional theory study of the clean and hydrated hematite (110) surfaces. *Physical Review B* **2007**, 75, (7), 075425 (1-15).
40. Thimsen, E.; Biswas, P., Nanostructured photoactive films synthesized by a flame aerosol reactor. *Aiche Journal* **2007**, 53, (7), 1727-1735.
41. Okuyama, K.; Kousaka, Y.; Tohge, N.; Yamamoto, S.; Wu, J. J.; Flagen, R. C.; Seinfeld, J. H., Production of Ultrafine Metal Oxide Aerosol Particles by Thermal Decomposition of Metal Alkoxide Vapors. *AIChE J.* **1986**, 32, (12), 2010-2019.
42. Yaws, C. L., *Handbook of vapor pressure*. Gulf Pub. Co.: Houston, 1994.
43. Li, S. S., *Semiconductor physical electronics*. Plenum: New York, 1993; p xiii, 507 p.
44. Morin, F. J., Electrical Properties of alpha-Fe₂O₃. *Physical Review* **1954**, 93, (6), 1195 - 1199.
45. Khaselev, O.; Turner, J. A., A Monolithic Photovoltaic-Photoelectrochemical Device for Hydrogen Production via Water Splitting. *Science* **1998**, 280, 425-427.

46. Rollmann, G.; Rohrbach, A.; Entel, P.; Hafner, J., First-principles calculation of the structure and magnetic phases of hematite. *Physical Review B* **2004**, 69, (16), 165107 (1-12).
47. Bredow, T.; Gerson, A. R., Effect of exchange and correlation on bulk properties of MgO, NiO, and CoO. *Physical Review B* **2000**, 61, (8), 5194-5201.
48. Bylaska, E. J.; Tsemekhman, K.; Gao, F., New development of self-interaction corrected DFT for extended systems applied to the calculation of native defects in 3C-SiC. *Physica Scripta* **2006**, T124, 86-90.
49. Schrier, J.; Demchenko, D. O.; Wang, L. W., Optical properties of ZnO/ZnS and ZnO/ZnTe heterostructures for photovoltaic applications. *Nano Letters* **2007**, 7, (8), 2377-2382.
50. Li, J. B.; Wang, L. W., Band-structure-corrected local density approximation study of semiconductor quantum dots and wires. *Physical Review B* **2005**, 72, (12), 125325 (1-15).
51. Guo, B.; Kennedy, I. M., The speciation and morphology of chromium oxide nanoparticles in a diffusion flame. *Aerosol Science and Technology* **2004**, 38, (5), 424-436.
52. Madelung, O., *Semiconductors--basic data*. 2nd rev. ed.; Springer: Berlin ; New York, 1996; p 317 p.
53. Saslow, W., *Physical Review Letters* 16, (9), 354.

Chapter 7:

Nanostructured Visible Light Active All Oxide p/n Bulk-Heterojunctions for Improved Charge Separation

7.1 Abstract:

Transition metal oxides are attractive materials for harvesting sunlight because they are low cost. While there have been some exciting early discoveries, such as the dye-sensitized solar cell, new device configurations should be explored to further increase efficiencies. The concept of the nanostructured bulk-heterojunction from the polymer solar cell community is applied to transition metal oxide devices. Bulk heterojunctions were synthesized by filling in the spaces between n-TiO₂ columns with p-Cu₂O, where both layers were synthesized by two different industrially relevant processes: a flame aerosol reactor for the n-TiO₂ and electrodeposition for the p-Cu₂O. While the overall thickness of the active layer was roughly constant for each device (between 5.5 and 6.2 μm), the thickness of the bulk heterojunction was varied between 0.2 and 4.6 μm, with the column aspect ratio and volume fraction of p-Cu₂O in the interpenetrating region remaining constant for each device. Increasing the thickness of the bulk heterojunction increased the efficiency of charge collection, resulting in 4.6 times higher power conversion efficiency relative to the thin case. The effect saturated when the bulk heterojunction had roughly the same thickness as the light absorption depth. Increasing the thickness of the bulk heterojunction beyond the light absorption depth resulted in no further efficiency gains. The presence of the n-TiO₂ columns in the p-Cu₂O allows excitons deep in the bulk to be collected, which would normally recombine if the columns were not present.

7.2 Introduction

There is no fundamental scientific limitation preventing the widespread use of solar panels to produce energy. The resource is plentiful, widely distributed, and there are efficient ways of harvesting it. Multijunction cells based on GaInP/GaInAs/Ge with efficiencies of 40 % have been fabricated¹, and silicon solar cells with efficiencies on the order of 15-20 % are routinely manufactured for terrestrial light harvesting. To overcome the temporal and spatial mismatch between energy supply and demand, solar fuels can also be produced²⁻⁶. Photoelectrochemical cells based on GaAs/GaInP₂ have been fabricated that split water into hydrogen and oxygen spontaneously upon illumination by simulated sunlight with power conversion efficiencies of 12%⁷. All of the concepts have been proven. Currently, the issue is that the cost of energy produced by solar panels is roughly 5-10 times higher than that produced by conventional fossil fuels. To surmount the cost issue, extensive work has been done to develop thin film photovoltaics based on CdTe⁸, amorphous silicon⁹ and Cu(In_xGa_(1-x))Se₂¹⁰, and the technologies will undoubtedly have commercial success. However, there are emerging concerns over the costly (In, Ga, Te, Si) and highly toxic (Cd,Pb) materials in these devices. The challenge is now achieving similar efficiencies with low-cost materials that are non-toxic and stable.

Polymer solar cells have been extensively explored as a low-cost alternative material for photovoltaics¹¹⁻¹⁵. These cells have enjoyed significant efficiency gains, mainly brought about by the use of nanostructured bulk-heterojunctions (BHJ) which consist of interpenetrating networks of the p-type and n-type polymers^{12, 16, 17}. The BHJ allows excitons to diffuse to the interface and dissociate into electrons and holes, despite

short exciton diffusion distances on the order of 10-50 nm¹⁴. In essence, the nanostructured BHJ allows one to decouple the light absorption from charge transport. By carefully selecting processing conditions^{13, 18, 19}, nanostructured interfaces can be achieved that increase the conversion efficiency from 3 to 6 times that of a planar junction²⁰, achieving conversion efficiencies of approximately 5% for the best devices¹³. The effect of the nanostructured junction is remarkable, but the power conversion efficiencies still leave room for improvement, and there are also stability issues with polymer-based devices. In addition, because the BHJ is typically synthesized in a single step, relying on internal self-assembly, the detailed structure of the BHJ interface and its effect on performance is not well-understood.

Transition metal oxides are an attractive alternative material. They are highly stable. In addition, so long as earth-abundant materials, such as Ti, Cu and Sn are used, they can be made low cost. Titanium dioxide (TiO₂) has been widely employed in photovoltaic dye-sensitized solar cells^{3, 4, 21}, achieving conversion efficiencies on the order of 11%²². There have been interesting advances in sensitizer development through the use of quantum dots^{23, 24}. However, dye-sensitized solar cells typically contain a liquid electrolyte, which is volatile and can cause stability issues²⁵. There has been some recent work on replacing the electrolyte with polymers²² and less volatile electrolytes²⁶, but the efficiencies still remain below that of the liquid electrolyte. Hybrid inorganic-organic cells have also been explored²⁷, but met with limited success. Amidst the excitement over the successes of the dye-sensitized solar cell, new configurations for transition metal oxide solar cells should be explored to fully realize this technology.

As we move forward towards more efficient and less expensive solar cells, it is necessary to integrate the key concepts from different communities. Some work has been done on solid state BHJs from traditional semiconductor materials²⁸⁻³⁰. To achieve a well-defined material architecture, guest-host synthesis approaches are attractive³⁰. The concept is illustrated in Figure 7-1. Here a well-defined host structure is synthesized, followed by deposition of the guest material to fill the void spaces in the host. This approach has been attempted in other solid-state material systems, such as nanotube TiO₂ host with CdTe guest²⁹, nanotube TiO₂ host with CuInSe₂ guest³⁰, with varying degrees of success. It is typically difficult to completely fill the pores in the host material. The degree of filling depends strongly on the characteristic size of the void spaces and diffusion of the depositing species³⁰. Smaller voids and higher diffusion result in less complete filling.

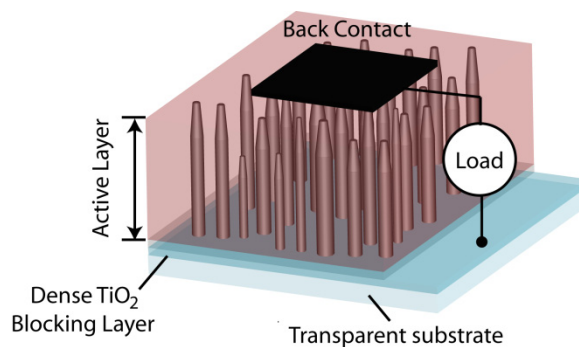


Figure 7-1: Diagram of an inorganic solid state bulk-heterojunction (BHJ) photovoltaic device.

Moving beyond conventional semiconductors to low cost all-oxide devices, the first step in the design/build process is selecting the materials. The p-type and n-type materials must have a type-II band offset, such that the conduction and valence bands of the p-type material are at higher energy than the n-type material, so electrons are segregated into the n-type semiconductor where they are mobile, and holes are segregated

into the p-type semiconductor where they are mobile. Second, the band gap of one of the components must be in the visible region of the spectrum, and should be no greater than 2.4 eV and no less than 0.7 eV if reasonable solar power conversion efficiencies are desired³¹. Third, if one wishes to promote the water splitting reaction, then the conduction and valence bands of both semiconductors must straddle the water reduction-oxidation potentials⁵, and the band gap of the photoactive material should be on the order of 2.0 eV to provide enough energy to split a water molecule (1.23 eV) and overcome potential losses in the system³². The n-TiO₂/p-Cu₂O system meets these criteria (Figure 7-2). The band positions in Figure 7-2 were taken from the literature^{3, 33}. Titanium dioxide (n-TiO₂) is an n-type semiconductor with a wide band gap of 3.2 eV. Cuprous oxide (p-Cu₂O) is a p-type semiconductor with a band gap of 2.0 eV. Based on the band gap, Cu₂O has a theoretical maximum photovoltaic conversion efficiency of about 23 %³¹.

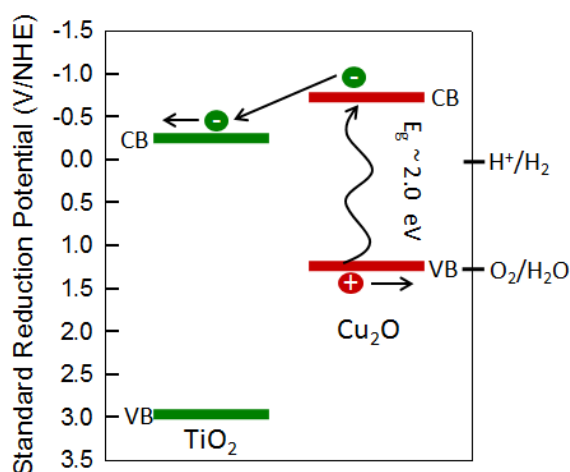


Figure 7-2: Energy level diagram of the TiO₂/Cu₂O system illustrating the conduction band (CB) and valence band (VB) positions. The devices synthesized for this study were used as photovoltaics. The water oxidation and proton oxidation potentials are shown simply to demonstrate that Cu₂O is thermodynamically capable of splitting water, and in particular is attractive for the proton reduction (cathodic) half reaction.

Integrating the concept of the BHJ into transition metal oxide solar cells, this paper presents a systematic study of the effect of BHJ structure on the performance of all-oxide photovoltaic p/n junctions. To the knowledge of the authors, systematic studies on the effect of BHJ thickness and feature size on photovoltaic performance for transition metal oxides, and generally for solid-state inorganic systems, have not yet been conducted. In this paper, we describe results of such a study due to the availability of well-controlled synthesis methods.

7.3 Results and Discussion

7.3.1 Synthesis

For this work, columnar n-TiO₂ films were synthesized on ITO substrates as the host. A dense layer of TiO₂ was deposited on the substrate prior to the columnar n-TiO₂ deposition by spin coating to serve as a hole-blocking layer. The hole-blocking layer is important³⁴ and photovoltaic cells fabricated without it were short-circuited due to the porous nature of the columnar layer which allowed the electrodeposited p-Cu₂O layer to contact the ITO substrate. The columnar n-TiO₂ films were synthesized by a flame aerosol reactor (FLAR), the details of which can be found in our earlier papers^{4, 5, 35}. The FLAR is a rapid, single-step, atmospheric pressure process that affords rational control over film morphology. Typical deposition rates are on the order of 1 nm s⁻¹, allowing micrometer-thick films to be deposited rapidly. It is similar to reactors that are used to make millions of metric tons of materials such as carbon black and TiO₂ pigments. In this process, nanoparticles (less than 10 nm in diameter) were deposited onto a warm substrate where they sintered to form oriented columnar structures, which typically have

long-range crystalline order and in many cases are single crystal⁴. The structures spontaneously self-assemble as a result of the nanoparticle deposition process, no substrate seeding or pretreatment is necessary. Columnar n-TiO₂ films of varying thickness, in the range from 0.2 μm to 4.6 μm were deposited and incorporated into the n-TiO₂/p-Cu₂O BHJ cells.

The guest material was p-Cu₂O. This is the active layer where the photoexcited electrons and holes are generated. The p-Cu₂O was deposited by electrodeposition³⁶ at a temperature of 55 °C in the voids between the n-TiO₂ columns. Electrodeposition is also an attractive synthesis process and is used industrially to produce metallic copper. For all cases in this study, the p-Cu₂O layer was cathodically deposited at a constant current density of 1.0 mA cm⁻² for 60 minutes; corresponding to total charge of 3.6 C cm⁻² and an equivalent dense p-Cu₂O film thickness of 5.4 μm³⁶. In other words, all cells reported in this paper had the same amount of p-Cu₂O, and therefore it is assumed that light absorption and electron-hole pair generation rates were the same in all cells, since n-TiO₂ is transparent in the visible region of the spectrum. However, as will be discussed later, the thickness of the BHJ layer affects the degree to which these electrons and holes are collected.

The BHJ structure consists of interpenetrating layers of n-TiO₂ and p-Cu₂O, as illustrated by the cross-sectional scanning electron microscope (SEM) image in Figure 7-3, along with a schematic illustrating the relevant characteristic dimensions in the device. There were no issues encountered with penetration of the electrodeposited p-Cu₂O into the n-TiO₂ column matrix. This is likely due to the wide spacing between columns (100-400 nm) relative to the diffusion length of the semiconductor precursors in

the electrolyte³⁰. X-ray diffraction measurements confirm that the host is crystalline anatase n-TiO₂ and the guest is crystalline p-Cu₂O (Figure 7-4). The n-TiO₂ columnar host appears to have a random crystallographic orientation, while the p-Cu₂O guest has a (001) orientation. The BHJ structure had a deep red color, and exhibited strong absorption in the visible region of the spectrum. The absorption edge was about 650 nm, in good agreement with the band gap value of 2.0 eV (Figure 7-4). It should be noted for the UV-visible absorption data in Figure 7-4, the area of specimen that contained p-Cu₂O was approximately 50 % of the sample beam, thus the actual absorbance values in the visible region of the spectrum is likely twice the values plotted.

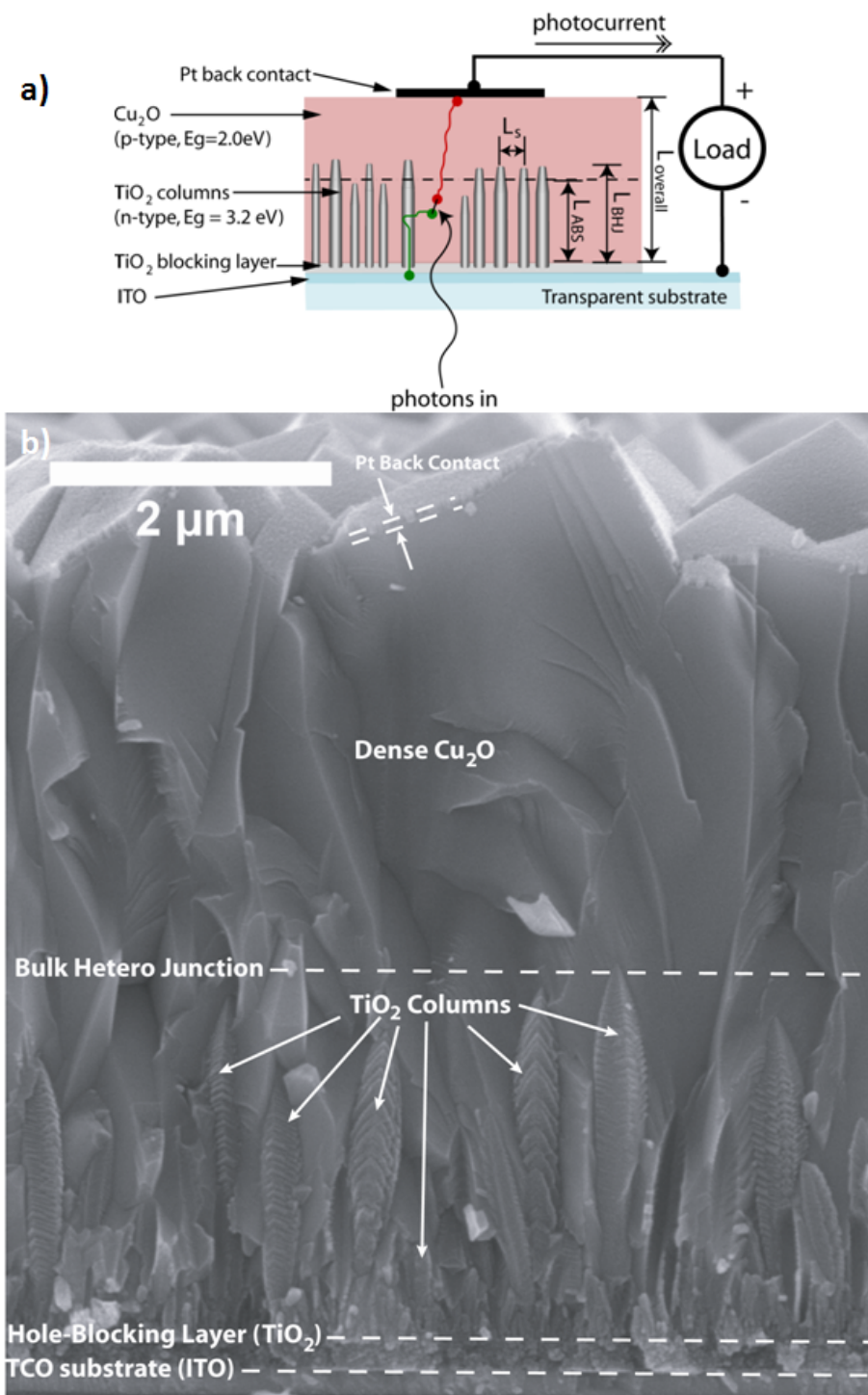


Figure 7-3: a) Side-view schematic showing the important physical dimensions in the device: Column spacing (L_s), light absorption depth (L_{ABS}), bulk heterojunction thickness (L_{BHJ}) and overall thickness ($L_{overall}$). b) Side view SEM image of a BHJ structure synthesized from a 2.5 μm columnar TiO₂ film, illustrating from bottom to top: the ITO TCO layer, dense hole blocking layer, bulk-heterojunction region, pure Cu₂O region, and Pt back contact.

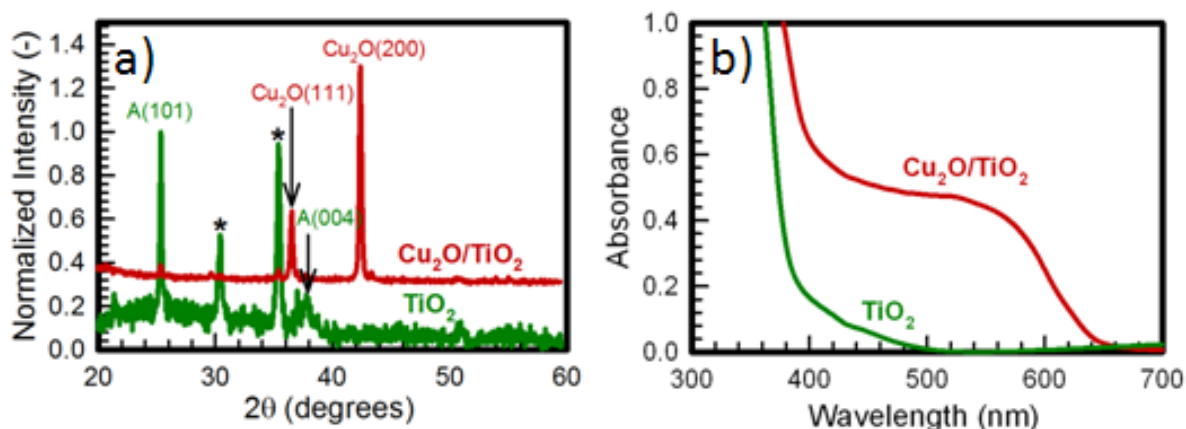


Figure 7-4: X-ray diffraction pattern (a) and UV-visible absorption spectra (b) for 2.3 μm TiO_2 columns with and without Cu_2O . In the XRD pattern, the * correspond to peaks from the Sn-doped In_2O_3 substrate (PDF# 01-088-2160, RDB). The remaining peaks correspond to anatase TiO_2 (PDF# 00-021-1272, RDB) or Cu_2O (PDF# 01-078-2076, RDB). The Cu_2O showed partial orientation along the (100) direction.

Moving to analyze the BHJ in detail, there are several important characteristic dimensions to identify (Figure 7-3a), as they will influence the performance of the device. The first is the light absorption depth L_{ABS} . This is intrinsic to the light-absorbing material, in this case p- Cu_2O . Based on results presented later in this paper, we estimate this depth to be more on the order of 2.0 μm in our system, which is similar to other values reported in the literature³⁷. The second important dimension to identify is the thickness of the BHJ (L_{BHJ}) which is controlled in this study and can be measured from SEM images of the n- TiO_2 columns before p- Cu_2O deposition. The third dimension is the overall thickness of the active layer, L_{overall} . This thickness is important in determining whether the optically active layer is thick enough to absorb all of the light (i.e. $L_{\text{overall}} > L_{\text{ABS}}$). All of the cells used in the present study had overall thicknesses greater than the estimated absorption depth. The last important dimension is the column spacing (L_s) which determines the width of the filaments of p- Cu_2O extending into the

BHJ. The spacing is difficult to measure directly. It is easier to measure the column diameter. For the purposes of this paper, the column spacing is assumed to be the same as the column diameter, which agrees with the SEM results.

Bulk heterojunctions with four different n-TiO₂ column thicknesses (L_{BHJ}) were synthesized by controlling the deposition time in the FLAR^{4, 35}. Cross-sectional SEM images of the n-TiO₂ films before and after p-Cu₂O deposition are presented in Figure 7-5. Elemental maps constructed by EDS using Ti-K_α and Cu-K_α X-rays in the SEM clearly reveal the inter-penetrating nature of the interface (Figure 7-6). The thickness of the n-TiO₂ film before p-Cu₂O deposition was measured approximately 75 times at various positions on the film at various magnifications by hand. The width of the columns for each film was measured at the thickest point on 75 different columns by hand. The overall thickness of the n-TiO₂/p-Cu₂O structure was measured in the same way. The average values along with the standard deviations of the measurements are presented in Table 7-1.

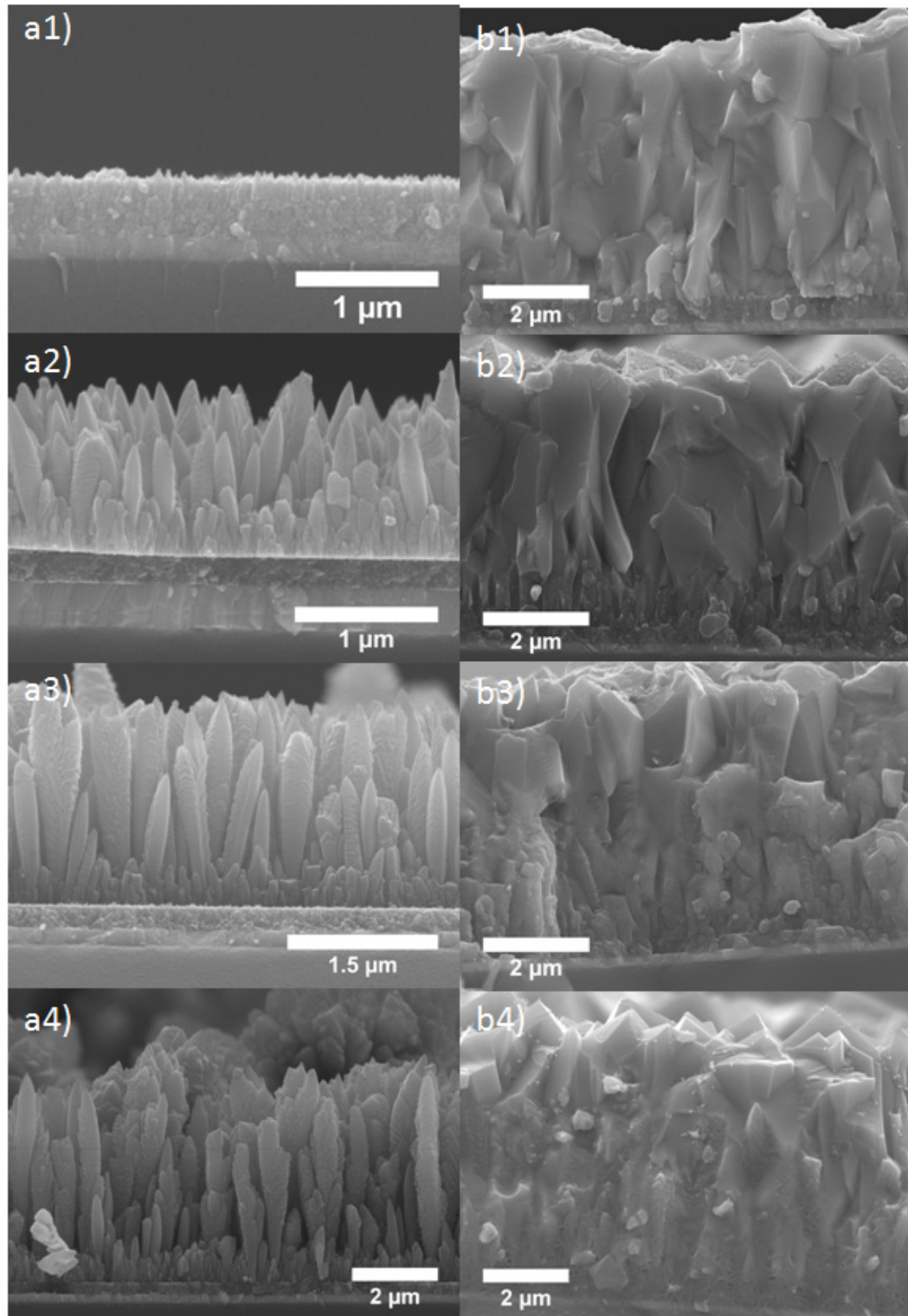


Figure 7-5: Side view SEM images of TiO₂ columns for cells 1-4 before (a1-4) and after (b1-4) Cu₂O deposition.

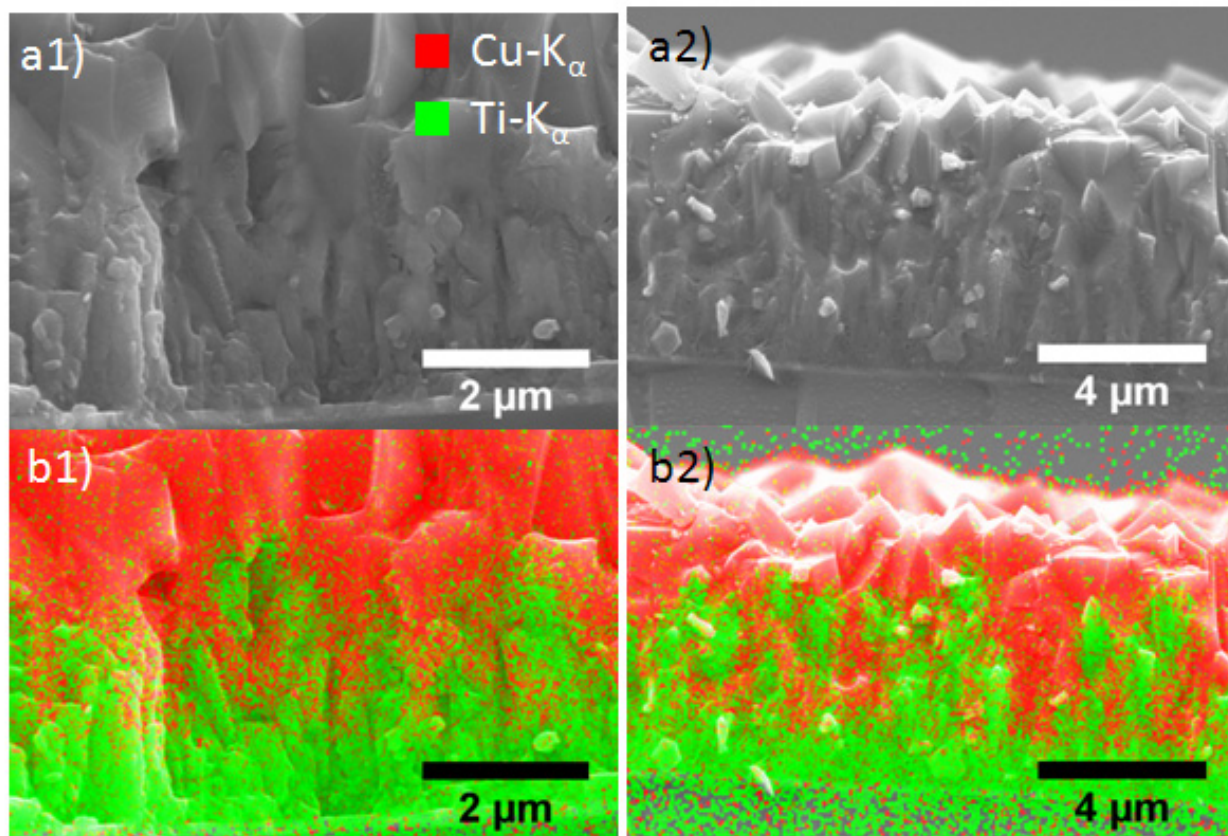


Figure 7-6: Side view SEM images (a) and elemental maps (b) taken by X-EDS for cell 3 (a1,b1) and cell 4 (a2,b2) illustrating the inter-penetrating nature of the n-TiO₂/p-Cu₂O interface.

Table 7-1: Summary of the relevant physical dimensions of each BHJ device. For comparison, the light absorption depth is approximately 2.0 μm.

Cell	L_{BHJ} (μm)	Column Diameter (L_s , μm)	Column Aspect Ratio	L_{overall} (μm)	$\Phi_{\text{Cu}_2\text{O}}$
1	0.21 ± 0.02	-	-	5.46 ± 0.17	$71 \pm 5 \%$
2	1.17 ± 0.08	0.15 ± 0.04	8.1 ± 1.3	5.67 ± 0.26	$77 \pm 4 \%$
3	2.27 ± 0.31	0.24 ± 0.08	9.5 ± 2.2	5.84 ± 0.26	$81 \pm 7 \%$
4	4.56 ± 0.62	0.44 ± 0.19	10 ± 2.8	6.62 ± 0.42	$73 \pm 7 \%$

There are several notable trends in the dimensions of the various bulk heterojunctions, such as the column width. As the thickness of the columnar film (L_{BHJ}) increases, so does the column width (L_s). Indeed, it appears as though the resulting

column aspect ratio (L_{BHJ} / L_s) is roughly constant for the deposition conditions used in this study. Assuming that the p-Cu₂O completely fills the inter-column spaces, the volume fraction of p-Cu₂O in the BHJ can be derived from geometric arguments based on volume conservation, and calculated using the following expression:

$$\phi_{Cu_2O} = 1 - \frac{L_{overall} - L_{0,Cu_2O}}{L_{BHJ}} \quad (7-1)$$

Where ϕ_{Cu_2O} is the volume fraction of p-Cu₂O in the BHJ region and L_{0,Cu_2O} is the equivalent thickness of the p-Cu₂O layer if it were homogenous and dense, which can be calculated from the total charge passed during electrodeposition (3.6 C cm⁻²) to be approximately 5.4 μm. From Table 7-1, it can be seen that the volume fraction of p-Cu₂O in the BHJ region remains constant, despite the increase in BHJ thickness. This is likely a result of the column aspect ratio remaining constant.

7.3.2 Photovoltaic Characteristics

The thickness of the BHJ region had a strong influence on the photovoltaic performance of the cells. The I-V curves generated under simulated AM1.5G illumination are presented in Figure 7-7, with the performance metrics tabulated in Table 7-2. The short circuit current increased from 0.42 to 1.07 mA cm⁻² as L_{BHJ} went from 0.2 μm to 2.3 μm, and then remained constant for the 4.6 μm case. These currents were much higher than the current expected from n-TiO₂ only, which is approximately 0.1 mA cm⁻².³⁸ The I-V curves in the dark of cells with L_{BHJ} values of 0.2 μm and 4.6 μm are presented in Figure 7-7. The cells exhibited rectifying behavior in the expected direction. While the overall conversion efficiency of these cells was relatively low, likely from the poor quality of the spin-coated hole-blocking layer³⁹ and unoptimized p-Cu₂O deposition

conditions³⁶, significant performance gains were achieved by increasing the BHJ thickness. Indeed, the short-circuit current went up by a factor of 2.6, and the overall conversion efficiency went up by a factor of 4.3 (Table 7-2). Since the light absorption in all of the cells was similar, the performance gains achieved with increasing L_{BHJ} are a result of improved charge collection.

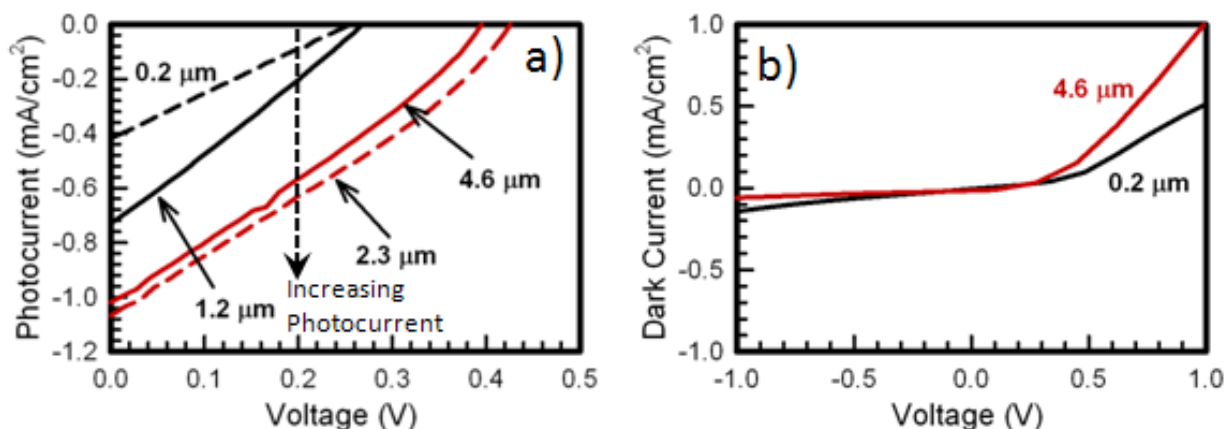


Figure 7-7: I-V curves measured as a function of BHJ thickness (L_{BHJ}) under simulated AM1.5 G illumination (a) and rectifying characteristics of cells 1 and 4 in the dark (b).

Table 7-2: Summary of the photovoltaic characteristics of each cell measured under simulated AM1.5G illumination.

Cell	I_{sc} (mA cm ⁻²)	V_{oc} (V)	FF	Power Conversion Efficiency (%)
1	0.42	0.26	0.24	0.03
2	0.73	0.27	0.26	0.05
3	1.07	0.42	0.29	0.13
4	1.02	0.40	0.28	0.11

There are several fundamental events that occur in p/n junction-based devices that lead to charge separation and generation of the electron motive force. The first is light absorption. Photons are absorbed over the entire depth of the material, with an exponentially decreasing intensity as the beam passes through the sample. Most of the

photons are absorbed within the absorption depth ($\sim 62\%$, if $L_{ABS} = \alpha^{-1}$). Each absorbed photon leads to the generation of an exciton, which is an electrostatically neutral particle consisting of an excited bound electron-hole pair. This exciton can then recombine or separate, depending on the where it is generated, its diffusion length and lifetime.

At the interface between the n-type (n-TiO₂) and p-type (p-Cu₂O) materials, there exists a region of strong electric field caused by depletion of electrons and holes relative to the bulk to obtain equilibrium, called the depletion region. If an exciton finds itself in the depletion region, it will separate. The electrons flow towards the n-type material and the holes flow in the p-type material. Once electrons are segregated into the n-type material, and holes in the p-type material, the charge transport to the electrical contact is a majority-carrier process, very efficient, and charge collection is relatively easy. However, exciton diffusion to the depletion region is not efficient, as it is completely random process due to the electrical neutrality of the particle. It is much more efficient to generate the exciton *directly* in the depletion layer. Since p-Cu₂O is the photoactive species in the cells synthesized for this study, we will focus on the p-type material. The width of the depletion region in the p-type material of a p/n heterojunction can be estimated by the following equation⁴⁰:

$$W_p = \left[\frac{2N_D \epsilon_n \epsilon_p \epsilon_0 V_{Bi}}{qN_A (\epsilon_n N_D + \epsilon_p N_A)} \right]^{1/2} \quad (7-2)$$

Where ϵ_0 is the vacuum permittivity (5.526×10^{-12} e V⁻¹ cm⁻¹), N_D and N_A and the donor and acceptor concentrations in the n-type and p-type semiconductors respectively, ϵ_n and ϵ_p are the relative dielectric constants of the n-type and p-type semiconductors, q is the elementary unit charge and V_{Bi} is the built-in potential at the interface. The dielectric constants are taken to be 7.11 and 45 for p-Cu₂O⁴¹ and n-TiO₂⁴² respectively. The

accepter and donor concentrations depend strongly on the doping concentration, but the intrinsic values are reported to be approximately 10^{15} cm^{-3} and 10^{18} cm^{-3} for p-Cu₂O⁴³ and n-TiO₂⁴⁴ respectively. Since the photovoltaic effect under simulated sunlight primarily arises from visible-wavelength excitons created in the p-Cu₂O, the built-in potential is estimated to be the difference between the conduction band of p-Cu₂O and the conduction band of n-TiO₂, which is approximately 0.61 V (Figure 7-2). Entering these values into equation (7-2) yields a depletion layer thickness of 0.69 μm .

In the BHJ structures, the depletion region emanates from the columns, in contrast to a planar junction where it can be thought of as a slab at the interface (Figure 7-8). If it is assumed that only excitons generated in the depletion region result in collected current, in the planar case only excitons generated in the 0.69 μm depletion region result in photocurrent while many excitons generated over the $\sim 2 \mu\text{m}$ absorption depth are wasted.

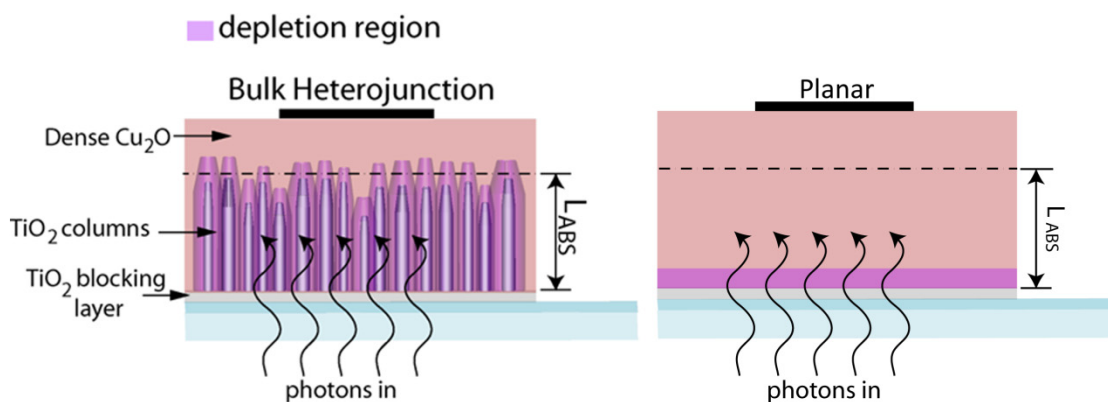


Figure 7-8: Schematic illustrating the proposed difference between the depletion region in a BHJ device and a planar device.

In the case of the BHJ, the situation is different. The average inter-column spacing is less than the depletion region width. Since it emanates from columns, the effective depletion region assumes the same thickness as the BHJ, which can be

controlled through the thickness of the TiO_2 columns (L_{BHJ}). Thus, excitons over the entire absorption depth can be harvested by setting $L_{\text{BHJ}} = L_{\text{ABS}}$, resulting in significantly improved photocurrent generation. Increasing L_{BHJ} beyond this point offers no advantages in terms of charge collection (Figure 7-9). Thus, assuming the column spacing is less than the depletion region width, the optically active material is thick enough to absorb the incident photons, and charge carrier transport is sluggish (which looks like the case for polymer and oxide solar cells), devices with $L_{\text{BHJ}} < L_{\text{ABS}}$ are charge carrier *transport-limited*, and devices with $L_{\text{BHJ}} > L_{\text{ABS}}$ are *recombination-limited* (Figure 7-9).

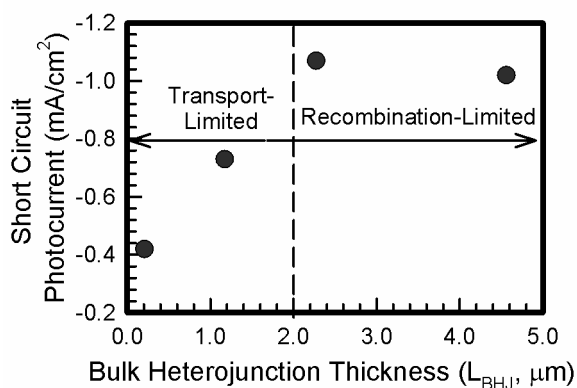


Figure 7-9: Short circuit photocurrent density as a function of BHJ thickness (L_{BHJ}) under simulated AM1.5 G illumination showing the saturation of the photocurrent when $L_{\text{BHJ}} \sim L_{\text{ABS}}$.

It was observed that this guest/host nanostructuring approach can be used to improve the performance of these devices by over a factor of 4, which is similar to the improvements reported by the polymer solar cell community. The present devices could be further improved by depositing a higher quality hole-blocking layer by spray pyrolysis⁴⁵, carefully controlling the p- Cu_2O deposition conditions^{30, 36}, and post-processing such as annealing the junctions to improve interfacial contact, charge transport

and reduce defect concentrations in the structure. Also, interfacial layers between the p-type and n-type materials would likely help²⁸. Simple steps like these can lead to performance gains of several orders of magnitude⁴. Since the present devices are among the first of their kind, this result is promising and significant improvements in performance are expected in the future.

7.4 Conclusions

It is important to explore new device configurations, particularly for transition metal-oxides to fully their potential to harvest sunlight. However, it is not only important to explore new configurations, but also to conduct systematic studies to understand how the relevant parameters influence performance. Towards these ends, bulk heterojunctions between columnar n-TiO₂ and p-Cu₂O were successfully synthesized. The p-Cu₂O was electrodeposited to fill in the spaces between the n-TiO₂ columns, which were deposited by a flame aerosol reactor (FLAR). The important characteristic dimensions of the BHJ were identified: the BHJ thickness (L_{BHJ}), inter-column spacing (L_s), guest volume fraction (ϕ_{Cu_2O}) and absorption depth (L_{ABS}). The columnar film thickness (L_{BHJ}) was varied between 0.2 μm to 4.6 μm ; with the column radius (L_s) varied between $< 0.15 \mu\text{m}$ and 0.44 μm . The p/n junction exhibited rectifying characteristics and the devices behaved as photovoltaics under simulated AM1.5G illumination. The photocurrent developed by the cells increased with n-TiO₂ column thickness until the bulk heterojunction thickness (L_{BHJ}) was the same as the light absorption depth (L_{ABS}), resulting in a 2.6 times more photocurrent and 4.3 times higher conversion efficiency than the thin case. Increasing L_{BHJ} beyond the absorption depth (L_{ABS}) resulted in no further performance gains. It is proposed that in the present devices the depletion region

occupies the entire inter-column spacing (L_s). Since the absorption depth in p-Cu₂O is much larger than the depletion region of a planar junction, increasing the BHJ thickness provides access to excitons deep in the bulk that would normally recombine if the n-TiO₂ columns were not there, improving the device performance.

7.5 Methods

This section summarizes details for synthesis of the n-TiO₂ layer, p-Cu₂O layer and back contact; as well as the details of materials characterization and photovoltaic characterization.

The base substrates used in this study consisted of a 180 nm ITO film deposited on 25.4 mm X 25.4 mm X 0.7 mm Corning 1737 glass (Delta Technologies, Stillwater MN) and were used as-received with no further treatment.

A dense, nanocrystalline TiO₂ layer was deposited onto the ITO as a hole-blocking layer by spin-coating. The solution was 0.4 ml of titanium tetra-isopropoxide (TTIP) dissolved in 4 ml of toluene. Spin coating solutions more concentrated than this resulted in significant cracking upon annealing, and concentrations less than this resulted in incomplete coverage. Before spin coating, a small portion of the substrate was masked to ensure that electrical contact could be made to the ITO after dense TiO₂ deposition. A drop of 0.1 ml of this solution was applied to the substrate while it was spinning at 1000 RPM for 4 seconds, followed by high-speed spinning at 5200 RPM for 30 seconds. The resulting thin film was annealed at 450 °C for 3 min, to give a partially-annealed nanocrystalline³⁹ layer 80 nm in thickness. The spin coating process was repeated 3 times to yield a 240 nm dense layer, which was finally annealed at 450 °C for 40 min.

The columnar n-TiO₂ was deposited on the dense n-TiO₂ using a flame aerosol reactor, the experimental details of which can be found in our earlier papers^{4, 35}. The substrate (ITO/dense TiO₂) was positioned 2.7 cm away from the burner outlet. The substrate was fixed to the copper substrate holder using a small amount of thermal paste (Arctic Silver 5, Arctic Silver, Visalia CA). A copper mask was applied to restrict the deposition of the columnar TiO₂ to a 15 mm circle in the center of the substrate. A 1/4 " stainless steel insert was placed between the copper substrate holder and copper heat sink to increase the thermal resistance and therefore substrate temperature^{4, 35}. The stainless steel insert was fixed to the substrate holder using thermal paste. The process gas flow rates, controlled by digital mass flow controllers (MKS, Wilmington MA) were methane = 2.0 liters per minute at standard temperature and pressure (lpm), oxygen = 8.0 lpm and Ar(dilution) = 9.5 lpm. The titanium precursor was TTIP and it was fed into the flame using a homemade bubbler. The bubbler temperature was maintained at 47 °C, and the argon flow rate through it was 0.5 lpm, corresponding to a TTIP feed rate of 0.60 mmol h⁻¹. The substrate holder temperature (which is much lower than the substrate surface temperature) was 165 °C for these deposition conditions. The thickness of the columnar films was controlled through the deposition time, with film 1, 2, 3 and 4 (Table 7-1) corresponding to deposition times of 4 min, 16 min, 32 min and 64 min respectively.

The p-Cu₂O layer was deposited by electrodeposition from a high pH solution containing chelated Cu(II) ions³⁶. Before deposition, the substrates (ITO/dense TiO₂/columnar TiO₂) were masked using a medium viscosity clear multipurpose adhesive (E6000, Eclectic Products, Pineville LA). An area ~0.7 cm² in the center of the columnar region of the substrate was exposed, with the rest of the substrate covered with sealant.

The precise exposed area of n-TiO₂ was measured from calibrated digital images using the ImageJ software package. If this adhesive was not applied than the p-Cu₂O preferentially deposited on the regions of the substrate that contained no columnar TiO₂, creating a highly non-uniform sample. A solution of 3 M lactic acid and 0.2 M copper sulfate in deionized (DI) water was prepared for the electrolyte. The pH of this solution was adjusted to 12.4 (measured by an in-situ pH probe) through the addition of a solution of 1M NaOH in DI water. The total volume of the 1M NaOH solution added was approximately 80 ml. As the NaOH solution is added, the color goes from light blue (low pH) to dark brown/black (neutral pH) to a deep rich blue (high pH). This solution was then heated in a 250 ml beaker to 55 °C, where it was maintained for the duration of deposition. A two-electrode configuration was used for deposition, with a Pt counter electrode (anode) and the masked columnar n-TiO₂ substrate as the working electrode (cathode). Deposition was carried out at a constant current density of 1.0 mA cm⁻² controlled by a digital source/meter (model 2400, Keithly Instruments, Cleveland OH). During deposition the applied voltage (automatically controlled) fluctuated between 1.0 and 1.2 V. In a select experiment, the potential of the working electrode was measured with respect to a saturated calomel reference electrode (SCE) and found to be approximately -0.6 V/SCE. Deposition was carried out for 60 min, corresponding to a total charge of 3.6 C cm⁻². After deposition, the sample was removed from the electrolyte, rinsed thoroughly with DI water and dried in the ambient.

The back electrical contact to the p-Cu₂O layer was accomplished by sputter coating Pt and then forming a final connection with electrically conductive paste. Before sputter coating the Pt, a 0.2 cm² region of the center of the p-Cu₂O was exposed, with the

rest of the sample being masked by electrical tape. A 70 nm Pt layer was then deposited on the exposed region by sputter coating. Contact to the thin Pt layer was established by apply a small amount of electrically conductive paste (SPI, Westchester PA), which was then easy to connect to the external measurement circuit.

The active layer of the device, before and after p-Cu₂O deposition, was characterized by side-view scanning electron microscopy (SEM), spatially resolved X-ray energy dispersion spectroscopy (X-EDS elemental mapping), X-ray diffraction (XRD) and UV-visible diffuse reflectance spectroscopy. Specimens for SEM and X-EDS mapping were prepared by mechanically cleaving the sample down the center of the active area followed by imaging in a JEOL 7001LVF FE-SEM operating at 15 kV. Distance measurements were performed by hand using ImageJ. Specimens for XRD characterization were measured before back contact deposition, with and without p-Cu₂O in a Rigaku DMAX/A diffractometer using Cu-K_α radiation. UV-visible diffuse reflectance measurements were performed in a Cary 300 (Varian, Palo Alto CA) equipped with an integrating sphere (DRA-CA-30I, Labsphere, North Sutton NH) by illuminating the sample through the transparent substrate at an incidence angle of 0°. For UV-visible measurement, the sample was mounted to a certified reflectance standard to mitigate errors induced by photon transmission through the sample. The spectra are corrected for the profile of the certified reflectance standard and baseline-subtracted. Only half of the sample beam was taken up by the p-Cu₂O region, while the TiO₂ occupied the entire beam. Thus, the actual absorption in the visible region of the spectrum is much higher than what is plotted in Figure 7-4.

The I-V curves for the various cells were measured under illumination from a solar simulator operating at 190 W (Oriel Light Sources, Stratford CT). The output was calibrated using a spectroradiometer to achieve the same integrated power density over the wavelength range from 220 nm to 950 nm as the AM 1.5 G spectra, which is 72 mW cm^{-2} . The active area was masked using electrical tape to be 0.2 cm^2 . The cell was illuminated through the transparent conducting substrate. The current was measured as a function of applied voltage using a digital source meter (2400, Keithley). The global efficiency was calculated using the following equation: $\eta = \frac{V_{oc}I_{sc}FF}{I_0} * 100$ where I_0 is the total incident intensity (100 mW cm^{-2}) and $FF = \frac{w_{mp}}{V_{oc}I_{sc}}$ where w_{mp} is the maximum power developed by the cell. The results presented are representative of approximately 13 cells that were tested.

7.6 Acknowledgements:

This work was partially supported by Corning Incorporated and DOD-MURI Grant UR523873. We would also like to thank the Center for Materials Innovation at Washington University in Saint Louis for facilities support, and Manoranjan Sahu, Woojin An and Chris Singer for helpful comments in preparing this manuscript.

7.7 References

1. King, R. R.; Law, D. C.; Edmondson, K. M.; Fetzer, C. M.; Kinsey, G. S.; Yoon, H.; Sherif, R. A.; Karam, N. H., 40% efficient metamorphic GaInP/GaInAs/Ge multijunction solar cells. *Applied Physics Letters* **2007**, 90, (18), -.
2. Fujishima, A.; Honda, K., Electrochemical Photolysis of Water at a Semiconductor Electrode. *Nature* **1972**, 238, 37.
3. Gratzel, M., Photoelectrochemical Cells. *Nature* **2001**, 414, 338 - 344.
4. Thimsen, E.; Rastgar, N.; Biswas, P., Nanostructured TiO₂ films with controlled morphology synthesized in a single step process: Performance of dye-sensitized solar cells and photo watersplitting. *Journal of Physical Chemistry C* **2008**, 112, (11), 4134-4140.
5. Thimsen, E.; Biswas, S.; Lo, C.; Biswas, P., Predicting the band structure of mixed metal-oxides: Theory and Experiment. *J. Phys. Chem. C* **2009**, 113, (5), 2014-2021.
6. Crawford, S.; Thimsen, E.; Biswas, P., Impact of Different Electrolytes on Photocatalytic Water Splitting. *Journal of the Electrochemical Society* **2009**, 156, (6), H346-H351.
7. Khaselev, O.; Turner, J. A., A Monolithic Photovoltaic-Photoelectrochemical Device for Hydrogen Production via Water Splitting. *Science* **1998**, 280, 425-427.
8. Beach, J. D.; McCandless, B. E., Materials challenges for CdTe and CuInSe₂ photovoltaics. *Mrs Bulletin* **2007**, 32, (3), 225-229.
9. Chopra, K. L.; Paulson, P. D.; Dutta, V., Thin-film solar cells: An overview. *Progress in Photovoltaics* **2004**, 12, (2-3), 69-92.

10. Contreras, M. A.; Ramanathan, K.; AbuShama, J.; Hasoon, F.; Young, D. L.; Egaas, B.; Noufi, R., Diode (characteristics in state-of-the-art ZnO/CdS/Cu(In(1-x)Gax)Se-2 solar cells. *Progress in Photovoltaics* **2005**, 13, (3), 209-216.
11. Halls, J. J. M.; Walsh, C. A.; Greenham, N. C.; Marseglia, E. A.; Friend, R. H.; Moratti, S. C.; Holmes, A. B., Efficient Photodiodes from Interpenetrating Polymer Networks. *Nature* **1995**, 376, (6540), 498-500.
12. Yu, G.; Gao, J.; Hummelen, J. C.; Wudl, F.; Heeger, A. J., Polymer Photovoltaic Cells - Enhanced Efficiencies Via a Network of Internal Donor-Acceptor Heterojunctions. *Science* **1995**, 270, (5243), 1789-1791.
13. Peet, J.; Kim, J. Y.; Coates, N. E.; Ma, W. L.; Moses, D.; Heeger, A. J.; Bazan, G. C., Efficiency enhancement in low-bandgap polymer solar cells by processing with alkane dithiols. *Nature Materials* **2007**, 6, (7), 497-500.
14. Peumans, P.; Yakimov, A.; Forrest, S. R., Small molecular weight organic thin-film photodetectors and solar cells. *Journal of Applied Physics* **2003**, 93, (7), 3693-3723.
15. Li, G.; Shrotriya, V.; Huang, J. S.; Yao, Y.; Moriarty, T.; Emery, K.; Yang, Y., High-efficiency solution processable polymer photovoltaic cells by self-organization of polymer blends. *Nature Materials* **2005**, 4, (11), 864-868.
16. Bull, T. A.; Pingree, L. S. C.; Jenekhe, S. A.; Ginger, D. S.; Luscombe, C. K., The Role of Mesoscopic PCBM Crystallites in Solvent Vapor Annealed Copolymer Solar Cells. *Acs Nano* **2009**, 3, (3), 627-636.
17. Yang, F.; Forrest, S. R., Photocurrent generation in nanostructured organic solar cells. *Acs Nano* **2008**, 2, (5), 1022-1032.

18. Kim, Y.; Choulis, S. A.; Nelson, J.; Bradley, D. D. C.; Cook, S.; Durrant, J. R., Device annealing effect in organic solar cells with blends of regioregular poly(3-hexylthiophene) and soluble fullerene. *Applied Physics Letters* **2005**, 86, (6), -.
19. Shrotriya, V.; Yao, Y.; Li, G.; Yang, Y., Effect of self-organization in polymer/fullerene bulk heterojunctions on solar cell performance. *Applied Physics Letters* **2006**, 89, (6), -.
20. Yang, F.; Shtein, M.; Forrest, S. R., Controlled growth of a molecular bulk heterojunction photovoltaic cell. *Nature Materials* **2005**, 4, (1), 37-41.
21. Kuang, D.; Brillet, J.; Chen, P.; Takata, M.; Uchida, S.; Miura, H.; Sumioka, K.; Zakeeruddin, S. M.; Gratzel, M., Application of highly ordered TiO₂ nanotube arrays in flexible dye-sensitized solar cells. *Acs Nano* **2008**, 2, (6), 1113-1116.
22. Snaith, H. J.; Schmidt-Mende, L., Advances in liquid-electrolyte and solid-state dye-sensitized solar cells. *Advanced Materials* **2007**, 19, (20), 3187-3200.
23. Hyun, B. R.; Zhong, Y. W.; Bartnik, A. C.; Sun, L. F.; Abruna, H. D.; Wise, F. W.; Goodreau, J. D.; Matthews, J. R.; Leslie, T. M.; Borrelli, N. F., Electron Injection from Colloidal PbS Quantum Dots into Titanium Dioxide Nanoparticles. *Acs Nano* **2008**, 2, (11), 2206-2212.
24. Ratanatawanate, C.; Xiong, C. R.; Balkus, K. J., Fabrication of PbS quantum dot doped TiO₂ nanotubes. *Acs Nano* **2008**, 2, (8), 1682-1688.
25. Sommeling, P. M.; Spath, M.; Smit, H. J. P.; Bakker, N. J.; Kroon, J. M., Long-term stability testing of dye-sensitized solar cells. *Journal of Photochemistry and Photobiology a-Chemistry* **2004**, 164, (1-3), 137-144.

26. Bai, Y.; Cao, Y. M.; Zhang, J.; Wang, M.; Li, R. Z.; Wang, P.; Zakeeruddin, S. M.; Gratzel, M., High-performance dye-sensitized solar cells based on solvent-free electrolytes produced from eutectic melts. *Nature Materials* **2008**, 7, (8), 626-630.
27. Boucle, J.; Ravirajan, P.; Nelson, J., Hybrid polymer-metal oxide thin films for photovoltaic applications. *Journal of Materials Chemistry* **2007**, 17, (30), 3141-3153.
28. Nanu, M.; Schoonman, J.; Goossens, A., Nanocomposite three-dimensional solar cells obtained by chemical spray deposition. *Nano Letters* **2005**, 5, (9), 1716-1719.
29. Seabold, J. A.; Shankar, K.; Wilke, R. H. T.; Paulose, M.; Varghese, O. K.; Grimes, C. A.; Choi, K. S., Photoelectrochemical Properties of Heterojunction CdTe/TiO₂ Electrodes Constructed Using Highly Ordered TiO₂ Nanotube Arrays. *Chemistry of Materials* **2008**, 20, (16), 5266-5273.
30. Wang, Q.; Zhu, K.; Neale, N. R.; Frank, A. J., Constructing Ordered Sensitized Heterojunctions: Bottom-Up Electrochemical Synthesis of p-Type Semiconductors in Oriented n-TiO₂ Nanotube Arrays. *Nano Letters* **2009**, 9, (2), 806-813.
31. Hanna, M. C.; Nozik, A. J., Solar conversion efficiency of photovoltaic and photoelectrolysis cells with carrier multiplication absorbers. *Journal of Applied Physics* **2006**, 100, (7), -.
32. Nowotny, J.; Sorerell, C. C.; Sheppard, L. R.; Bak, T., Solar-hydrogen: Environmentally safe fuel for the future. *International Journal of Hydrogen Energy* **2005**, 30, 521-544.
33. de Jongh, P. E.; Vanmaekelbergh, D.; Kelly, J. J., Cu₂O: a catalyst for the photochemical decomposition of water? *Chemical Communications* **1999**, (12), 1069-1070.

34. Bach, U.; Lupo, D.; Comte, P.; Moser, J. E.; Weissortel, F.; Salbeck, J.; Spreitzer, H.; Gratzel, M., Solid-state dye-sensitized mesoporous TiO₂ solar cells with high photon-to-electron conversion efficiencies. *Nature* **1998**, 395, (6702), 583-585.
35. Thimsen, E.; Biswas, P., Nanostructured photoactive films synthesized by a flame aerosol reactor. *Aiche Journal* **2007**, 53, (7), 1727-1735.
36. Izaki, M.; Shinagawa, T.; Mizuno, K. T.; Ida, Y.; Inaba, M.; Tasaka, A., Electrochemically constructed p-Cu₂O/n-ZnO heterojunction diode for photovoltaic device. *Journal of Physics D-Applied Physics* **2007**, 40, (11), 3326-3329.
37. de Jongh, P. E.; Vanmaekelbergh, D.; Kelly, J. J., Cu₂O: Electrodeposition and characterization. *Chemistry of Materials* **1999**, 11, (12), 3512-3517.
38. Photoelectrochemical cells in the traditional dye-sensitized solar cell configuration were constructed using pristine TiO₂ films (i.e. no dye) and tested. These cells developed approximately 0.1 mA cm⁻². In addition, the photocurrent of the Cu₂O/TiO₂ cells only dropped slightly if a 375 nm long pass filter was used to eliminate the UV portion of the spectrum, again suggesting that the photocurrent in the Cu₂O/TiO₂ cells primarily resulted from visible light. In.
39. Truijen, I.; Van Bael, M. K.; Van den Rul, H.; D'Haen, J.; Mullens, J., Synthesis of thin dense titania films via an aqueous solution-gel method. *Journal of Sol-Gel Science and Technology* **2007**, 41, (1), 43-48.
40. Li, S. S., *Semiconductor physical electronics*. Plenum: New York, 1993; p xiii, 507 p.
41. Madelung, O., *Semiconductors--basic data*. 2nd rev. ed.; Springer: Berlin ; New York, 1996; p 317 p.

42. Rausch, N.; Burte, E. P., Thin Tio₂ Films Prepared by Low-Pressure Chemical Vapor-Deposition. *Journal of the Electrochemical Society* **1993**, 140, (1), 145-149.
43. Ishizuka, S.; Kato, S.; Okamoto, Y.; Akimoto, K., Control of hole carrier density of polycrystalline Cu₂O thin films by Si doping. *Applied Physics Letters* **2002**, 80, (6), 950-952.
44. Forro, L.; Chauvet, O.; Emin, D.; Zuppiroli, L.; Berger, H.; Levy, F., High-Mobility N-Type Charge-Carriers in Large Single-Crystals of Anatase (Tio₂). *Journal of Applied Physics* **1994**, 75, (1), 633-635.
45. Kavan, L.; Gratzel, M., Highly Efficient Semiconducting Tio₂ Photoelectrodes Prepared by Aerosol Pyrolysis. *Electrochimica Acta* **1995**, 40, (5), 643-652.

Chapter 8:

Conclusions and Future Directions

8.1 Conclusions

While this thesis did not find the "holy grail" solution to the energy problem, which would be a low cost material capable of directly producing solar fuels with a sunlight-to-fuel energy conversion efficiency of 10%, several important strides were made in that direction. These conclusions are likely to have a lasting impact on the fields of aerosol film deposition, solar energy harvesting by metal-oxide semiconductors and others. Below are the major conclusions drawn by this work:

- i. Human development increases with per capita primary energy consumption. However, there is an energy consumption level after which little gain in development is achieved by increasing primary energy consumption, a point of diminishing return, or saturation energy. If every nation in the world had a primary energy consumption equal to the saturation energy, it would require a more than doubling of global primary energy consumption. In light of climate change, solar energy harvesting is an attractive source to meet the growing demand, and utilizing new technology based on metal oxide semiconductors has the potential to break through the cost barriers currently preventing widespread adoption.
- ii. A robust system consisting of a flame aerosol reactor (FLAR) for the deposition of nanostructured TiO₂ films with controlled morphology was developed. The FLAR can be used to synthesize nanocrystalline granular films with high surface area or single-crystal columnar films with slightly lower surface area, but superior electron transport characteristics. The process is rapid, single step, operates at

atmospheric pressure and is industrially scalable. The FLAR affords rational control over many important materials properties such as thickness, surface area, grain size and electron transport characteristics.

- iii. Controlling morphology, which includes nanostructure, is a conceptual tool that can be used to improve device performance, in some cases by factors as large as 10 to 50. Despite having a lower surface area, single-crystal columnar TiO₂ films have superior performance in dye-sensitized solar cells and photo water splitting cells relative to unsintered granular structures, mainly due to superior electron transport characteristics and lower recombination rates, which lead to a simulated sunlight-to-electricity conversion efficiency of approximately 6.0 % for dye-sensitized solar cells and a UV-light-to-hydrogen conversion efficiency of 11% for photocatalytic water splitting.
- iv. A reaction mechanism for photo oxidation of water on the surface of TiO₂ was proposed. At acidic and neutral pH values, water molecule oxidation dominates, while at basic pH values, hydroxide ion (OH⁻) oxidation dominates. Hydroxide ion oxidation is more rapid than the oxidation of water molecules, likely due to the electrostatic interaction between positive holes in the TiO₂ and the negative hydroxide ions on the surface. It appears as though seawater can be used as a resource for water splitting, so long as the pH of the water is sufficiently high. Although, accumulation of ions in the electrolyte could eventually lead to precipitation, potentially leading to catalyst deactivation.

- v. The role of chemical composition in determining the electronic band structure of mixed metal oxides in the Ti-Fe-O system was studied. It was found that the conduction and valence bands in the mixed compounds were at the same energy levels as the pristine, basis compounds. A simple mixed metal oxide band structure (MMOBS) was proposed as a simple design tool for mixed compounds.
- vi. Bulk-heterojunctions (BHJ) between columnar n-TiO₂ and p-Cu₂O were successfully synthesized. The important characteristic dimensions of the BHJ were identified: the BHJ thickness (L_{BHJ}), inter-column spacing (L_s), guest volume fraction (ϕ_{Cu_2O}) and absorption depth (L_{ABS}). The p/n junction exhibited rectifying characteristics and the devices behaved as photovoltaics under simulated AM1.5G illumination. The photocurrent developed by the cells increased with n-TiO₂ column thickness until the bulk heterojunction thickness (L_{BHJ}) was the same as the light absorption depth (L_{ABS}), resulting in a 2.6 times higher photocurrent and 4.3 times higher conversion efficiency than the thin case. Increasing L_{BHJ} beyond the absorption depth (L_{ABS}) resulted in no further performance gains. Increasing the BHJ thickness provides access to excitons deep in the bulk that would normally recombine if the n-TiO₂ columns were not there, improving the device performance. The result provides design concepts and lays the foundation for the development of a monolithic all-oxide self-biased water splitting device.

8.2 Future Directions

8.2.1 Columnar Film Synthesis Mechanism

It would be rather straightforward, but important to do a detailed study of the deposition mechanism for the columnar films. Indeed, it appears as though the mechanism is a *physical* mechanism and the columnar morphology should be achievable with many different materials, although the necessary time-temperature history would be material dependent. In addition, by controlling the Péclet number of the depositing particles (by changing the strength of the thermophoretic force driving deposition, for instance), the column width and spacing could probably be controlled, to some extent.

An integrated theory-experiment approach would likely yield the best results. On the experimental side, films could be deposited using different metal-organic precursors, empirically tuning the deposition conditions (temperature, particle size) to achieve the columnar morphology for different metal oxide materials. The critical temperature and particle size would likely be related to the melting point of the material, lower melting point materials forming the columnar structure at milder sintering conditions (larger particles and lower temperatures), and higher melting point materials achieving the columnar morphology at more intense sintering conditions (smaller particles and higher temperatures).

Simple sequential Brownian dynamics could be performed on large numbers of particles to observe preferential deposition on the protruding structures (unsintered columns). Column size could be defined based on a radial distribution function, allowing

the effect of the incoming particle Péclet number on the characteristic size and spacing of the columns to be systematically studied.

8.2.2 Dye-Sensitized Solar Cells

It was found that the columnar nanostructure yielded a higher photocurrent than the unsintered granular structure in Chapter 4. However, it is likely that there is an optimum morphology between the columnar structure and the unsintered granular structure, which has higher surface area and therefore light absorption in dye-sensitized solar cells. A more detailed study of the effect of morphology could be performed by depositing films with morphologies intermediate between the columnar and granular, or by post-annealing the granular structures to improve inter-particle electrical contact.

8.2.3 Electrolyte Saturation Effects

If one wishes to use seawater as a source of water for photo water splitting, as the water is consumed the concentrations of various ionic species in the electrolyte will accumulate. The accumulation will lead at some point to saturation and precipitation. It would be interesting to systematically study the effect of electrolyte saturation on water splitting device performance. It is expected that strategies developed by the reverse osmosis water purification community, who experience similar issues with saturation and precipitation of ionic species in aqueous electrolytes, could be applied in this case to overcome the saturation issue.

8.2.4 Extension of MMOBS

One could perform DFT calculations on more materials to determine the specific classes of materials for which the MMOBS procedure is valid.

8.2.5 Improvement of n-TiO₂/p-Cu₂O BHJ Cells

The n-TiO₂/p-Cu₂O cells are the first of their kind to be synthesized. Thus there is much work that could be done to improve performance. Below are recommended places to first attack the problem. The devices could be further improved by depositing a higher quality hole-blocking layer by spray pyrolysis, carefully controlling the p-Cu₂O deposition conditions, and post-processing such as annealing the junctions to improve interfacial contact, charge transport and reduce defect concentrations in the structure. Also, interfacial layers between the p-type and n-type materials would likely help. Simple steps like these could lead to performance gains over several orders of magnitude. In addition, these cells could also be applied to self-biased water splitting.

Appendix I:

Experimental Setups

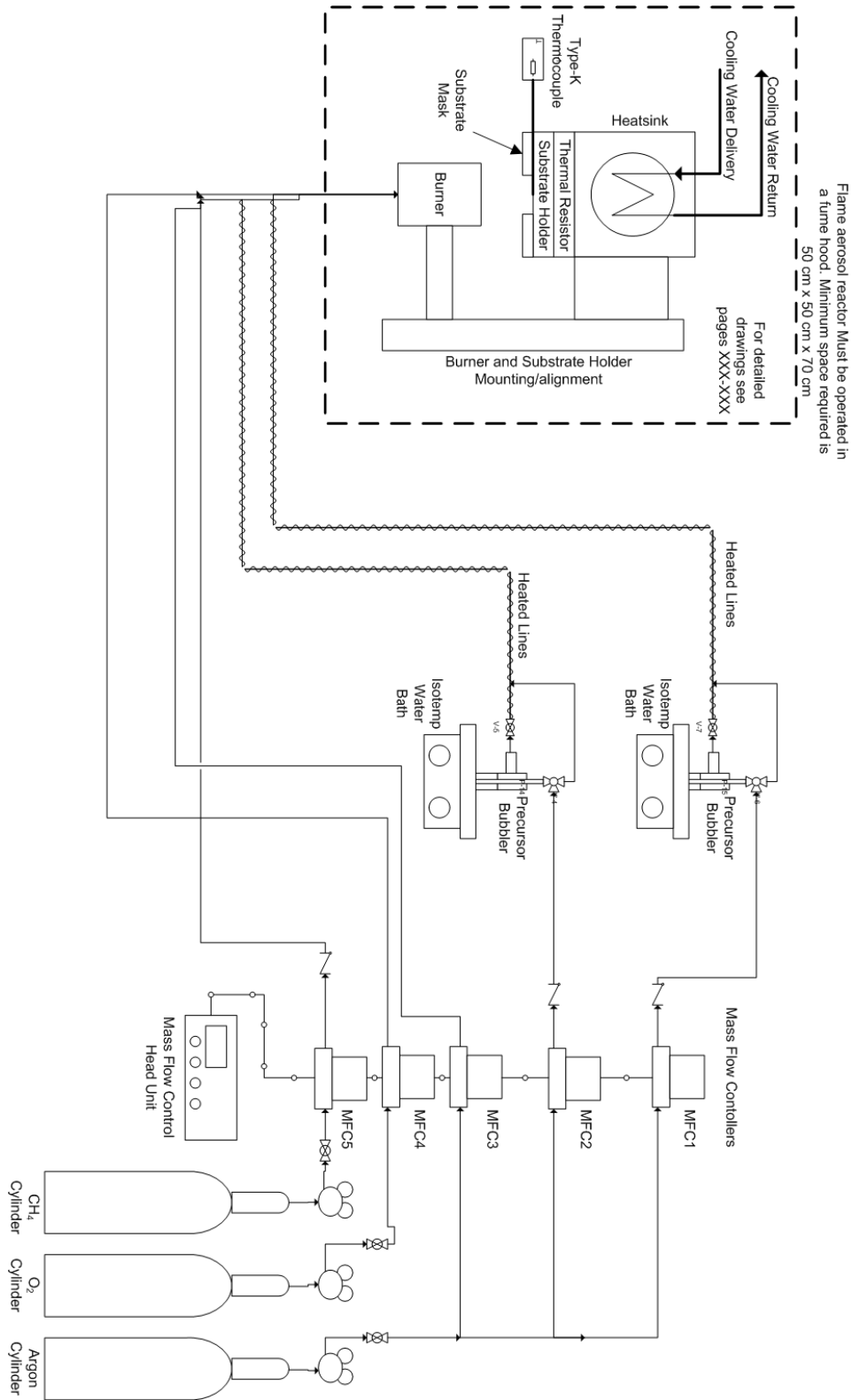


Figure I-1: Schematic of the premixed flame aerosol reactor (FLAR).

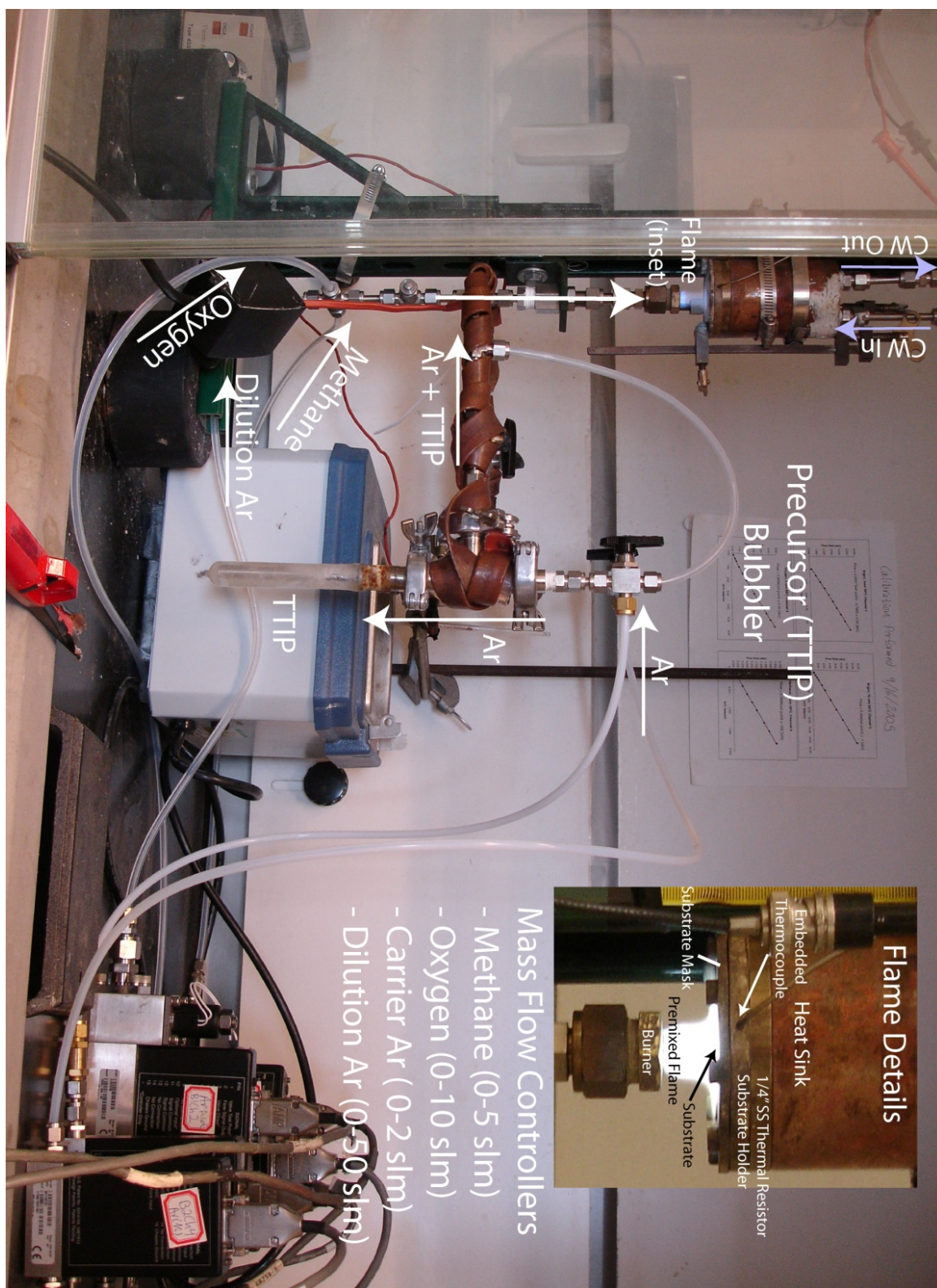


Figure I-2: Digital image of the premixed flame aerosol reactor (FLAR).

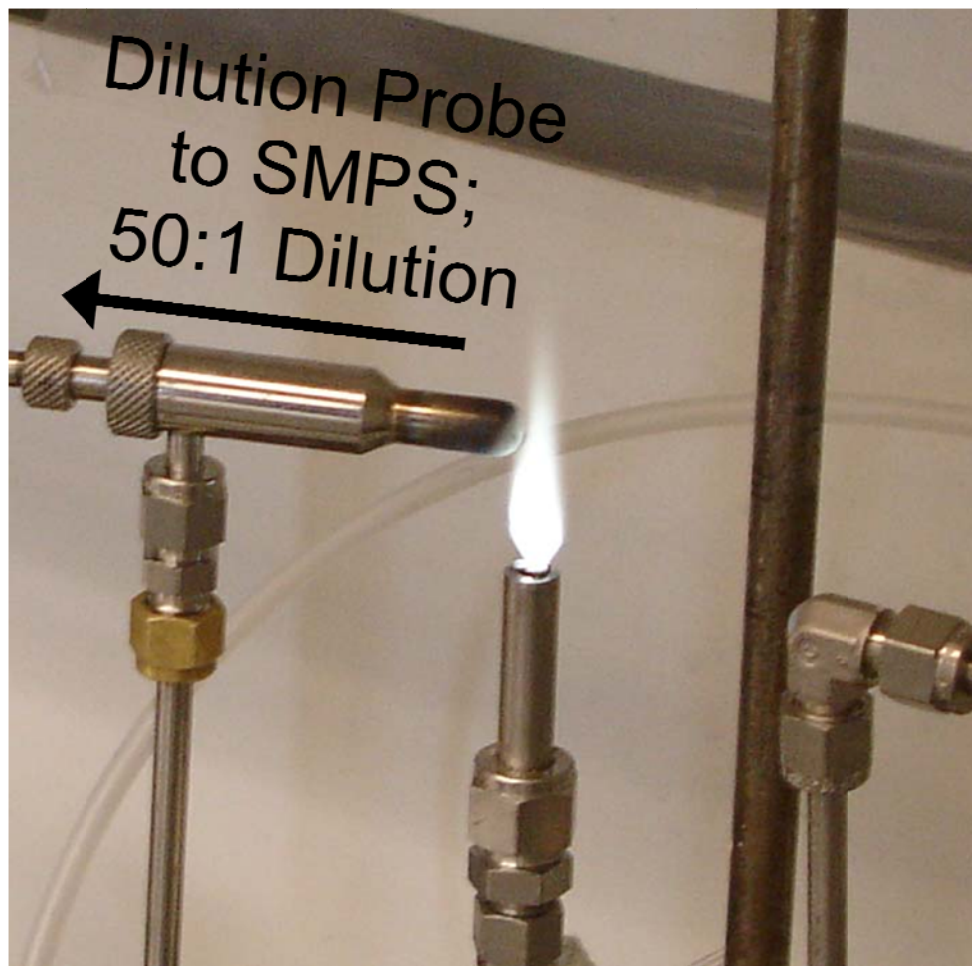


Figure I-3: Digital image of the sampling for aerosol size distribution measurements by SMPS in Chapter 3. The probe is a primary dilution probe.

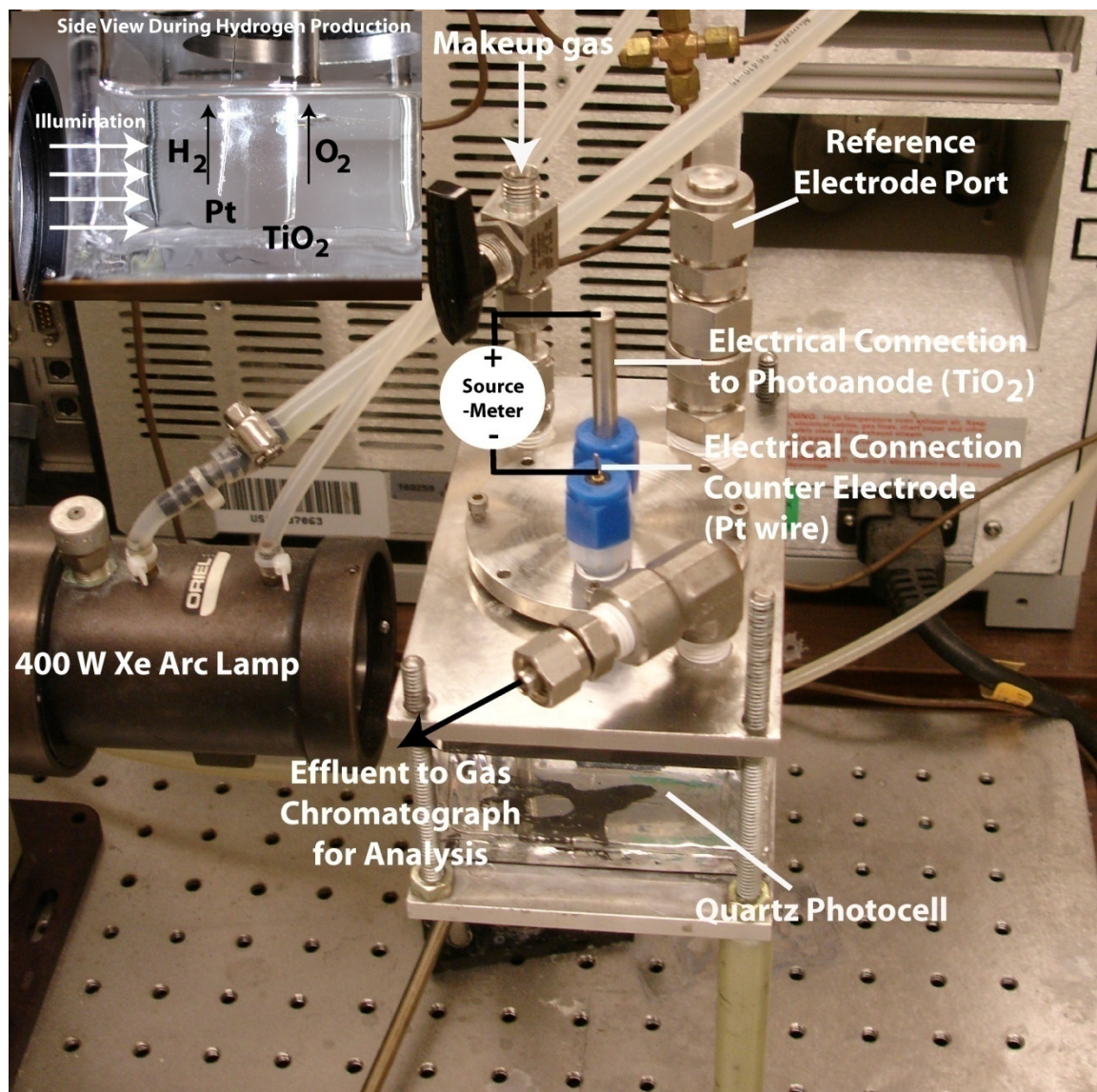


Figure I-4: Digital image of the water splitting photocell.



Figure I-5: Digital image of the solar simulator used for photovoltaic testing in Chapter 7.

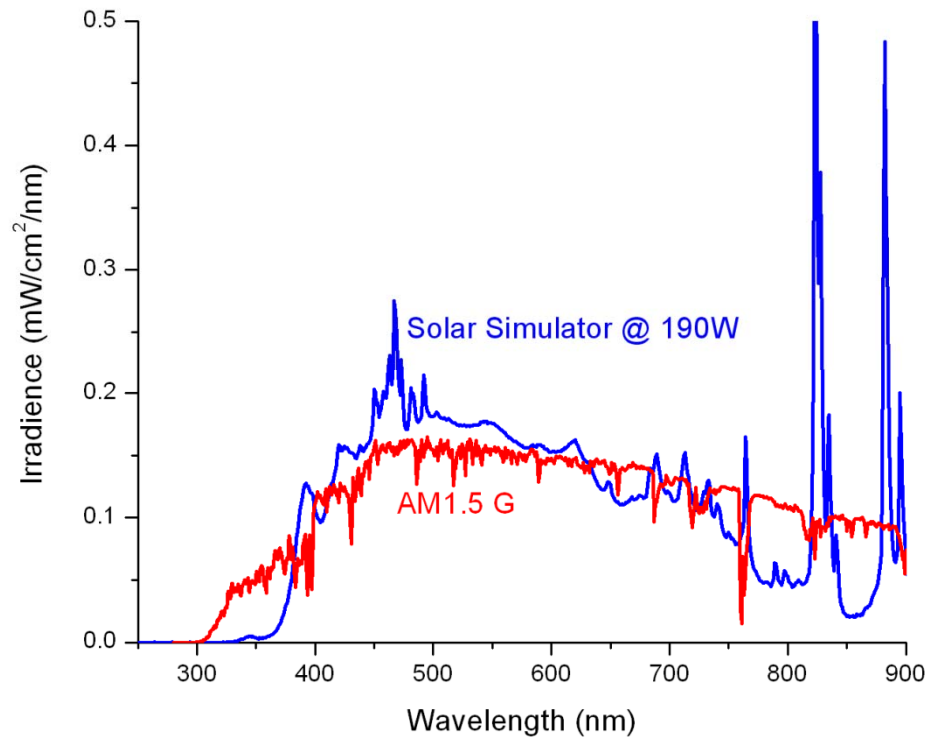


Figure I-6: Comparison of the spectral output of the solar simulator to the AM1.5G standard.

Appendix II:

pH and Redox Thermodynamics

In Chapter 5 the thermodynamics of water splitting were discussed in the context of various standard reduction-oxidation potentials at pH 0. However, it should be noted that changing the pH can affect these thermodynamics. The effects of pH on the thermodynamics of TiO₂-based photocatalysis have been addressed by Bard et al¹. The key findings are presented here. First, in an aqueous solution at room temperature, the valence and conduction band positions of TiO₂ shift with pH according to the following equations¹:

$$E_{CB} = E_{CB}^0 - 0.059pH \quad (\text{II.1})$$

$$E_{VB} = E_{VB}^0 - 0.059pH \quad (\text{II.2})$$

where the superscript 0 denotes the potential of the valence and conduction bands at standard conditions (pH 0). At room temperature, the potentials of water oxidation and proton reduction shift by the same amount as a function of pH according to the Nernst equation²:

$$E_H \approx E_H^0 - 0.059pH \quad (\text{II.3})$$

where E_H^0 is the standard reduction potential for the water oxidation and proton reduction half reactions, +1.23 volts and 0.00 volts respectively. Since the band positions of the TiO₂ and water oxidation half reactions have the same pH dependence, the pH has no net effect of the thermodynamics of these reactions with respect to reduction or oxidation by photo-excited TiO₂.

However, if a given reduction-oxidation reaction is pH-independent, then the thermodynamic driving force for photocatalytic reduction or oxidation of this species will

change as a function of pH (Figure II.1). These considerations should be taken into account in analyzing complex electrolytes.

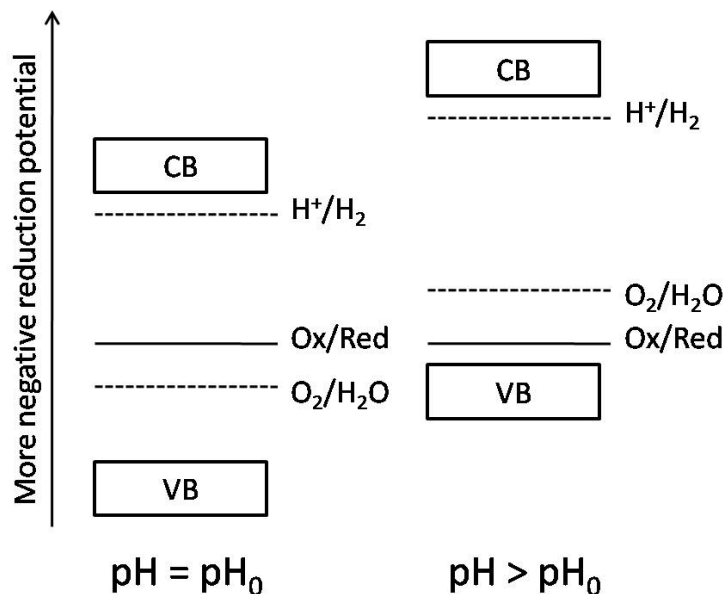


Figure II.1: Trend in potential with pH for the band positions of TiO₂, proton reduction, water oxidation, and an arbitrary pH-independent reduction-oxidation half reaction labeled as Ox/Red. This figure was adapted from Bard et al¹.

References:

1. Ward, M. D.; White, J. R.; Bard, A. J., Electrochemical Investigation of the Energetics of Particulate Titanium-Dioxide Photocatalysts - the Methyl Viologen Acetate System. *Journal of the American Chemical Society* **1983**, 105, (1), 27-31.
2. Schwarzenbach, R. P.; Gschwend, P. M.; Imboden, D. M., *Environmental organic chemistry*. J. Wiley: New York, 1993; p x, 681 p.

Appendix III:

Curriculum Vitae

Name: Elijah James Thimsen

Born: 13 October 1982, Minneapolis MN

Address:

2977 Caroline Court
Saint Paul MN, 55117

Education:

2009 Ph.D. in Energy, Environmental and Chemical Engineering
Advisor: Dr. Pratim Biswas
Washington University in Saint Louis, Saint Louis MO

2005 Bachelors of Mechanical Engineering
University of Minnesota, Minneapolis MN

Research Experience:

2005-2009 Aerosol and Air Quality Research Laboratory
Department of Energy, Environmental and Chemical Engineering
Washington University in Saint Louis

2002-2005 High Temperature and Plasma Laboratory
Department of Mechanical Engineering
University of Minnesota

Students Supervised (2)

2. Neema Rastgar (May 2007 to May 2009) -- B.S. Chem. E. 2009
Currently a Chemical Engineering Ph.D. Student at the University of Minnesota

1. Sam Crawford (August 2006 to May 2008) -- B.S. Chem. E. 2008
Currently a Materials Science Ph.D. Student at the Massachusetts Institute of Technology

Awards and Honors:

- National Science Foundation International Research Fellowship (2009-declined)
- Graduate Research Fellowship, Center for Materials Innovation (CMI) at Washington University in Saint Louis (9/2005)
- Honorable Mention, National Science Foundation (4/2006)
- The John L. and Julianne J. Stein Scholarship, Washington University in Saint Louis (11/2005)
- Inventor Recognition Award, Patents and Technology Marketing, University of Minnesota (9/2005)
- Undergraduate Research Grant, Undergraduate Research Opportunities Program (UROP), University of Minnesota (1/2004)

- Walter and Margaret Pierce Endowment Fund Scholarship for Academic Excellence, Department of Mechanical Engineering, University of Minnesota (11/2003)
- Dean's List - Institute of Technology, University of Minnesota (2002-2005)

Select Professional Service:

1. Peer reviewer for the *Journal of Physical Chemistry, Chemistry of Materials, and Materials*
2. Graduate Student Assistant for the 1st and 2nd International Symposium on Energy and Environment (May 2007 and December 2008)

Refereed Publications (6)

6. Sam Crawford, **Elijah Thimsen** and Pratim Biswas; *Impact of Electrolyte on Photocatalytic Water Splitting*, Journal of the Electrochemical Society (2009), Vol. 156, No. 5, H346-H351
5. **Elijah Thimsen**, Suhashis Biswas, Cynthia Lo and Pratim Biswas; *Predicting the Band Structure of Mixed Transition Metal-Oxides: Theory and Experiment*, Journal of Physical Chemistry C (2009), Vol 113, pp. 2014-2021
4. **Elijah Thimsen**, Neema Rastgar and Pratim Biswas, *Nanostructured TiO₂ films with controlled morphology synthesized in a single step process: performance of dye-sensitized solar cells and photo watersplitting*, Journal of Physical Chemistry C (2008) Vol 112, No. 11, pp. 4134-4140
3. **Elijah Thimsen** and Pratim Biswas, *Nanostructured Photoactive Films Synthesized by a Flame Aerosol Reactor*, AIChE J. (2007) Vol.53, No. 7, pp.1727-1735
2. Anthony, R.; **Thimsen, E.**; Johnson, J., Campbell, S.; Kortshagen, U., *A Non-Thermal Plasma Reactor for the Synthesis of Gallium Nitride, GaN, AlN, InN and Related Materials*. Symposium (Materials Research Society Symposium Proceedings Vol.892) (2006) pp.221-224
1. Lorenzo Mangolini, **Elijah Thimsen** and Uwe Kortshagen, *High Yield Scaleable Plasma Synthesis of Luminescent Silicon Nanocrystals*; Nanoletters (2005) Vol. 5, No. 4, pp.655-659

Refereed Publications in Preparation or Submitted (4)

4. Luis Modesto-Lopez, **Elijah Thimsen**, Aaron Collins, Robert Blankenship and Pratim Biswas, *Electrospray-Assisted Characterization and Deposition of Chlorosomes to Fabricate a Light-Harvesting Nano-Bio Device*, in preparation

3. **Elijah Thimsen** and Pratim Biswas, *Human Development and the Energy-Environment Nexus*, in preparation

2. **Elijah Thimsen** and Pratim Biswas, *Visible light active all oxide bulk-heterojunction photovoltaics*, Submitted to ACS Nano

1. Pratim Biswas and **Elijah Thimsen**, *High Temperature Aerosols: Measurement, Deposition, and Applications in Energy and Environmental Nanotechnologies*, Book Chapter in the 2009 edition of Aerosol Measurement Submitted

Patents (2):

2. **Elijah Thimsen** and Pratim Biswas, *Synthesis of Nanostructured Photoactive Films with Controlled Morphology by a Flame Aerosol Reactor*, U.S. patent application number 60/969,365

1. Uwe Kortshagen, **Elijah Thimsen**, Lorenzo Mangolini, Ameya Bapat and David Jurbergs, *Process and Apparatus for Forming Nanoparticles Using Radiofrequency Plasmas*, United States Patent No 7,446,335 (November 4th 2008)

External Oral Presentations (6):

6. **Elijah Thimsen** *Aerosol Processing of Nanostructured Metal Oxides for Solar Energy Harvesting*, 3 Invited seminars at ETH and EPFL in Switzerland, December 2008.

5. **Elijah Thimsen** and Pratim Biswas, *Bionano Antenna-Reaction Center (ARC) Hybrid Solar Cells Facilitated by Aerosol Processing* American Association for Aerosol Research Conference, October 2008, Orlando FL, USA

4. **Elijah Thimsen**, Subhashis Biswas, Cynthia Lo and Pratim Biswas, *Nanostructured TiO₂ thin films doped with transition metals for enhanced visible light absorption: experiments and first-principles calculations* American Chemical Society Conference, April 2008, New Orleans LA, USA

3. **Elijah Thimsen**, Neema Rastgar and Pratim Biswas, *Rapid synthesis of nanostructured metal-oxide films for solar energy applications by a flame aerosol reactor (FLAR)* SPIE Optics and Photonics Conference, August 2007, San Diego CA, USA

2. **Elijah Thimsen**, Hee-eun Song, Christine Kirmaier, Dewey Holten and Pratim Biswas, *Flame aerosol reactor (FLAR) fabrication of doped and pristine nanostructured metal-oxide films for solar-hydrogen production* American Chemical Society Conference, March 2007, Chicago IL, USA

1. **Elijah Thimsen** and Pratim Biswas, *Premixed Flame Deposition of Anatase TiO₂ Films for Photo-Activated Processes* International Aerosol Conference, September 2006, Saint Paul MN, USA

External Poster Presentations (4):

4. **Elijah Thimsen** and Pratim Biswas, *Aerosol Processing for Solar Energy Harvesting* Gordon-Kenan Research Conference (GRC) on Solar Fuel Production, February 2009, Ventura CA, USA

3. **Elijah Thimsen** and Pratim Biswas, *Aerosol Processing for Solar Energy Harvesting* McDonnell Global Energy and Environment Partnership (MAGEEP) Meeting, December 2008, Hong Kong, China

2. **Elijah Thimsen**, Neema Rastgar, Cynthia Lo and Pratim Biswas, *Nanostructured Oxide Semiconductor Films with Controlled Morphology by a Flame Aerosol Reactor*, Materials Research Society Fall Meeting, Boston MA, USA

1. **Elijah Thimsen** and Pratim Biswas, *Rapid Synthesis of Photo-Active Anatase Titanium Dioxide Films by a Premixed Flame Aerosol Reactor*, Energy Nanotechnology International Conference, June 2006, Cambridge MA, USA